

**THERMORESPONSIVE TRANSIENT ELECTRONIC SYSTEMS AND  
MICROFLUIDIC DEVICES FOR BIOMEDICAL APPLICATIONS**

By

XIN ZHANG

Dissertation

Submitted to the Faculty of the  
Graduate School of Vanderbilt University  
in partial fulfillment of the requirements

for the degree of

DOCTOR OF PHILOSOPHY

in

Mechanical Engineering

December 14, 2019

Nashville, Tennessee

Approved:

Leon Bellan, Ph.D

Deyu Li, Ph.D

Charles Manning, Ph.D

Greg Walker, Ph.D

Yaqiong Xu, Ph.D

**DEDICATION**

*To my beloved mom, dad, and grandparents*

## ACKNOWLEDGEMENT

First, I would like to thank my advisor, Dr. Leon Bellan, for his mentorship throughout this research.

I would like to thank my Ph.D. dissertation committee Dr. Charles Manning, Dr. Deyu Li, Dr. Greg Walker, and Dr. Yaqiong Xu for their expertise and valuable suggestions.

I would like to thank my colleagues for their support, feedback and collaboration throughout my graduate studies: Dr. Michael Nickels, Dr. Fei Liu, Dr. Shannon Faley, Dr. Jung Bok Lee, Dr. Qian Zhang, Brian O'grady, John Rector, Callie Weber, Jason Wang. Then, I would like to thank staff members of the Vanderbilt Institute of Nanoscale Science and Engineering (VINSE): Kurt Heinrich, Dr. Bo Choi, Dr. Ben Schmidt, Dr. Dmitry Koktysh, Dr. Anthony Hmelo, Dr. Alice Leach and Dr. William Martinez. In addition, I would like to thank Dr. Enxia Zhang and Dr. Tim Holman for their valuable helpful discussions on how to characterize radio frequency circuits.

Further, I would like to thank my friends throughout my life who contribute enormously to my currently remaining sanity. I very much cherish our friendship.

Finally, to my family, there is no way I can thank you all enough. It is your unconditional love and support that allow me to be the man who I am now.

## TABLE OF CONTENTS

	Page
DEDICATION .....	ii
ACKNOWLEDGEMENT .....	iii
TABLE OF CONTENTS.....	iv
LIST OF TABLES .....	vi
LIST OF FIGURES .....	vii
Chapter 1 Introduction .....	1
1.1 Background .....	1
1.2 Overview of Transient Electronics.....	6
1.3 Overview of PET Radiotracer Synthesis using Microfluidic Devices .....	14
Chapter 2 Thermoresponsive Conductive Composites for Transient Electronics .....	20
2.1 Introduction .....	20
2.2 Methods and Materials .....	24
2.3 Results and Discussion.....	26
2.4 Conclusion.....	35
Chapter 3 Thermoresponsive Transient Radio Frequency Circuits .....	37
3.1 Introduction .....	37
3.2 Methods and Materials .....	42
3.3 Results and Discussion.....	45
3.4 Conclusion.....	57
Chapter 4 Thermal Transport in Electrospun Polymer Nanofiber .....	58
4.1 Introduction .....	58
4.2 Methods and Materials .....	60
4.3 Results and Discussion.....	62
4.4 Conclusion.....	73
Chapter 5 [ <sup>18</sup> F]Fallypride Synthesis Using a Simple Microfluidic Device .....	74
5.1 Introduction .....	74
5.2 Materials and Methods .....	78
5.3 Results and Discussion.....	85
5.4 Conclusion.....	94
Chapter 6 High-yielding Radiosynthesis of <sup>68</sup> Ga-PSMA-11 Using a Low-cost Microfluidic Device .....	96
6.1 Introduction .....	96
6.2 Materials and Methods .....	100
6.3 Results and Discussion.....	105
6.4 Conclusion.....	116



Chapter 7 Summary and Outlook .....117  
REFERENCES .....120

## LIST OF TABLES

Table	Page
<b>Table 4. 1</b> Properties of four vinyl polymer materials, including: formula, molecular weight (Mw), monomer weight, molecular chain length, room temperature thermal conductivity ( $k$ ), calculated single chain Young's modulus ( $E_{\text{single chain}}$ ), and glass transition temperature (Tg).....	62
<b>Table 5. 1</b> The relationship between the volume of anion exchange beads inside the concentration column and the radioactivity trapped on the microfluidic chip. All listed values are decay-corrected to the time point of initial radioactivity in the syringe. ....	86
<b>Table 5. 2</b> The relationship between the volume of $K_{222}/K_2CO_3$ used for releasing trapped [ $^{18}F$ ]fluoride off the concentration column and the releasing efficiency. The efficiency is calculated accounting for the decay of the radionuclide over time. ....	87
<b>Table 5. 3</b> Operational performances of our microfluidic platform compared to several reported results based on microfluidic [ $^{18}F$ ]fallypride production. All efficiencies and yields are calculated based on decay-corrected values. ....	93
<b>Table 6. 1</b> Experimental results of the efficiency of miniaturized SCX and SAX columns at critical steps. All efficiencies are calculated based on decay-corrected values. ....	108
<b>Table 6. 2</b> Production performance comparison between routinely employed system and reported microfluidic system. ....	114
<b>Table 6. 3</b> A comparison between clinical acceptance criteria and quality control tests of synthesized $^{68}Ga$ -PSMA using developed microfluidic system. ....	115

## LIST OF FIGURES

Figure	Page
<b>Figure 1. 1</b> Demonstration of transient electronics. (a) Images of a device that includes transistors, diodes, inductors, capacitors, and resistors, with interconnects and interlayer dielectrics, all on a thin silk substrate. (b) Exploded-view schematic illustration, with a top view in the lower right inset. (c) Images showing the time sequence of dissolution in DI water. ....7	7
<b>Figure 1. 2</b> Changes in resistance of serpentine thin film traces as a function of time during dissolution in Hanks' solution and in DI water, for cases of (a) Mg (300 nm); (b) AZ31B Mg alloy (300 nm); (c) sputter deposited W (150nm); (d) Zn (300 nm); (e) Mo (40 nm); (f) CVD W (150 nm); (g) Fe (150 nm); (h) Mg, AZ31B Mg alloy, and Zn; (i) Mo, Fe and sputter deposited W. ....9	9
<b>Figure 1. 3</b> Images of Si NMs at various stage of dissolution in bovine serum (pH~7.4 at physiological temperature (37 °C) measured by (a) DPM and (b) AFM. Thickness profiles extracted from the (c) DPM and (d) AFM images in (a) and (b). (e) Theoretical and measured changes in resistance of a serpentine shaped Si NMs after various times of immersion in PBS (blue) and bovine serum (red) at body temperature. ....11	11
<b>Figure 1. 4</b> Images of dissolution and degradation of SWNT FETs on a PVA substrate in water at various stages, (a) 10s, (b) 90s, (c) 300s, (d) 1800s. ....12	12
<b>Figure 1. 5</b> Heat-triggerable transient electronics coated with wax containing acid dispersions. Release of MSA by melting a wax coating leads to rapid electronic destruction by acidic degradation of Mg electrodes on glass. In addition, using a cyclic poly(phthalaldehyde) (cPPA) substrate affords a more rapid destruction of the device due to acidic depolymerization of cPPA. .... 14	14
<b>Figure 1. 6</b> (A) Schematic representation of a chemical reaction circuit used in the production of 2-deoxy-2-fluoro-d-glucose (FDG). Five sequential processes are shown: (i) concentration of dilute fluoride ion with the use of a miniaturized anion exchange column located in a rectangle-shaped fluoride concentration loop, (ii) solvent exchange from water to dry MeCN, (iii) fluorination of the d-mannose triflate precursor 1, (iv) solvent exchange back to water, and (v) acidic hydrolysis of the fluorinated intermediate 2a (or 2b) in a ring-shaped reaction loop. Nanogram amounts of FDG (3a, 3b) are the final product. The operation of the circuit is controlled by pressure-driven valves, with their delegated responsibilities illustrated by their colors: red for regular valves (for isolation), yellow for pump valves (for fluidic metering circulation), and blue for sieve valves (for trapping anion exchange beads in the column module). (B) Optical micrograph of the central area of the circuit. The various channels have been loaded with food dyes to help visualize the different components of the microfluidic chip; colors are as in (A), plus green for fluidic channels. Inset: Actual view of the device; a penny (diameter 18.9 mm) is shown for comparison. ....16	16
<b>Figure 1. 7</b> EWOD chip designed and fabricated for tracer synthesis. (A) Schematic of the chip, showing the actuation glass plate patterned with regular EWOD electrodes (blue),	

multifunctional electrodes named heating site (orange and red), and electric contact pads along the two edges, as well as the electrical ground glass plate assembled on top. (B) A picture of the fabricated chip, showing the EWOD and multifunctional electrodes (slightly darker) and gold connection lines and contact pads (yellow). .....18

**Figure 2. 1** (a)Thermoresponsive transient system with AgNWs embedded in a LCST polymer film. The conductive AgNW network disintegrates when the water bath temperature cools below the LCST and the polymer binder dissolves. (b) Stability of a AgNW/PNIPAm composite over 24 h and dramatic disintegration upon water bath cooling below LCST (~32 °C). (c) Stability of a AgNW/MC composite over 24 h and dramatic disintegration upon water bath cooling below LCST (~45 °C).....23

**Figure 2. 2** Schematic illustration of the fabrication process used to pattern AgNW networks. 1. Deposit parylene onto Si wafer. 2. Use photolithography to pattern desired shape in resist. 3. Remove exposed parylene film using oxygen plasma. 4. Cast AgNW suspension on the whole wafer surface. 5. Peel the parylene off and leave patterned AgNWs on the surface. 6. Spin coat methyl cellulose solution. 7. Gently peel methyl cellulose film from Si substrate. ....25

**Figure 2. 3** Electrical conductance of an immersed transient circuit (50mm in length and 4 mm in width), and water bath temperature after the bath heater is turned off. Measurements were taken every 5 seconds. Transient behavior of methyl cellulose film (0.08 mm in thickness, containing an embedded AgNW network) with molecular weight of 88,000(a), 41,000(b) and 14,000(c). (d) shows the transient behavior of 0.7 mm thick MC film with the same molecular weight as (b) but almost 10x thicker.....27

**Figure 2. 4** (a) SEM image of AgNW network embedded within a MC film. (b) Stability of the electrical conductance of the AgNW network embedded in MC over 24 h immersed in a warm water bath (change of 9.7%). (c) Dramatic loss of conductivity when the water bath cools below the LCST. (d-f) Optical images of the AgNW/MC film morphology change in a water bath at 60, 38 and 22 °C. ....28

**Figure 2. 5** The electrical resistance of a AgNM/MC film after being deformed 180° by hand versus number of times bent. ....30

**Figure 2. 6** Conductivity of varying mass ratio AgNWs/PNIPAm with AgNW aspect ratio L/D 2000~4000 (a) and 100 (b). Dotted line represents the 3D theoretical electrical percolation threshold for isotropically oriented cylinders with identical aspect ratios. Solid line represents the 2D theoretical electrical percolation threshold for isotropically oriented rectangles. ....31

**Figure 2. 7** (a) Patterned parallel AgNW/MC conductive traces with linewidth of 2 mm and 500 μm. The inset shows the conductors deformed by hand. (b) Patterned zigzag traces of AgNWs/MC. The inset shows zigzag patterns with linewidth of 50 μm. (c) Optical image of the deformed LED circuit. (d) Optical image of the LED circuit connected with AgNW/MC conductor submerged in hot water. (e) Optical image of the LED circuit connected with AgNW/MC conductor submerged in cold water. ....32

**Figure 2. 8** (a) Schematic showing the parallel-plate capacitor formed from AgNWs and MC. (b) Stability of capacitance over 24 h in warm water bath (change of ~10%). (c) Dramatic change in capacitance as water bath temperature drops below the LCST. ....33

**Figure 2. 9** Energy dispersive spectroscopy (EDS) image of parallel plate capacitor built by

attaching two slabs of AgNW/MC film together. Blue indicates Ag and red indicates C. ....34

**Figure 2. 10** Capacitance change over time when the dry capacitor was placed on a hot plate. ...35

**Figure 3. 1** Schematic illustration of thermoresponsive transient radio frequency circuitry consisting of parylene encapsulation layers, bonding MC substrates as well as conductive AgNW traces embedded in the middle. When immersed in warm water, the whole circuitry can maintain physically and electrically stable. However, when solution temperature drops below LCST, the dissolution of in-between MC substrates leads to rapid disintegration of percolating AgNW network, implementing thermally triggered transience on demand.....42

**Figure 3. 2** A photograph of apparatus for characterization of the correlation between S11 of thermoresponsive transient RFID device and corresponding solution temperature. (1) - (6) represent the spectrum analyzer, a computer-controlled hot plate, a two-turn primary probe, a xyz control stage, a directional coupler, and a beaker filled with PBS solution. ....44

**Figure 3. 3** Tensile testing sample photo (top) and schematic representation (bottom), indicating bonding locations and overlapping areas used in test. (b) Measured results of bonding strength of laminated MC samples with/without thermal treatment. Red curve represents MC sample heated at 100 °C and blue curve represents MC sample annealed at room temperature. ....46

**Figure 3. 4** (a) Measured optical transmission of a 10- $\mu\text{m}$ -thick MC film. Inset photo shows a hand-held MC film placed in front of a computer screen, illustrating high optical transparency. (b) AFM surface height profile of fabricated MC substrates with scan area of 20  $\mu\text{m}$  \* 20  $\mu\text{m}$ . (c) A phot showing a flexible MC film bended by fingers. (d) Measured bond strength of MC samples with or without thermal soldering. (e) Thermal gravimetric analysis of fabricated MC substrates showing alternation of water content with different temperatures (f) A SEM image of cross-section of laminated MC substrates annealed by heating at 100 °C. (g) A SEM image of cross-section of laminated MC substrates annealed at room temperature. ....48

**Figure 3. 5** (a) Schematic illustration of critical steps for fabrication of parylene stencil. (b) A photograph showing fabricated transient RFID tag based on AgNWs and MC and the inset image showing a RFID device deformed by hand (c) Measured height profile of patterned AgNW traces on top of a silicon wafer. (d) SEM-EDS elemental analysis of fabricated transient antenna device. Yellow, red and blue represent chloride (parylene), carbon (MC), and silver (AgNWs), respectively. (e) Measured return loss (S11) of transient RFID device in ambient dry environment. ....49

**Figure 3. 6** Measured height profile of fabricated parylene stencil mask used for subsequently patterning nanowires. ....50

**Figure 3. 7** SEM-EDS elemental mapping showing different constituent materials including AgNWs in blue (a), MC in red (b), and parylene in yellow(c). ....51

**Figure 3. 8** (a) A SEM image showing percolating conductive AgNW network. The inset photograph depicting a bottle of 4% (w/v) AgNW suspension used for solution casting. (b) A SEM image of patterned AgNW traces on top of a clean silicon wafer. (c) Measured resistance of patterned AgNW circuits processed at different temperatures. (d) Measured results showing the correlation between antenna resistance versus amplitude of S11 parameter and Q factor. ....53

**Figure 3. 9** Measured S11 of MC-based RFID device in ambient dry environment (a) and immersed in warm solution (b).....55

**Figure 3. 10** (a) Experimentally measured return loss of a transient RFID antenna in warm/cold water. (b) Stability test showing the variation of amplitude of S11 over 24 h in 50 °C water bath. (c) Thermally triggered transient behavior that shows dramatic S11 change due to a cooling trigger, occurring at 38 °C. (d)-(f) A set of photographs that visualize morphology alteration of transient RFID antenna in a water bath at 50, 38, and 22 °C.....57

**Figure 4. 1** (a) Molecular structure of PE, PVC, PVDF ( $\alpha$  &  $\beta$  phase) and PVA. (b) Schematic of electrospinning setup. (c) An SEM micrograph of a PVDF nanofiber. (d) An SEM micrograph of a PVDF nanofiber suspended over a Si trench. (e) An SEM micrograph of a PVDF nanofiber suspended on thermal measurement device. (f) Optical image showing the laser focused on individual nanofiber for Raman measurement.....60

**Figure 4. 2** (a) Measured thermal conductivity of PE nanofibers with different molecular weights in the temperature range of 70-320 K. (b) Measured thermal conductivity of PE nanofibers at 200 K as a function of the square root of the molecular weight. The green curve is a fit from a model that considers the anisotropic heat flux along and across the molecular chains,<sup>161,162</sup> and the red as well as blue lines are the calculated results when  $\alpha = 0$  or 0.001 (bulk PE), respectively. (c) Raman spectra acquired for PE nanofibers with Mw of 3,000,000, 420,000, and 125,000, respectively. (d) The calculated intensity ratio of I1416/I1300 group, indicating the fraction of orthorhombic crystalline phase of PE nanofibers, increases with molecular weight. The error bars indicate the standard deviation of the intensity ratio of I1416/I1300 group measured from several nanofibers. ....64

**Figure 4. 3** Polarized Raman spectra of (a) PVA, (b) PVDF, and (c) PVC nanofibers with the laser beam polarized parallel (the red curve) and perpendicular (the blue curve) to the fiber axis. (d) Values for  $P = I_{\perp\perp} / I_{\parallel\parallel}$ , a ratio that semi-quantitatively characterizes the molecular orientation in PVA, PVDF, and PVC nanofibers. ....67

**Figure 4. 4** (a) Comparison of measured thermal conductivity of electrospun PE, PVA, PVDF, and PVC nanofibers. (b) Measured Young's moduli of PVA, PVDF and PVC nanofibers of different diameters. ....69

**Figure 5. 1** Synthesis process for the production of [<sup>18</sup>F]fallypride.....78

**Figure 5. 2** (a) A photograph of the microfluidic chip with an American twenty-five cent coin placed above. (b) A schematic illustration of the microfluidic chip employed for [<sup>18</sup>F]fallypride production, including a [<sup>18</sup>F]fluoride concentration column, fluorination reaction cavity and [<sup>18</sup>F]fallypride purification column. (c) A photograph of anion exchange beads trapped inside a microchannel by 10  $\mu$ m gap PDMS pillars. (d) A photograph of reverse phase C<sub>18</sub> microparticles trapped inside a microchannel with 40  $\mu$ m gap PDMS pillars. ....79

**Figure 5. 3** Schematic representation of the steps used for the production of [<sup>18</sup>F]fallypride on our integrated microfluidic chip. The six steps shown are: (a) concentrate [<sup>18</sup>F]fluoride using anion-exchange column, (b) release trapped [<sup>18</sup>F]fluoride off the column and transfer into reaction cavity, (c) evaporate to achieve an anhydrous environment by heating and N<sub>2</sub> drying, (d) [<sup>18</sup>F]fallypride fluorination, (e) isolate undesired products using purification column, (f) collect purified [<sup>18</sup>F]fallypride off chip. ....82

**Figure 5. 4** Photograph of on-chip reaction cavity with no reagent inside (a) and after water evaporation (b). ....84

<b>Figure 5. 5</b> The relationship between precursor concentration and fluorination efficiency. ....	88
<b>Figure 5. 6</b> (a) Crude radio-HPLC of [ <sup>18</sup> F]fallypride synthesized inside the reaction cavity. (b) Radio-HPLC of [ <sup>18</sup> F]fallypride eluted from the on-chip purification column.....	89
<b>Figure 5. 7</b> Radio-HPLC analysis of the waste mixture passed through the C <sub>18</sub> column. This injection was taken using the mixture solution flowing out from the purification column after labelling reaction. 95% [ <sup>18</sup> F]Fluoride was washed off the purification column, and only 5% [ <sup>18</sup> F]fallypride was lost at this step. ....	90
<b>Figure 5. 8</b> (a) PET image of rat brain using [ <sup>18</sup> F]fallypride produced in a microfluidic chip. (b) The variation of [ <sup>18</sup> F]fallypride concentration imaged in the microPET for 2 hours. ....	92
<b>Figure 5. 9</b> A typical UV spectrum for the purified [ <sup>18</sup> F]fallypride, showing product peak at 11.11 min. The presence of minor impurities is observed throughout the spectrum.....	94
<b>Figure 6. 1</b> Schematic representation of a chip designed for the synthesis of <sup>68</sup> Ga-PSMA, including an SCX column, SAX column, passive mixing module and reactor for the labelling reaction.....	99
<b>Figure 6. 2</b> Photographs of the fabricated microfluidic device for the radiosynthesis of <sup>68</sup> Ga-PSMA-11 (a), SCX (b) and SAX (c) resins trapped inside microchannels, and the entrance of mixing module (d) with diamond-shape obstructions inserted throughout the zigzag microchannel.....	101
<b>Figure 6. 3</b> Schematic diagrams showing the three sequential labelling steps: (a) concentration of generator-obtained <sup>68</sup> Ga <sup>3+</sup> using an on-chip SCX column, (b) <sup>68</sup> Ga <sup>3+</sup> elution from the SCX, followed by trapping on the SAX in the form of [ <sup>68</sup> GaCl <sub>4</sub> ] <sup>-</sup> , (c) release <sup>68</sup> Ga <sup>3+</sup> with water, followed by mixing with PSMA precursor to accomplish the formation of <sup>68</sup> Ga-PSMA.....	103
<b>Figure 6. 4</b> The relation between volume of HCl and both SCX release efficiency and SAX trap efficiency.....	107
<b>Figure 6. 5</b> Experimental evaluation of the mixing performance using the combination of inserted obstructions and zigzag microchannels. The captured fluorescent images indicate mixing results at inlet (a), middle (b) and outlet (c), respectively, which are in good agreement with corresponding numerical simulation.....	109
<b>Figure 6. 6</b> Normalized fluorescent intensity for characterization of mixing performance after passing through the on-chip mixing module.....	110
<b>Figure 6. 7</b> Comprehensive investigations regarding optimal reaction conditions for <sup>68</sup> Ga labeling reaction using the developed microfluidic device. Several parameters including reaction time (a), reaction temperature (b), precursor concentration (c), and pH (d) are studied. ....	111
<b>Figure 6. 8</b> Analytical TLC profile of <sup>68</sup> Ga-PSMA synthesized using the microfluidic chip, showing quantitative conversion.....	112
<b>Figure 6. 9</b> Analytical HPLC trace of <sup>68</sup> Ga-PSMA. The top blue curve and bottom red curve indicate chemical and radiochemical purity, respectively. The retention time of <sup>68</sup> Ga-PSMA is 7.88 min. ....	113

# Chapter 1 Introduction

## 1.1 Background

About 60 years ago, the physicist Richard Feynman gave a remarkable speech envisioning the significance of manipulating matter at small scales. Over the past half a century, research efforts in the realm of micro- and nanotechnology not only advance our fundamental understanding of macroscopic phenomena but also enable the emergence of numerous revolutionary applications, such as quantum computers,<sup>1</sup> high-resolution *in vivo* imaging,<sup>2</sup> and targeted cancer therapy.<sup>3</sup>

When the size of fundamental building blocks shrinks down, unique properties or behaviors that are not attainable in traditional bulk formats begin to occur. For example, while bulk monocrystalline silicon, the most widely used semiconducting material, is generally considered as a rigid and brittle material, silicon nanomembranes (SiNMs), whose thickness is a few hundred nanometers, are mechanically flexible, which enables novel applications in the field of photonics, electronics and healthcare.<sup>4</sup> By leveraging these favorable attributes, it is hence feasible to construct novel electronics based on conventional inorganic semiconductors yet in unconventional forms (e.g. nanoparticles, nanomembranes and nanorods). Such examples include applications ranging from fingertip tactile sensing,<sup>5</sup> stretchable electronics<sup>6,7</sup> to human-machine interfaces.<sup>8</sup> Because of the improved capability to synthesize small structures, engineered nanoparticles with well-defined dimensions and shapes have found increasing use in biomedical areas such as disease diagnosis and precise therapy.<sup>9</sup> For example, gold nanoparticles, due to their intriguing optical properties, such as enhanced surface plasma resonance and Raman scattering, have been identified and investigated as novel agents for cancer imaging and



photothermal therapy.

Nanocomposites consisting of materials with disparate properties have attracted substantial research attention because such compounds possess many attractive characteristics that each individual material does not exhibit. For instance, incorporating micro/nano-fillers into polymeric matrices can yield compounds that either combine the advantageous attributes of each individual component or enhance particular properties of interest. For example, Stankovich et al. described a general approach to prepare graphene-polymer composites (electrical conductivity  $\sim 0.1 \text{ S m}^{-1}$ ) via complete exfoliation of graphite and dispersion of individual graphene sheet.<sup>10</sup> Another demonstration reported by Moisala et al. is the development of thermally and electrically conductive epoxy composites by adding single/multi-walled carbon nanotube into the insulating matrix.<sup>11</sup>

Furthermore, by choosing suitable materials, high-performance electronics that can physically disappear after a predetermined timeframe provide feasible routes to alleviate environmental issues arising from consumer electronic waste. For instance, employing degradable composites including silk, magnesium and SiNMs, Hwang et al. reported transient electronic systems composed of various basic electronic elements that dissolve in a controlled manner upon exposure to water.<sup>12</sup> Taking advantage of nanocomposites with unique properties or behaviors, there are opportunities to construct novel electronic systems that physically disappear when no longer needed. Recently, transient electronics, whose defining feature is to utilize nanocomposites that are able to disintegrate upon external stimuli, have gained tremendous attention due to its widespread applications ranging from temporary implantable devices to environmental sensors.<sup>13</sup> Since transient systems depend primarily on the choice of constituent materials, the development of composites that eventually disappear after a

predetermined timeframe plays a critical role in advancing the field of transient electronics. For example, Acar et al. reported a transient polymer composite composed of PVA with the addition of gelation or sucrose, which allows controlled dissolution rate simply by adjusting fillers concentration.<sup>14</sup> Building on biodegradable materials, Huang et al. demonstrated a transient printed circuit boards (PCB) that consists of layers of transient metal traces (e.g. magnesium (Mg), tungsten (W), zinc (Zn)) and dielectric interlayers (e.g. sodium carboxymethylcellulose (Na-CMC) and polyethylene oxide (PEO)).<sup>15</sup> Such device was able to probe ambient temperature in a wireless manner and dissolve within 10 minutes after immersion in water. To date, the majority of transient electronics systems are based on degradation/dissolution of materials. Hence, there are opportunities to broaden the scope and applicability of transient systems by developing stimulus-responsive materials. By employing stimulus-responsive composites, it enables the construction of novel transient systems that can be triggered to disintegrate upon a particular external signal such as pH, light and mechanical stress. For instance, Park et al. reported a thermal-triggered transient electronics where wax layers with corrosive acid encapsulated inside microdroplets are used as device substrates.<sup>16</sup> When exposed to external heat source, the wax layer melted and released the encapsulated acid, which sequentially caused the destruction of above electronic components. Hernandez et al. also reported a novel architecture of microfluidic transient systems that allowed selective etching of constituent components of interest.<sup>17</sup> When integrated with internal clocks, photodetectors or humidity sensors, on-demand transience behavior can be wirelessly activated.

As illustrated by abovementioned examples, the capability to shrink down the size of functional structures plays a critical role in the development of novel high-performance electronic systems. Consequently, extensive efforts have been devoted to developing relevant

techniques that allow the formation of organic/inorganic structures with desired characteristics.<sup>18,19</sup> For example, Molenkamp et al. employed well-oriented mesoporous silica as a template to produce semiconducting polymers with preferential orientation for optoelectronic applications.<sup>20</sup> Sundrani et al. reported an alternative hierarchical approach to fabricate arrays of aligned nanoscale polymer fibers where silicon nitride of various depths were used to create high-aspect-ratio cylindrical polymer domains.<sup>21</sup> Among those reported approaches, electrospinning represents another facile and versatile method that have been widely employed to generate nanostructures with critical dimensions ranging from several micrometers to tens of nanometers.<sup>22</sup> More detailed discussion regarding the electrospinning mechanism and apparatus can be found in the later section. Beyond initial efforts on understanding how to control and optimize the electrospinning process, electrospun nanofibers in the past decades have found extensive applications in a wide scope of research fields. For example, Wu et al. reported a facile approach to produce highly transparent (~90%) and conductive (~2 Ω/sq) electrodes via depositing a thin layer of metal (~80 nm) onto sacrificial electrospun fiber network.<sup>23</sup> Superior to indium tin oxide, the as-fabricated electrode exhibited excellent mechanical properties (e.g. bendability, flexibility) after repeated stretching and bending cycles. Additionally, Wang et al. developed an optical sensor consisting of electrospun poly(acrylic acid)-poly(pyrene methanol) (PAA-PM) fibers for detecting metal ions ( $\text{Fe}^{3+}$  and  $\text{Hg}^{2+}$ ) and 2,4-dinitrotoluene (DNT).<sup>24</sup> Similarly, Kim et al. developed a  $\text{NO}_2$  gas sensor based on  $\text{TiO}_2$ /poly (vinyl acetate) composite nanofibers (200-500 nm diameter) that possessed excellent sensitivity (833% change in resistance) when exposed to 500 ppb  $\text{NO}_2$  at 300 °C. Besides aforementioned applications, electrospun nanofibers can act as the building blocks for biosensors by converting specific biological signals of interest into electrical outputs. Sawicka et al. developed a urea-sensitive

system by leveraging urease-immobilized electrospun PVP fibers.<sup>25</sup> Patel et al. employed electrospinning to encapsulate horseradish peroxidase enzymes into porous electrospun fiber matrix. Due to small diameters (100-200 nm), high level of porosity (2-4 nm) and a large surface area, the resulting silica fibers were very promising as the building-blocks for enzyme-based biosensors.<sup>26</sup>

From the perspective of fluid manipulation, the electrospinning process allows transformation from macroscopic liquid/melted suspension into micro- and nanoscale structures. Similarly, microfluidics, a technique that generally focuses on the control of fluid using micro- or nanochannels, offers another distinctive approach that holds potential to advance a variety of fields.<sup>27</sup> Fluid flowing in micro- or nanochannels exhibit many desirable features that are not attainable in macroscopic scale. For example, the ability to manipulate immiscible fluids using microfluidic system enables the generation of monodisperse bubbles or droplets with diameters in tens of nanometers, which have been adopted for generation of polymer particles, emulsions and foams.<sup>28</sup> Since microfluidic devices typically require extremely low amounts of samples and reagents, such characteristics provide feasible approaches to achieve precise and cost-efficient analysis of expensive or hazardous samples, which occurs frequently in the field of biology and chemistry.

In addition, another intriguing benefit of microfluidics is to implement multistep chemical/biological reactions in a small microfluidic chip, also referred as “lab on a chip”. The development of various lab-on-chip systems have advanced numerous fields such as chemical/biological analysis, point-of-care diagnostics and therapeutics.<sup>29</sup> A remarkable example reported by Lee et al. was an automated pneumatic microfluidic device for rapid and efficient production of positron emission tomography (PET) radiotracers.<sup>30</sup> Starting from  $\sim 1 \mu\text{l}$  of

[<sup>18</sup>F]fluoride mixture, the whole [<sup>18</sup>F]FDG production process was completed within 14 min (typically ~2 hours in practical scenario) and the amount of resulting product were sufficient for several mouse experiments. To briefly sum up, by introducing three disparate projects that leverage or investigate micro- and nanoscale structures, this dissertation aims to reveal novel behaviors and properties closely associated with small structures. In the following section, I will overview three research areas including transient electronics, electrospun polymeric nanofibers with enhanced thermal conductivities and microfluidics for efficient PET radiotracer production.

## **1.2 Overview of Transient Electronics**

Transient electronics represent a unique platform for circuitry in which physical disintegration and disappearance occurs in a controlled fashion either after a predetermined time scale or a desired task has been performed. While long term physical and functional reliability is a distinctive feature of the majority of traditional integrated circuit electronics, there are emerging needs for functional electronics that are compatible with this envisioned transient operation. Electronics exhibiting transient behavior have recently attracted attention due to their broad potential in areas such as degradable energy harvesters, zero-waste electronic systems and temporary implantable biomedical devices.<sup>31-33</sup> Empowering diverse high-performance electronics with the ability to degrade or disappear as needed encourages the pursuit of novel techniques suitable for the construction of transient systems. Much of the work in this area has been performed by John Rogers and colleagues. For example, they have reported highly-integrated transient systems (along with thorough description of the constituent materials, fabrication techniques, device components and theoretical analysis).<sup>12</sup> As shown in Figure 1.1a, various electronic components (including resistors, diodes, inductors, capacitors, transistors and conductive interconnectors) were all integrated on a thin silk film to form a high-performance

circuit that can dissolve in water. Figure 1.1b schematically illustrates the different constituent materials used for construction of this transient circuitry. Magnesium (Mg) is used to form conductive interconnections and electrodes, magnesium oxide (MgO) as a dielectric, silicon nanomembrane (Si NM) as a semiconductor, and silk as the device substrate. The dissolution behavior in water and macroscopic morphological changes are presented in Figure 1c. The device disintegration occurred at a measurable rate, and the whole device dissolved in water within 10 minutes.

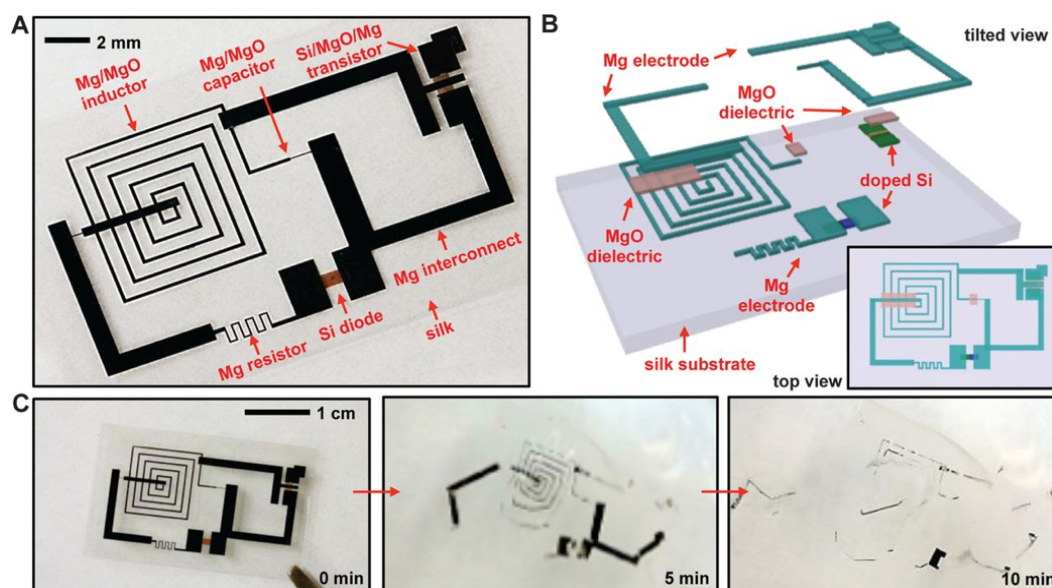


**Figure 1. 1** Demonstration of transient electronics. (a) Images of a device that includes transistors, diodes, inductors, capacitors, and resistors, with interconnects and interlayer dielectrics, all on a thin silk substrate. (b) Exploded-view schematic illustration, with a top view in the lower right inset. (c) Images showing the time sequence of dissolution in DI water.

The disintegration of transient systems is fundamentally related to the intrinsic properties of the materials employed to form functional devices. In other words, to further develop this field of devices, it is critical to study diverse materials capable of achieving transience in a defined

manner, such as solubility in water or biofluids, disintegration upon external stimuli (heat, humidity, light intensity and so on) and self-destruction after predetermined time scales. Three categories of materials are required to form fully functional transient circuitry: conductors, semiconductors and insulating substrates. First and foremost, conductive materials, typically working as electrodes or interconnectors in electronics, are one of the most essential components. Unlike bulk metals, certain thin metal films, such as Mg, Zn and so on, are able to dissolve in water or biofluids due to hydrolysis, and the corresponding time scales for transience (depending on the thickness of metal films), range from hours to months or years. As a result, understanding the dissolution behavior of thin metal films is of primary importance for designing and fabricating high-performance transient electronic devices. Yin et al. performed systematic investigation of the dissolution behavior of numerous metals (Mg, Zn, Fe, W and Mo) in de-ionized water or simulated body fluids.<sup>34</sup> Figure 1.2 shows the changes in electrical resistance as a function of time for various metals immersed in Hank's solution and in DI water at body temperature. This work comprehensively elucidates the dissolution behaviors and mechanisms of various metals, which will help engineers choose appropriate conductive materials when designing transient electronics.

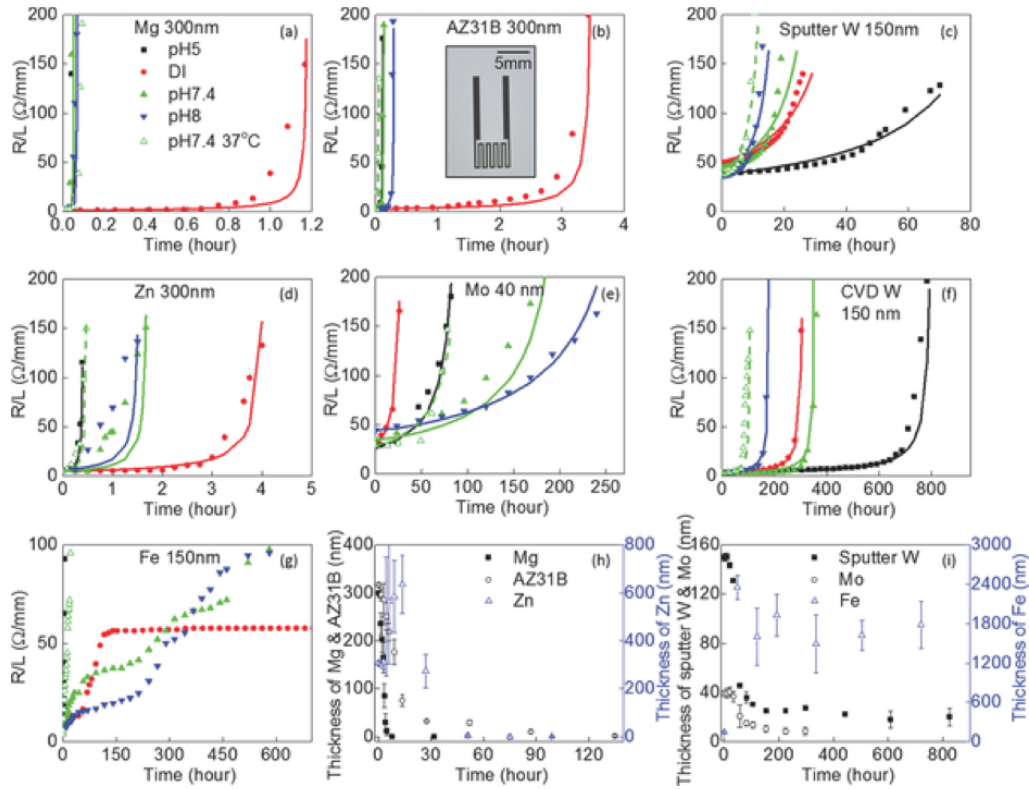


**Figure 1. 2** Changes in resistance of serpentine thin film traces as a function of time during dissolution in Hanks' solution and in DI water, for cases of (a) Mg (300 nm); (b) AZ31B Mg alloy (300 nm); (c) sputter deposited W (150nm); (d) Zn (300 nm); (e) Mo (40 nm); (f) CVD W (150 nm); (g) Fe (150 nm); (h) Mg, AZ31B Mg alloy, and Zn; (i) Mo, Fe and sputter deposited W.

In addition to conductive metals, semiconductor materials are an important class of constituent materials for transient electronics due to their essential role in various active electronic devices, such as transistors, light-emitting diodes, temperature and strain sensors. Of all the available semiconductor materials, Si has many distinct advantages and thus it has been widely used in well-established integrated circuits, and techniques used to process, transfer and integrate silicon nanostructures are quite mature. While bulk Si is generally not considered soluble in water (partly due to the presence of an oxide layer on its exterior surface), hydrolysis in water or biofluids can still take place at a noticeable rate when Si is in films with thicknesses



on the micro/nanoscale. Moreover, Si nanomembranes (NMs), when implanted in live animals, not only show good functional behavior, but are also biocompatible. All these attractive features, therefore, make Si NMs an ideal semiconductor material for transient electronics. Yin et al. conducted both experimental and theoretical studies on the underlying hydrolysis mechanisms of Si NMs, with the goal of future application in bioresorbable electronics.<sup>35</sup> Numerous factors including temperature, pH, doping level, and even the presence of ions/proteins, affected the rate of the hydrolysis reaction. Hwang et al. reported the use of single-crystal Si NWs for high-performance transient electronics, and also characterized the corresponding dissolution behavior due to hydrolysis.<sup>36</sup> As shown in Figure 1.3, the dissolution rate of Si NMs at physiological temperature was spatially uniform when immersed in bovine serum (PH=7.4) and the overall time required for complete dissolution is closely linked with the thickness of constituent Si NMs. Additionally, Kang et al. conducted comprehensive studies of the hydrolysis-induced dissolution on semiconductors with different dopant types and dopant concentrations.<sup>37</sup> As an alternative to utilizing Si NMs as semiconductor materials, Lei et al. recently developed totally decomposable polymer semiconductors based on imine chemistry for fully disintegrable transient electronics, widening the available options for semiconductor materials for transient systems.<sup>38</sup>

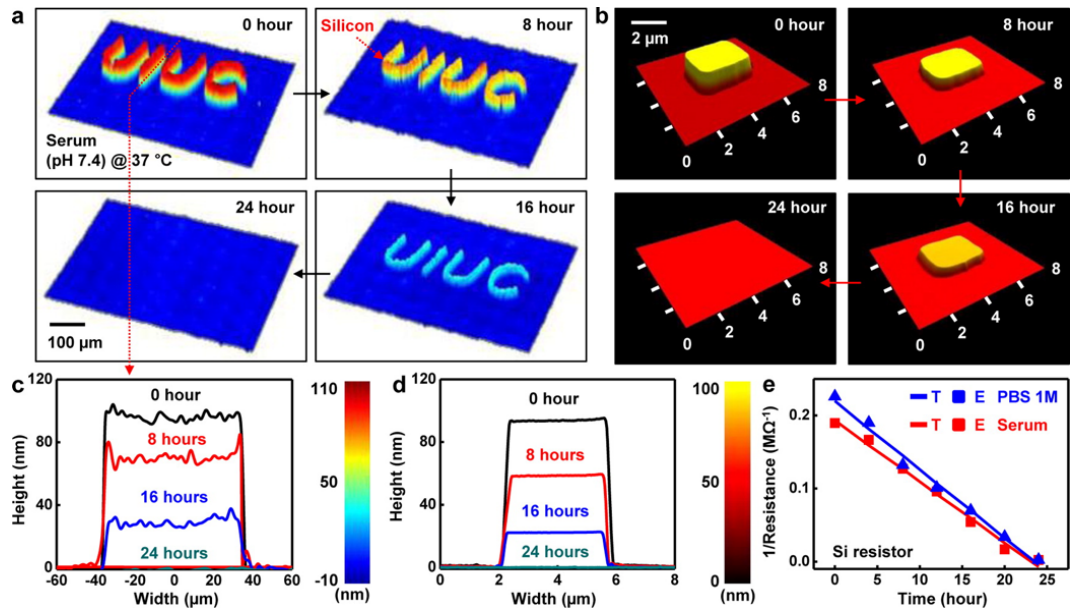


**Figure 1.** 3 Images of Si NMs at various stage of dissolution in bovine serum (pH~7.4 at physiological temperature (37 °C) measured by (a) DPM and (b) AFM. Thickness profiles extracted from the (c) DPM and (d) AFM images in (a) and (b). (e) Theoretical and measured changes in resistance of a serpentine shaped Si NMs after various times of immersion in PBS (blue) and bovine serum (red) at body temperature.

Another distinguishing characteristic of traditional electronics, such as printed circuit boards (PCBs), are their mechanical rigidity and long-term functionality, generally far exceeding the lifetime needed for the intended application. There are opportunities, however, for materials that are able to dissolve, disintegrate or disappear in mild environments in a controlled manner. In this scenario, polymers whose characteristics include bendability, flexibility, conformability, and biocompatibility are promising candidates to enable behaviors and properties that cannot be provided by traditional materials. A large number of natural or synthetic polymers, such as poly(vinyl alcohol) (PVA), polyvinylpyrrolidone (PVP), polylactideglycolic acid (PLGA), polylactic acid (PLA), and silk have been employed as the encapsulation layer for biomedical applications or as the supporting substrate for transient electronics. For example, the presence of

hydroxyl groups in the monomer structure enables PVA to work as a suitable substrate material for degradable or bioresorbable electronics. Jin et al. reported single-walled carbon nanotube field effect transistors (FETs) where PVA was utilized as a water-soluble substrate.<sup>39</sup> **Figure 1.4** depicted the dissolution and disintegration of the FETs on a PVA film. The dissolution of a 30  $\mu\text{m}$  thick PVA film took place instantly upon its contact with water and the whole substrate completely dissolved and disappeared after 30 min. As noted before, the capability to controllably disintegrate is critical for producing transient systems that respond to external stimuli. Acar et al. reported a means to achieve programmable degradation and dissolution simply by introducing gelatin or sucrose into a PVA composite.<sup>14</sup> The addition of gelatin resulted in a prolonged dissolution time scale while the addition of sucrose led to a reduced dissolution time scale.

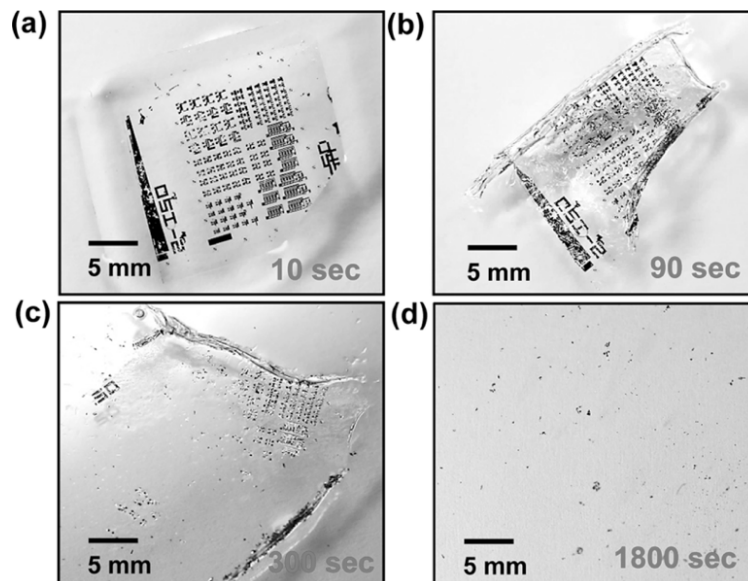


**Figure 1. 4** Images of dissolution and degradation of SWNT FETs on a PVA substrate in water at various stages, (a) 10s, (b) 90s, (c) 300s, (d)1800s.

There are plenty of cases using other polymers for transient electronics applications. Hwang et al. employed a thin natural silk film as the substrate for transient systems.<sup>12</sup> Kang et al. reported implantable silicon-based brain sensors using a 30 $\mu$ m-thick PLGA membrane as the degradable substrate.<sup>40</sup> Fu et al. used the electrospun PVP membrane as a degradable separator for a transient lithium ion battery where all components were able to fully dissolve in water within minutes due to a triggered cascade reaction.<sup>41</sup>

To date, the vast majority of transient electronics have behavior enabled by the unique properties of the materials used for construction, materials that are able to degrade or dissolve in water or biofluids. However, there is an emerging need for transient electronics that exhibit disappearance induced by some external stimulus, such as temperature, humidity, light and so on. To expand the versatility of transient electronics technology, recent efforts have demonstrated several alternative disintegration modes where the variation of external factors triggers the degradation or self-destruction of electronic devices. For example, Park et al. reported a thermally triggered transient electronic device employing heat to trigger the destruction of a polymer substrate.<sup>16</sup> In **Figure 1.5**, when exposed to a heat source, the melting of wax coated above electronics released methanesulfonic acid microspheres encapsulated inside, and the patterned Mg electrodes and cPPA substrate were subsequently destroyed due to acidic degradation and depolymerization, respectively. Another example of triggered transient electronics was reported by Hernandez et al.<sup>42</sup> In this work, polymer 2-(4-methoxystyryl)-4,6-bis(trichloromethyl)-1,3,5-triazine (MBTT), a photo-acid generator (PAG), linked with the backbone of cyclic poly(phthalaldehyde) (PPA) served as a supporting substrate. When exposed to UV light, the MBTT additive generated a highly reactive Cl radical that captured a hydrogen from its surroundings to form hydrochloric acid (HCl), and as-generated HCl reacted with cPPA

to trigger the depolymerization by cleaving the acetal backbone of cPPA. Moreover, it also suggested that transience rates were tunable by adjusting either the PAG concentration or the intensity of applied UV light.

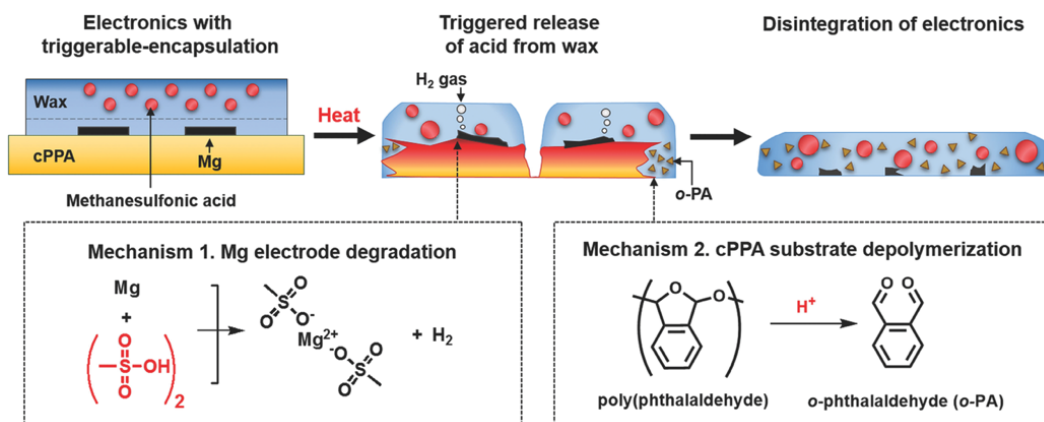


**Figure 1. 5** Heat-triggerable transient electronics coated with wax containing acid dispersions. Release of MSA by melting a wax coating leads to rapid electronic destruction by acidic degradation of Mg electrodes on glass. In addition, using a cyclic poly(phthalaldehyde) (cPPA) substrate affords a more rapid destruction of the device due to acidic depolymerization of cPPA.

### 1.3 Overview of PET Radiotracer Synthesis using Microfluidic Devices

Positron emission tomography (PET) is a non-invasive nuclear medical imaging technique that has been broadly employed to assist in diagnostic and therapeutic procedures.<sup>43</sup> PET radiotracers are composed of specific biological molecules labelled with short-lived radionuclides, such as <sup>11</sup>C, <sup>18</sup>F, <sup>68</sup>Ga and are engineered to accumulate at areas of interest inside the patient after injection. Utilizing a PET scanner, three-dimensional images indicating specific physiological activities can be subsequently constructed. Additionally, PET technology has also been applied to aid in preclinical studies to understand biochemical processes and develop novel drugs. While plenty of PET radiotracers have been discovered in research settings, only a limited number of those are currently produced for daily clinic usage due to both the centralization of resources needed to produce radiopharmaceuticals and the

complexity of the synthetic process. The current development of equipment for synthesizing PET probes suffers from many challenges, including the need to complete a complex multistep chemical processes in limited time frame (due to radioactive decay) and the strict criteria for human imaging. Therefore, to eliminate current bottlenecks for producing PET radiotracers, further development and simplification of the synthetic setup for producing PET probes on demands is critical.

Microfluidic technology has been identified as a promising means for the synthesis of PET radioactive tracers within the last decade.<sup>44</sup> The numerous advantages of microfluidic devices (including high surface to volume ratio, fast thermal and mass transport rate, improved reaction efficiency and resulting yield) are quite useful when applied to radiopharmaceutical synthesis, and thus have motivated significant research effort on the development and optimization of low-cost and efficient microfluidic devices for PET radiotracer production. Experimental results published by several groups have demonstrated benefits that can result from using microfluidic devices. For example, Lee et al. reported a microfluidic device in a highly integrated configuration for the production of [<sup>18</sup>F]FDG, a widely used PET tracer for imaging oncology.<sup>30</sup> As shown in Figure 1.7, five sequential processes including [<sup>18</sup>F]fluoride concentration, water evaporation, radiofluorination, solvent exchange and hydrolytic deprotection were all performed on the chip. Moreover, the production of [<sup>18</sup>F]FDG was completed within 14 min, which was a significant improvement compared to conventional automated synthesis modules (over 2 hours). However, polydimethylsiloxane (PDMS), a commonly used material for microfluidic chip, is not chemically resistant to most organic solvents. Besides, PDMS may react with [<sup>18</sup>F]fluoride ion and reduce the overall radiochemical yield.<sup>45</sup> To avoid the limitation arising from PDMS, several groups have explored other materials as alternatives for microfluidic chip fabrication. Zacheo et al. evaluated the radioactivity resistance of several polymeric materials, such as PDMS, SU-8 and Teflon coated on PDMS.<sup>46</sup> Experimental results revealed that SU-8 and Teflon coated hard surfaces exhibited better performance in terms of radioactivity resistance and chemical stability. Another attempt reported by Gillies et al. developed a simple microreactor composed of three layers of thermally bonded glass plates with holes on the top plate as inlets, an etched mixing disk for reaction, and outlets on the side.<sup>47,48</sup> As a

proof-of-principle, [ $^{18}\text{F}$ ]FDG was synthesized using two devices linked in sequence, where the first device was designed to carry out the [ $^{18}\text{F}$ ]fluorination and the second device was employed to achieve deprotection.

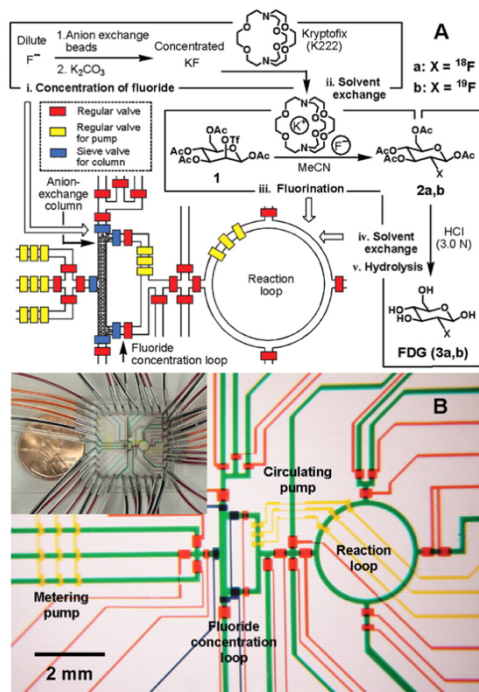


**Figure 1. 6** (A) Schematic representation of a chemical reaction circuit used in the production of 2-deoxy-2-fluoro-d-glucose (FDG). Five sequential processes are shown: (i) concentration of dilute fluoride ion with the use of a miniaturized anion exchange column located in a rectangle-shaped fluoride concentration loop, (ii) solvent exchange from water to dry MeCN, (iii) fluorination of the d-mannose triflate precursor 1, (iv) solvent exchange back to water, and (v) acidic hydrolysis of the fluorinated intermediate 2a (or 2b) in a ring-shaped reaction loop. Nanogram amounts of FDG (3a, 3b) are the final product. The operation of the circuit is controlled by pressure-driven valves, with their delegated responsibilities illustrated by their colors: red for regular valves (for isolation), yellow for pump valves (for fluidic metering circulation), and blue for sieve valves (for trapping anion exchange beads in the column module). (B) Optical micrograph of the central area of the circuit. The various channels have been loaded with food dyes to help visualize the different components of the microfluidic chip; colors are as in (A), plus green for fluidic channels. Inset: Actual view of the device; a penny (diameter 18.9 mm) is shown for comparison.

There are several procedures involved in routine [ $^{18}\text{F}$ ]fluoride-labelled PET radiotracer production, including [ $^{18}\text{F}$ ]fluoride concentration, solvent exchange, evaporation, radiolabelling reaction,

deprotection (optional) and purification.<sup>49</sup> Nonetheless, most research exploring microfluidic technology for PET tracer production has focused primarily on a single step, the radiolabelling reaction. For example, recent studies by Chen et al. and Ding et al. reported a digital electrowetting-on-dielectric (EWOD microfluidic device ) that can synthesize a variety of <sup>18</sup>F-labelled PET tracers.<sup>50-53</sup> As shown in Figure 1.8, the idea of using electric potentials to manipulate droplets (micro/nanoliter in volume) on a dielectric surface does not require mechanical valves, pumps or channels, which eliminates the issue of [<sup>18</sup>F]fluoride loss due to unwanted reaction between [<sup>18</sup>F]fluoride ion and PDMS. The small volume used in EWOD chip along with the open-to-air configuration allows for rapid evaporation, solvent exchange and reaction kinetics and thereby increases the specific activity (radioactivity per mass of tracer) of resulting products. To prove the utility of this platform, four diverse radiotracers including [<sup>18</sup>F]FDG, [<sup>18</sup>F]FLT, [<sup>18</sup>F]SFB and [<sup>18</sup>F]fallypride were synthesized for multiple runs.<sup>51</sup>

In addition to EWOD-based microfluidic systems, Bejot et al. reported a batch microfluidic device used to synthesize [<sup>18</sup>F]SFB.<sup>54</sup> Though [<sup>18</sup>F]fluoride concentration and purification was performed by conventional off-chip means, the relatively short synthesis time (25 min) and improved final yield (55±6%) successfully illustrate how microfluidic technology is advantageous for PET probe production compared to clinical modules in current use. Additionally, Steel et al. developed an automated glass microfluidic device that enables rapid PET radiosynthesis.<sup>55</sup> Preliminary experimental results showed that sequential [<sup>18</sup>F]fluorination and deprotection of [<sup>18</sup>F]FDG was accomplished in 18 min with a yield of 40%. Moreover, 1 Ci of [<sup>18</sup>F]fluoride was loaded without any observed radiolysis in the automated microfluidic device, indicating the potential for delivering patient doses (typically ~10 mCi).



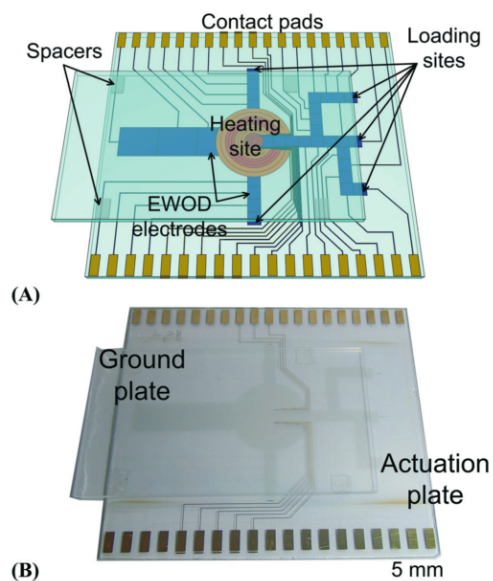


**Figure 1. 7** EWOD chip designed and fabricated for tracer synthesis. (A) Schematic of the chip, showing the actuation glass plate patterned with regular EWOD electrodes (blue), multifunctional electrodes named heating site (orange and red), and electric contact pads along the two edges, as well as the electrical ground glass plate assembled on top. (B) A picture of the fabricated chip, showing the EWOD and multifunctional electrodes (slightly darker) and gold connection lines and contact pads (yellow).

More recently, several groups have advanced microfluidic technology for PET probe synthesis to a level that, starting from [ $^{18}\text{F}$ ]fluoride obtained from cyclotron, the resulting radiotracers meet strict requirements (e.g. chemical and radiochemical purity, specific radioactivity and quality control criterion) to allow human PET imaging. Lebedev et al. reported the first case of PET human doses produced via a microfluidic device and a human PET scan was provided using the resulting radiotracer.<sup>56</sup> The key features of their microfluidic device included a fluoride concentration system and a microfluidic batch reactor. HPLC-based purification and reformulation units were integrated in the device. It is noteworthy that reported microfluidic system can achieve up to 3 full production runs in a day, which would significantly aid in on-demand PET radiotracer production. Another example of employing microfluidics for

dose-on-demand synthesis of PET radiopharmaceuticals was reported by Arima et al.<sup>57</sup> Their integrated microfluidic platform exhibited yields comparable to those commercially available via a vessel-based setup (40-80%) and enabled clinicians to obtain radiopharmaceuticals as needed within a few minutes. Moreover, the flexible modular microfluidic platform can be easily modified and applied to the synthesis of diverse PET radiotracers.

## Chapter 2 Thermoresponsive Conductive Composites for Transient Electronics

### 2.1 Introduction

Transient electronics are an emerging platform of electronic circuitry purposefully designed to disintegrate and irreversibly lose function.<sup>12</sup> The transient system is fabricated so that it exhibits stable electrical behavior until a stimulus, such as light<sup>42</sup>, temperature<sup>16</sup> or a solvent<sup>34</sup>, is applied. Transient systems composed of nontoxic, decomposable, and biocompatible materials are promising platforms with applications in several areas including bioresorbable electronics,<sup>33,58,59</sup> energy storage devices<sup>41,60,61</sup>, and secure storage systems.<sup>13,62</sup> A critical aspect of a transient system is the mechanism for disintegration, which is fundamentally linked to the properties and behavior of the materials used for construction. Here, we report a type of thermoresponsive transient electronics based on entirely disintegrable and biocompatible polymers and conductive nanowires. The transient system exhibits stable electrical behavior when immersed in warm water, but quickly dissolves when the temperature of the surrounding solution drops below a threshold temperature. In other words, by utilizing polymers with thermal transitions above room temperature, we are able to fabricate a conducting composite that requires energy input (in the form of heat) to prevent irreversible dissolution and loss of function. Employing standard fabrication techniques, we have successfully fabricated various passive electronic components and multilayer devices. When dissolution was triggered by low solution temperature, these transient components exhibited a gigantic loss of electrical conductivity.

Composites formed from non-conducting polymers and conducting particles have been used for a wide variety of applications, as such systems leverage both the enhanced or unique mechanical/optical/thermal properties of the polymeric matrix and the electrically conducting

properties of the embedded particles. Examples of such composite systems include the use of conductive nanowires deposited on elastomeric and/or transparent substrates (to obtain stretchable and/or transparent conductors),<sup>63,64</sup> epoxies loaded with conductive particles (to obtain castable conductive adhesives),<sup>65,66</sup> and transient electronic systems formed from conductive particles and soluble polymers.<sup>12,38</sup> In each of these systems, the matrix serves as a binder that holds the conductive network of particles together or otherwise provides mechanical support; the resulting bulk behavior of the material is a combination of the matrix behavior (mechanical, optical, thermal, chemical) and the particle behavior (generally, electrical conductivity). In some systems, the goal is to couple response of the matrix to some environmental factors to a change in electrical performance. In particular, in transient electronic systems, the electrical behavior of the device is designed to change irreversibly as a response to some environmental change (e.g. exposure to solvent or light). In this work, we leverage the LCST behavior of certain polymers to obtain a conductive composite material that requires energy input (in the form of heat) in order to stay viable. Loss of energy input results in cooling, which subsequently results in dissolution and loss of function. While others have demonstrated materials systems wherein energy input causes destruction (e.g. using photosensitive films),<sup>16,61</sup> the composite material discussed herein is the first to require energy input to prevent destruction and loss of conductivity.

To date, the majority of transient electronics systems are based on the concept of transience induced by immersing the devices in an aqueous environment. The loss of function is due to the dissolution or destruction of construction materials.<sup>34</sup> Stimulus-responsive systems that maintain a stable state but quickly disintegrate upon exposure to a specific stimulus may enable more complex behaviors and sharper transitions between the stable, functional state and the

disintegrated state. Rogers and colleagues have investigated a range of materials to form these architectures, including Mo, Zn, W, Fe, Mg for conductive contacts, silicon nanomembranes (Si NMs) or metal oxide (e.g. ZnO) as semiconductors, and polymeric matrices such as silk fibroin, poly(vinyl alcohol) (PVA) and polyvinylpyrrolidone (PVP).<sup>[10–19]</sup> Circuitry formed from these materials slowly dissolves in aqueous environments and thus function is lost after a predetermined period of time (linked to the dimensions<sup>71</sup> and composition<sup>14,72</sup> of the device). Recently, thermally-induced transient devices have been demonstrated by Chan *et al.* using a coating of wax-encapsulated methanesulfonic acid on top of prefabricated electronic devices.<sup>16</sup> Transient devices composed of magnesium conductive traces formed on Cyclic poly(phthalaldehyde) (cPPA) films fully disintegrated within 1 minute after the heat-triggered exposure to methanesulfonic acid. Photosensitive transient systems reported by Hector *et al.* and wireless microfluidic transient systems reported by Chi *et al.* have also broadened the functionality of transient devices.<sup>17,42</sup> To add a new stimulus-responsive behavior to a transient electronic system, here we employ as a “binder” polymers that exhibit lower critical solution temperature (LCST) behavior, wherein the polymer is hydrophobic (and insoluble) above a threshold temperature and hydrophilic (and soluble) below that temperature. This allows us to form a transient electronic system that must be maintained in a warm solution to maintain function; disintegration and loss of function occur when the surrounding solution cools below a threshold temperature.

Here, we demonstrate that both methyl cellulose (MC) and Poly(N-isopropylacrylamide) (PNIPAm), with different LCST thresholds, may be employed as substrates for thermoresponsive transient systems.<sup>73,74</sup> In conjunction with these stimulus-responsive polymeric binders, we employ high aspect ratio silver nanowires (AgNWs) to form a percolating

conductive network. The predominant advantages of using AgNWs as conductive material are due to their excellent electrical conductivity, biocompatibility and high anisotropy, minimizing the effects of polymer swelling on bulk conductivity.<sup>75-77</sup> The AgNW suspensions exhibit excellent compatibility with existing micropatterning techniques. The AgNW/polymer composite exhibits stable electrical performance when immersed in a warm water bath ( $T_{\text{water}} > \text{LCST}$ ), but disintegrates within 5 second when a cooling thermal stimulus triggers the transient behavior (Figure 2.1a-c). After characterizing the thermoresponsive electrical conductance of these composites, we demonstrate the ability to pattern (both macroscopically and microscopically) conductive AgNW traces in thermoresponsive insulating substrates and form various transient passive components. A transient platform, composed of various passive components on a thermoresponsive transient substrate is built to demonstrate the versatility of this system.

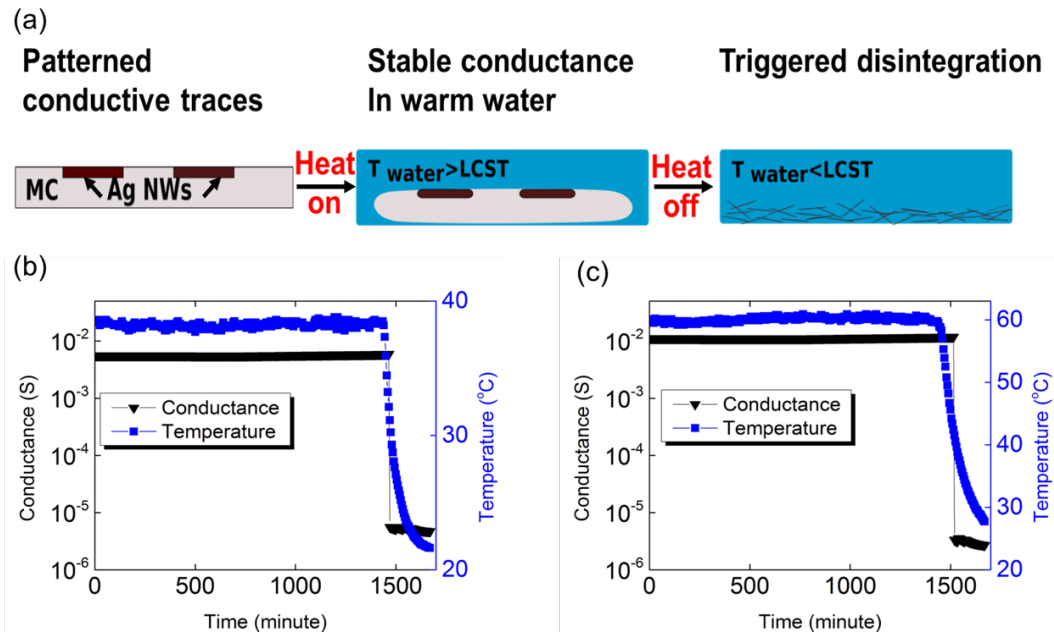


**Figure 2. 1** (a)Thermoresponsive transient system with AgNWs embedded in a LCST polymer film. The conductive AgNW network disintegrates when the water bath temperature cools below the LCST and the polymer binder dissolves. (b) Stability of a AgNW/PNIPAm composite over 24 h and dramatic disintegration upon water bath cooling below LCST ( $\sim 32^{\circ}\text{C}$ ). (c) Stability of a AgNW/MC composite over 24 h and dramatic disintegration upon water bath cooling below LCST ( $\sim 45^{\circ}\text{C}$ ).

## 2.2 Methods and Materials

To characterize the percolation threshold of AgNW/polymer composites, PNIPAm (Sigma-Aldrich, Mn 20,000-40,000) was dissolved in isopropanol (5% w/v) and mixed with AgNW suspensions at various mass ratios; this solution was then cast onto interdigitated gold electrodes. To form patterned conductors, we first deposited parylene C onto a clean Si substrate (PDS, Specialty Coating System) to form  $\sim 3 \mu\text{m}$  thick film (3 grams of parylene dimer used). Standard photolithography was used to pattern photoresist (S1813, 1000 rpm for 1 minute) on top of the parylene to serve as an etch mask. Oxygen plasma etching (Oxford RIE PlasmaPro 100 Cobra, descum for 250s) was used to remove exposed parylene. AgNW (ACS Material, AgNWs-300 and AgNWs-L50) suspension was cast on the wafer and left exposed in a fume hood for 1 hour to allow the isopropanol solvent to evaporate. Patterned AgNW traces were obtained via carefully peeling off the parylene mask (Figure 2.2). Methyl cellulose (Sigma-Aldrich 15cp, 400cp, 4000cp) dissolved in trifluoroethanol (Fisher, 2,2,2-Trifluoroethanol) was spun coated onto the patterned AgNWs at 100 rpm. After drying overnight, the MC film (with embedded AgNWs) was gently peeled off the silicon wafer. To fabricate a parallel plate capacitor, MC solution was spun coated on patterned AgNW traces at 100 rpm, and then another dry piece of AgNW/MC film (with AgNWs facing upward) was immediately placed on the still-wet MC film with the alignment as desired. Afterward, the whole substrate was placed in a fume hood overnight. In this way, the top and bottom surface of the MC film may contain parallel conductive AgNW traces to work as electrodes.

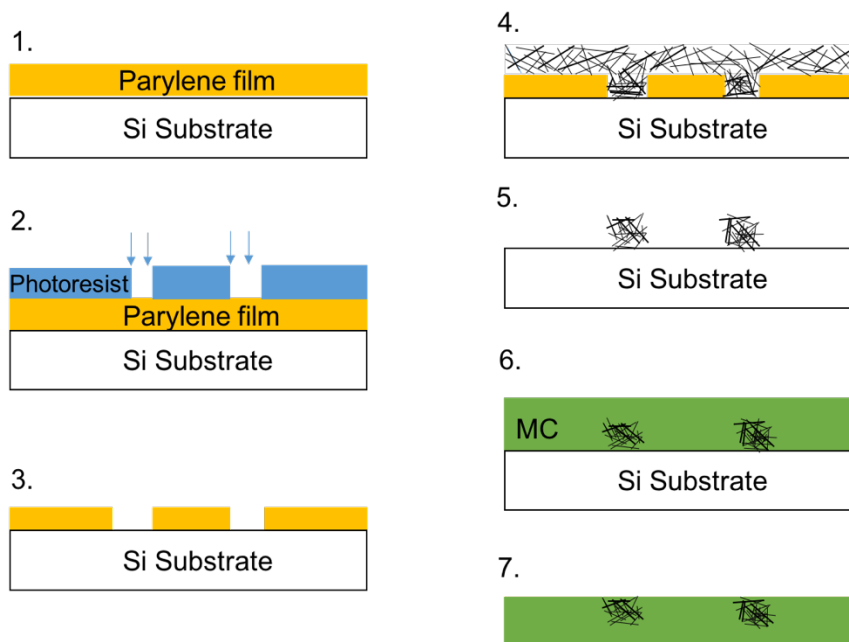


**Figure 2. 2** Schematic illustration of the fabrication process used to pattern AgNW networks. 1. Deposit parylene onto Si wafer. 2. Use photolithography to pattern desired shape in resist. 3. Remove exposed parylene film using oxygen plasma. 4. Cast AgNW suspension on the whole wafer surface. 5. Peel the parylene off and leave patterned AgNWs on the surface. 6. Spin coat methyl cellulose solution. 7. Gently peel methyl cellulose film from Si substrate.

Computer controlled hot plates (IKA/RET control-visc) were used to heat the water baths in which transient devices were immersed. A LabVIEW program was used to acquire data from electrical characterization hardware (sourcemeater or LCR meter) and water bath temperature measurements from the hotplates (using the hotplate’s external temperature probe), and to turn off the hotplate heat source at a specific time. A Keithley 2450 Sourcemeater was used to measure the electrical conductance of the AgNWs/polymer composite in both dry and wet states. Capacitance was measured using a computer-controlled LCR meter (Keithley U1731C) connected to the device using gold coated Kevin Clips (Allied Electronics).



## 2.3 Results and Discussion

To characterize the transient behavior, we cast various formulations of AgNWs and LCST polymer onto interdigitated gold electrodes<sup>78,79</sup> and monitored the electrical conductance. When immersed in a warm water bath ( $T_{\text{water}} > \text{LCST}$ ), the polymeric binder is hydrophobic and thus enables stable electrical conductance with negligible change over 24 hours. When the water bath is allowed to cool and the temperature drops below the LCST, the polymeric binder becomes hydrophilic and dissolves, releasing the embedded AgNWs into solution, irreversibly destroying the circuit and rendering it untraceable. Unless otherwise indicated, deionized water (DI water) with electrical resistivity of 18 M $\Omega$ ·cm (produced using a Milli-Q Integral ultrapure water) has been used as solvent in this study. The timeframe for disintegration in previous transient systems that rely on slow and steady dissolution of their components is on the order of hours or days,<sup>80</sup> and similar timeframes were observed with photosensitive transient systems.<sup>42</sup> Using our AgNW/LCST polymer platform, we obtain extremely rapid (within 5 second) loss of function upon cooling. To tune the threshold temperatures of our thermoresponsive transient systems, we can choose polymers with different LCSTs. For example, PNIPAm and MC have a LCST around 32°C and 45°C, respectively; these polymers have been widely used as temperature-sensitive scaffolds for tissue engineering and drug delivery.<sup>81,82</sup> The temperature-dependent electrical behavior of devices formed from MC with three different molecular weights (14,000, 41,000, 88,000), as well as a device formed from MC with molecular weight of 41,000 but 10x thicker than the others, was compared. We did not observe any obvious relationship between disintegration temperature and either film thickness or molecular weight (Figure 2.3). It is known that the LCST of MC changes only slightly (a few degrees C) with varying molecular weight.<sup>83,84</sup> This small variation in LCST may affect the temperature at which the MC film begins to

disintegrate to a small extent, but this was not observable in this study with any significance due to the rate of cooling of the water bath in relation to the disintegration rate. Moreover, it is known that the rate of thermogelation is only marginally dependent on molecular weight,<sup>85</sup> and swollen films formed from different molecular weight MC may, upon cooling, disintegrate at different rates. However, the dependence on molecular weight of these behaviors were not so dramatic as to be observable in this study. Since the 3- $\mu\text{m}$  thick AgNW networks are attached only on the surface of MC (i.e. the nanowires are not distributed throughout the entire device thickness), the conductance loss due to the dissolution of the MC film is not related to the thickness of the polymer substrate.

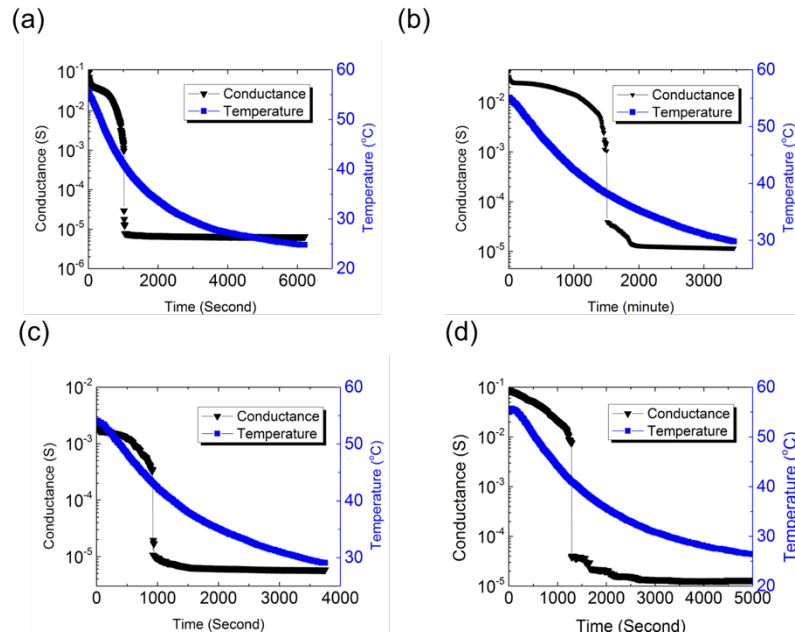


**Figure 2. 3** Electrical conductance of an immersed transient circuit (50mm in length and 4 mm in width), and water bath temperature after the bath heater is turned off. Measurements were taken every 5 seconds. Transient behavior of methyl cellulose film (0.08 mm in thickness, containing an embedded AgNW network) with molecular weight of 88,000(a), 41,000(b) and 14,000(c). (d) shows the transient behavior of 0.7 mm thick MC film with the same molecular weight as (b) but almost 10x thicker.

Figure 2.4a shows a SEM image of AgNWs embedded in a MC film. When pouring the MC solution on the AgNW pattern, the liquid infiltrates into the AgNW network but maintains the pattern of the conductive AgNW network. After drying overnight, the resulting transparent polymer film with AgNWs buried below the polymer surface can be peeled off the Si substrate. The conductivity of the resulting AgNW traces is  $6250 \text{ S cm}^{-1}$  (sheet resistance of  $\sim 0.4 \text{ } \Omega/\text{sq}$ ), and is similar to values reported in previous studies using AgNWs as conductors ( $5825\text{-}8130 \text{ S cm}^{-1}$ , for use in stretchable electronics, strain sensors and soft robotics),<sup>66,86–88</sup> and higher than values reported in previous transient electronics studies using pasted of polymer and conductive tungsten microparticles ( $\sim 400 \text{ S cm}^{-1}$ ).<sup>15</sup> This value is also higher than the conductivity of commercial silver epoxy ( $\sim 140 \text{ S cm}^{-1}$  or resistivity of  $0.007 \text{ } \Omega/\text{sq}$ ).<sup>89</sup> Negligible resistance change was observed after repeated bending of  $180^\circ$  by hand, as the AgNW network holds its shape while embedded within the MC matrix (Figure 2.5). This behavior is similar to that observed with AgNW networks used as conductors for stretchable electronics applications.<sup>75</sup>

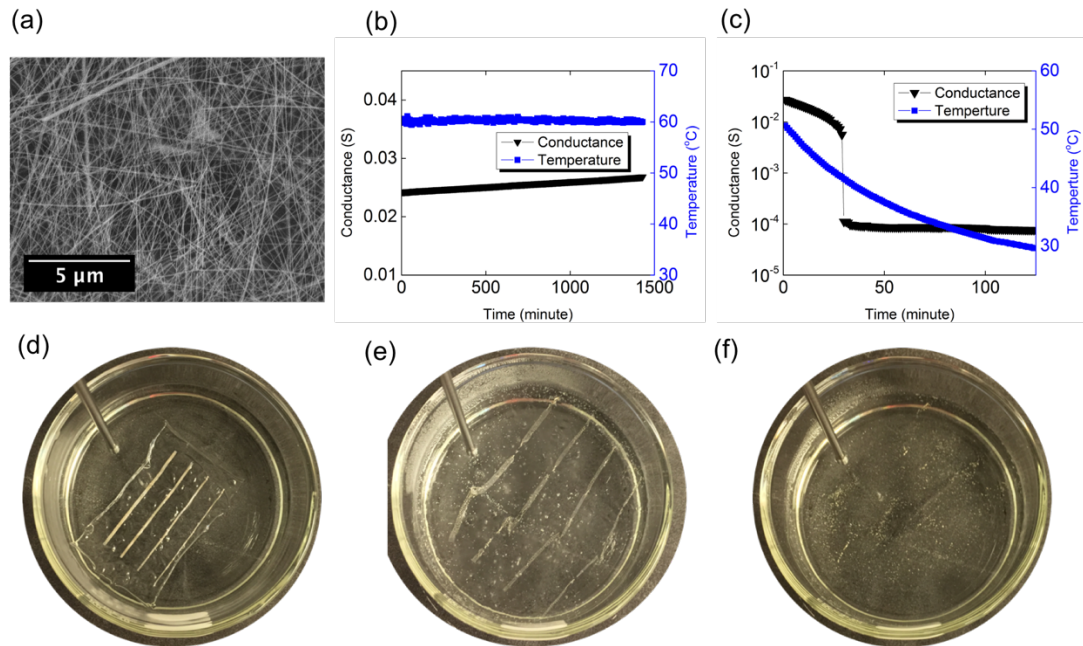


**Figure 2. 4** (a) SEM image of AgNW network embedded within a MC film. (b) Stability of the

electrical conductance of the AgNW network embedded in MC over 24 h immersed in a warm water bath (change of 9.7%). (c) Dramatic loss of conductivity when the water bath cools below the LCST. (d-f) Optical images of the AgNW/MC film morphology change in a water bath at 60, 38 and 22 °C.

The electrical conductance of the transient system depends on the density of the AgNWs embedded in dielectric polymeric matrix.<sup>90</sup> We compared the electrical percolation threshold of two different varieties of AgNW (aspect ratios (L/D) of 100 and 2000~4000) to determine the optimal mass ratio of AgNWs/polymer for each size of AgNW in our conductive composite system. We spun coated thin films of various AgNW/PNIPAm formulations onto interdigitated gold electrodes to measure their conductance in both dry and wet states. The measured resistance was then converted into the film conductivity based on the geometry of the interdigitated gold electrodes using the following equation:

$$\sigma_f = \frac{1}{R_f} * \frac{d}{l(N-1)t}$$

where  $d$  is the gap between the interdigitated electrodes,  $t$  is the thickness of the film,  $l$  is the length of the individual electrode and  $N$  is the number of teeth.<sup>78,91</sup> Figure 2.6 shows conductivity as a function of AgNW/polymer mass ratio and the result agrees, to within an order of magnitude, with the 3D theoretical electrical percolation prediction for isotropically oriented conductive cylinders with high aspect ratios for  $L/D > 100$ .<sup>92,93</sup> The 3D percolation theory assumes isotropically oriented nanowires in 3D space, whereas the 2D percolation theory model would be appropriate for nanowires oriented entirely within a plane (i.e. no out-of-plane orientation components). In our work, the AgNW/polymer composite was deposited onto the interdigitated gold electrodes via spin coating, and thus the radial liquid flow during coating likely yields a preferred orientation in the plane (i.e. a somewhat anisotropic distribution of AgNW orientation).

As a result, the threshold observed in our experimental results lies, as expected, between the bounds set by the 3D model and 2D model.

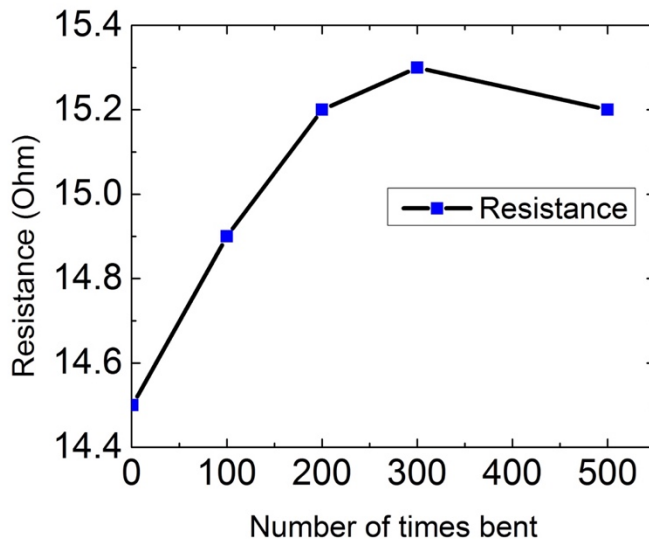


**Figure 2. 5** The electrical resistance of a AgNW/MC film after being deformed 180° by hand versus number of times bent.

To test the transient performance of this platform, a MC substrate containing patterned AgNW networks with dimension of 50 mm in length, 4 mm in width and 0.08 mm in thickness was submersed in a warm water bath and the electrical conductance was measured using gold-coated kelvin clips applied to the two ends of the AgNW/MC trace. Figure 2.4b shows the change in conductance of the AgNW/MC film over a 24-hour period. After the heat source was turned off, the conductance was stable until  $T_{\text{water}} < LCST$ , where a significant loss of conductance can be seen over a 5-minute period (the sampling period of the measurement) (Figure 2.4c). Faster transient behavior as short as 5-second was seen in Figure 2.3. It is worth noting that, once the device is immersed in the water bath, it cannot be retrieved and dried as it has become too fragile. This transient behavior was reproducibly observed on multiple

AgNW/MC samples. Optical images corresponding to the morphology change of the AgNW/MC film at different temperatures are provided in Figures 2.4d-f. Figure 2.4d shows the AgNW/MC layer immersed in warm water bath (60°C). It can be seen that water swelled the MC film but the embedded AgNW network was mechanically stable and electrical performance was not lost. When the temperature of water bath dropped below the LCST, the MC substrate became soluble in water, removing the mechanical support for the AgNW network and thus causing the destruction of the conductive network. Figure 2.4f shows the disintegration of the AgNW/MC film when the water bath temperature had cooled to room temperature (22 °C).

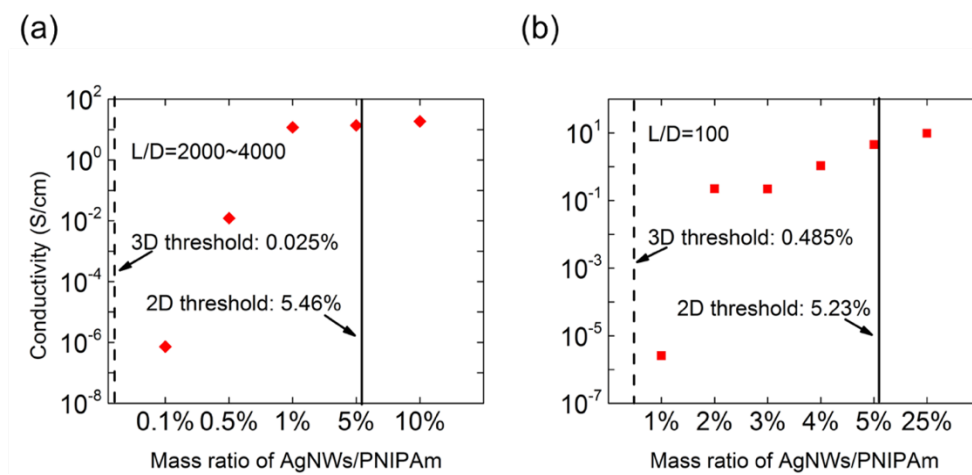


**Figure 2. 6** Conductivity of varying mass ratio AgNWs/PNIPAm with AgNW aspect ratio  $L/D$  2000~4000 (a) and 100 (b). Dotted line represents the 3D theoretical electrical percolation threshold for isotropically oriented cylinders with identical aspect ratios. Solid line represents the 2D theoretical electrical percolation threshold for isotropically oriented rectangles.

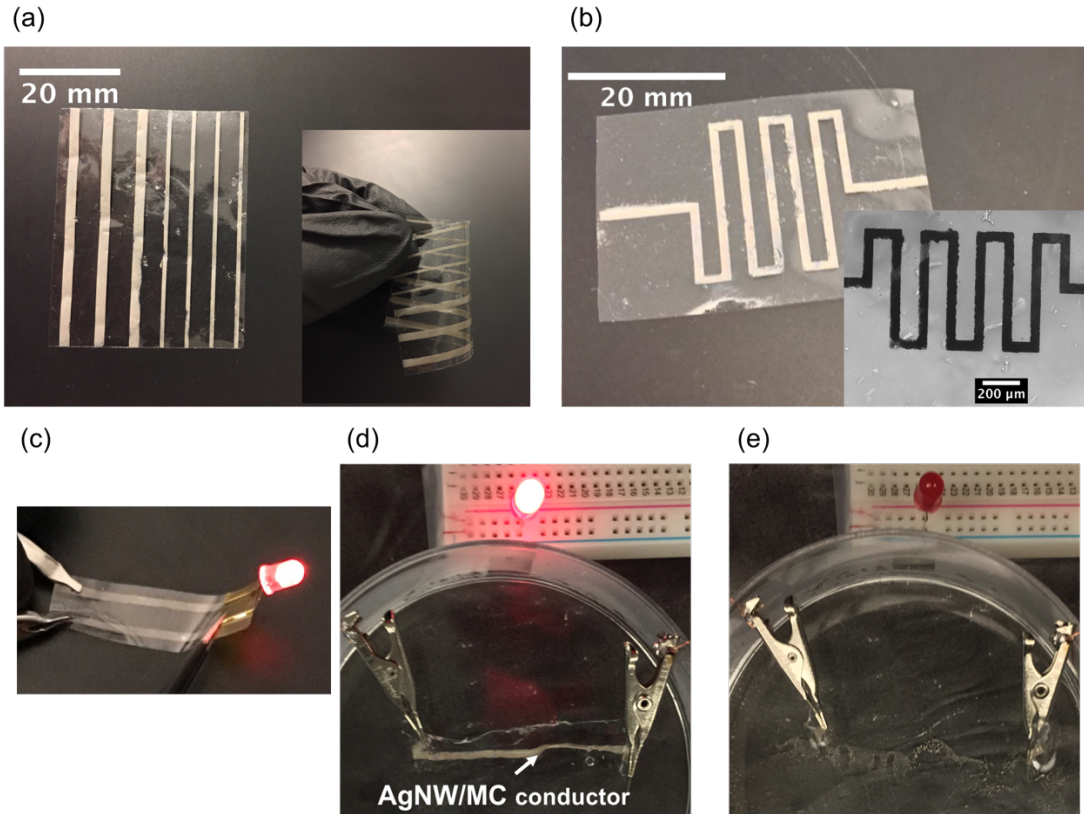


**Figure 2. 7** (a) Patterned parallel AgNW/MC conductive traces with linewidth of 2 mm and 500  $\mu\text{m}$ . The inset shows the conductors deformed by hand. (b) Patterned zigzag traces of AgNWs/MC. The inset shows zigzag patterns with linewidth of 50  $\mu\text{m}$ . (c) Optical image of the deformed LED circuit. (d) Optical image of the LED circuit connected with AgNW/MC conductor submerged in hot water. (e) Optical image of the LED circuit connected with AgNW/MC conductor submerged in cold water.

Figure 2.7a shows a patterned AgNW/MC thermoresponsive transient conductor with linewidths of 2mm and 500  $\mu\text{m}$ . The inset image shows the deformed film in hand, illustrating that this is a flexible electronics system not unlike previous flexible electronics employing AgNWs patterned on elastomers.<sup>75,94,95</sup> Zigzag patterns were also fabricated (Figure 2.7b). Using a parylene mask, we were able to fabricate microscopic zigzag patterns with linewidth as small as 50  $\mu\text{m}$  (Figure 2.7b inset). In Figure 2.7c, we employed parallel AgNW/MC traces to construct a simple circuit to light a light-emitting diode (LED). We also powered a surface-

mount device (SMD) LED with a AgNW/MC trace with linewidth of 1 mm. With transient conductive AgNW/MC traces, we then built a temperature-sensitive LED circuit, composed of a red LED connected in series with a piece of AgNW/MC trace (Figure 2.7d). The red LED remained continuously lit for 12 hours while the AgNW/MC conductor was submerged in a warm water bath ( $T_{\text{water}} > \text{LCST}$ ). After the heat was turned off, the red LED turned off when the colder solution temperature triggered the dissolution of MC film, leading to the destruction of the AgNW/MC circuit (Figure 2.7e). We note that LCST polymer-based substrates may have the potential to integrate with other materials, such as Mg, Zn and Si NMs, to enable additional varieties of thermoresponsive transient electronics.

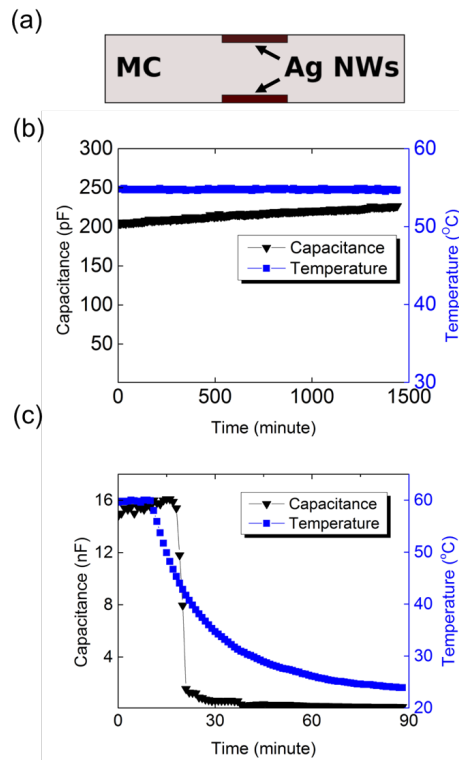


**Figure 2. 8** (a) Schematic showing the parallel-plate capacitor formed from AgNWs and MC. (b) Stability of capacitance over 24 h in warm water bath (change of ~10%). (c) Dramatic change in capacitance as water bath temperature drops below the LCST.



To demonstrate the ability to form multilayer devices, we fabricated a thermoresponsive parallel-plate capacitor (Figure 2.8a). The device was composed of a MC slab with two patterned AgNW traces, embedded in the top and bottom surfaces, as two conductive electrodes (Figure 2.9). The thickness of the AgNW layer on each side was  $\sim 4 \mu\text{m}$ , with a  $\sim 110 \mu\text{m}$  MC film in the middle.

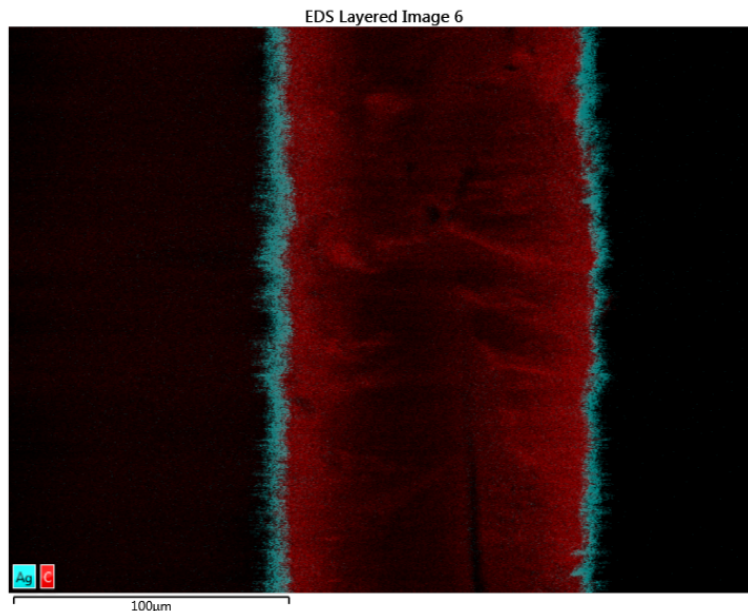


**Figure 2. 9** Energy dispersive spectroscopy (EDS) image of parallel plate capacitor built by attaching two slabs of AgNW/MC film together. Blue indicates Ag and red indicates C.

To achieve the desired alignment of two AgNW/MC films, we spin coated fresh MC solution onto patterned AgNW traces, 2 mm in width, on a silicon wafer and immediately put another prefabricated dry AgNW/MC film down (with AgNWs facing upwards) on top of this fresh coating. Careful adjustment of the position of the top AgNW/MC film using tweezers allowed us to achieve the desired alignment needed to form a parallel plate capacitor. When the device was immersed in a warm water bath, we measured a stable capacitance for 24 hours

(Figure 2.8b). As before, the destruction of the capacitor was triggered when the water bath temperature decreased below the LCST. The capacitance change was rapid and occurred within 5 minutes (Figure 2.8c). In the dry state, the capacitance was in good agreement with the theoretical prediction, given by  $C = \epsilon_0 \epsilon_r \frac{A}{d}$ , where  $\epsilon_0$  is electric constant,  $\epsilon_r$  ( $\sim 20$ ) is the dielectric constant of dry MC film,<sup>96</sup>  $A$  and  $d$  are overlap area and gap between the two electrodes, respectively. To address the concerns of thermally-induced capacitance changes, we placed the dry capacitor on a hot plate for a long time period and monitored its electrical behavior; the result indicated that the capacitor performance was not compromised simply by elevated temperature (Figure 2.10).

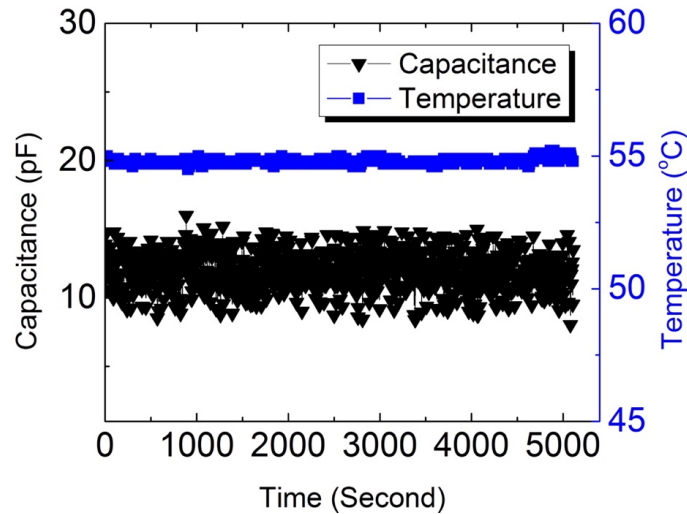


**Figure 2. 10** Capacitance change over time when the dry capacitor was placed on a hot plate.

## 2.4 Conclusion

We have demonstrated that LCST polymers, such as PNIPAm and MC, are promising thermoresponsive materials for transient electronics applications. AgNW/MC conductive traces were fabricated by embedding AgNWs below the surface of MC film. Stable electrical

conductivity in solution was observed for over 24 hours, and a cooling stimulus induced rapid disintegration. The loss of electrical conductance is due to the conductive AgNW network being released from the polymeric binders, causing irreversible destruction of the circuit. Using a parylene patterning technique, we formed straight and zigzag patterns of AgNWs at macroscopic and microscopic scales. Finally, a temperature-responsive LED circuit and a capacitor were built using the AgNW/MC conductors. With stable electrical performance in a warm water environment, thermally-induced disintegration (e.g. heat is required for the circuit to remain viable) and compatibility with standard fabrication techniques, the reported thermoresponsive transient conductive composites open up new possibilities for exciting applications employing stimulus-responsive transient electronic devices.

## Chapter 3 Thermoresponsive Transient Radio Frequency Circuits

### 3.1 Introduction

The development of bioresorbable circuitry has facilitated the advancement of temporary biomedical implants, providing new behaviors such as the capability to disintegrate in the body and thereby avoid complications associated with surgical extraction. While previous efforts have demonstrated a variety of biodegradable circuitry,<sup>97–100</sup> there is still a need to develop next-generation implantable systems that may respond in new, more unique ways, including the capability of disintegrating in response to a specific stimulus.

The recent emergence of transient electronics that are designed to disintegrate and disappear after they are no longer needed represents a promising route to advance temporary biomedical implants. The expansion of available transient modes, materials and devices enables the development of novel transient circuitry platforms, many of which have demonstrated potential utility in facilitating monitoring or treatment of various disorders. For example, implantable transient platforms consisting of biodegradable metals, semiconductors, and polymeric substrates have been developed to accomplish several tasks such as noninvasive sensing, real-time diagnosis and point-of-care therapy.<sup>59,101–103</sup> Moreover, such biocompatible transient systems can be safely resorbed in the body after preprogrammed time frames, avoiding potential infection and inflammation due to long-term implantation or surgical removal. Additional applications of transient electronics include secure data storage that can protect confidential information from unauthorized access and environmentally-friendly electronics that generate non-hazardous byproducts after disposal.<sup>68,104–106</sup>

Not surprisingly, the implementation of various transient electronic systems imposes a set of

stringent requirements on materials selection, hardware architectures and manufacturing techniques. To date, significant research effort in the field of transient circuitry has been devoted to the development of bioresorbable and biodegradable circuits that can play a critical role in advancing healthcare applications. Such examples include fully bioresorbable electronic sensors for continuous monitoring intracranial pressure and temperature<sup>103</sup>, transient neurophysiologic monitoring systems<sup>102</sup>, and wireless transient devices for neuroregeneration and recovery.<sup>101</sup> Several recent reviews thoroughly summarize different classes of materials (e.g. conductors, insulators, semiconductors and encapsulation/substrate materials) that have been utilized in bioresorbable transient electronic systems.<sup>98,107,108</sup> Despite these initial successful results, the majority of existing transient systems are primarily dependent on uncontrolled materials degradation and dissolution in aqueous environment, the drawback of which is the absence of on-demand transience. As such, there are opportunities to look beyond hydrolysis-enabled transient platforms, and to exploit alternative materials (e.g. stimuli-responsive or “smart materials”) and device architectures that can enable triggered transience.

One route to enable on-demand transience is to utilize materials that can exhibit profound changes in behavior upon external triggers. By leveraging such unique behavior, several externally-triggered transience modalities have been demonstrated. For example, Gao et al. reported moisture-triggered transient electronics that can physically disappear within controlled time frames. This transient system was based on the fact that the moisture-triggered hydrolysis of the polyanhydride substrate employed generated corrosive organic acids, which subsequently destroyed electronic components and substrates.<sup>109</sup> Our previous work illustrated a thermoresponsive transient mode by leveraging composites of thermoresponsive polymers and conductive silver nanowires (AgNWs). Such conductive composites can provide constant

conductance when immersed in warm water, but rapidly disintegrate upon a cooling trigger.<sup>110</sup> Additionally, Pandey et al. reported two techniques, nanothermite thin film coating and release of corrosive acidic agents, to enable triggered self-destructing transient electronics. Both methods were shown to destroy typical silicon microchips within 13s of trigger activation.<sup>104</sup> In addition to the development of such stimuli-responsive compounds, other transient systems have been enabled by employing novel manufacturing approaches. For instance, Chang et al. developed 3D, heterogeneously integrated transient electronic systems by transfer printing multilayer interconnected components onto poly(lactic-co-glycolic acid) (PLGA) substrates.<sup>97</sup> Furthermore, Yoon et al. employed 3D printing to fabricate transient substrates composed of water-soluble poly (vinyl alcohol) (PVA), the dissolution of which can be precisely controlled by altering the density of the printed PVA.<sup>111</sup>

We introduce materials, device architecture and processing techniques for construction of a wireless transient radio frequency (RF) antenna that can maintain physical stability and electrical functionality in a warm phosphate-buffered saline (PBS) bath but disintegrates and disappears when the solution cools down. Unlike the vast majority of popular silk-based transient systems, where water acts both as solvent to dissolve silk substrates and as reactant to induce the hydrolysis of construction materials (i.e. magnesium and silicon nanomembrane), our transient systems are designed to provide stable performance in warm aqueous environment (i.e. water or biofluids) and on-demand transience behavior can be rapidly activated by applying an external cooling stimulus. To fabricate solution-temperature triggered transient systems, we develop a collection of relevant techniques including materials processing methods, device architectures, and encapsulation approaches. The implementation of a cooling triggered transient RF antenna illustrates the potential of such thermoresponsive polymeric materials to act as building blocks

for next-generation retrieval-free implantable devices, the lifespan of which can be controlled by an external cooling trigger.

Methyl cellulose (MC), a polymer that exhibits lower critical solution temperature (LCST), is systematically investigated to determine its ability to function as a substrate for thermoresponsive transient systems. Methyl cellulose is hydrophilic in cold water ( $T_{\text{water}} < \text{LCST}$ ) yet is hydrophobic in warm water ( $T_{\text{water}} > \text{LCST}$ ), which is due to the interplay between contribution from enthalpy (arising from the hydrogen bonding between water molecules and polar groups on the polymer), leading to dissolution of the polymer and contribution from unfavorable entropy of mixing (arising from hydrophobic groups on the polymer), leading to the precipitation of the polymer.<sup>112</sup> We employ a well-established parylene stencil approach to pattern networks of conductive metal nanowires,<sup>113</sup> which act as functional electrical circuits above the LCST but disintegrate upon the dissolution of substrate. In order to enable on-demand transience upon a cooling stimulus, we develop a 3D multilayer integration strategy by sandwiching patterned AgNW circuitry between two layers of MC substrates as illustrated in Figure 1. Such device architecture is of considerable importance to achieve rapid thermoresponsive transient behavior upon an external cooling trigger as the dissolution of MC substrates below LCST eliminates mechanical support of the embedded functional circuitry, thereby causing rapid disintegration of the percolating AgNW network. In order to integrate multiple MC substrates, we developed a simple water-welding approach to accomplish robust adhesion between MC substrates. When exposed to water mist from a spray brush, the top surface of a MC film becomes tacky and hence will adhere to a target surface. In addition, this bonding method does not involve the use of complex cleanroom facilities or any organic solvents.

While silk has gained extensive popularity as a device substrate material in various transient

systems, it is noted that the swelling of silk represents a long-standing issue that can result in unwanted delamination prior to achieving the desired performance.<sup>114</sup> Though hydrophobic above LCST, a similar issue occurs when dealing with MC substrates in warm water. To address this issue, we develop a parylene-coating strategy to reduce the contact area between water and the MC substrate. Using this approach, MC-based transient systems are able to function stably when completely immersed in warm water, but sudden loss of functionality occurs when the aqueous environment is cooled below a threshold temperature. We note that parylene possesses many advantageous properties, including flexibility, transparency, low water permeability and biocompatibility, all of which make it well-suited to act as the water barrier without affecting encapsulated transient circuitry.<sup>115</sup>

Figure 3.1 provides a schematic representation illustrating the operating principle of the proposed thermoresponsive device fabricated by laminating layers of biocompatible polymeric materials with patterned conductive nanofillers embedded in the middle. When immersed in warm water, the transient system maintains stable and functional behavior over at least seven days. However, when the device is no longer needed, rapid transience can be initiated simply by allowing the water bath to cool, which triggers the dissolution of the encapsulated MC substrates and further leads to disintegration of the embedded nanowire circuits. Hence, the lifespan of such thermoresponsive transient system is very much dependent on the temperature of the surrounding solution.



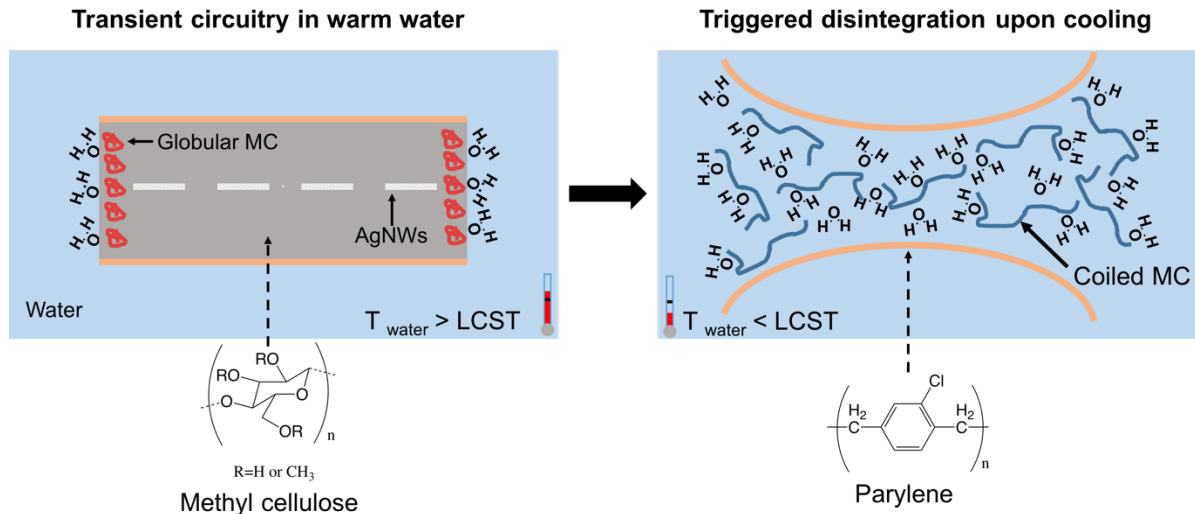


**Figure 3. 1** Schematic of thermoresponsive transient radio frequency antenna consisting of parylene encapsulation layers, bonded MC substrates, and conductive AgNW traces embedded in the middle. When immersed in warm water, the whole circuit is physically and electrically stable (after initial swelling). However, when the solution temperature drops below the polymer LCST, the dissolution of the MC substrates leads to rapid disintegration of the percolating AgNW network.

### 3.2 Methods and Materials

Solution casting was used to prepare methyl cellulose substrates with high transparency. In order to dissolve methyl cellulose powder in water, 40 mL distilled water in a beaker (Milli-Q Integral ultrapure system, 18M $\Omega$ ) was first heated on a hot plate at 60 °C with a magnetic bar stirring at 500 rpm. Then, 1200 mg methyl cellulose powder (Sigma-Aldrich, Mn 20,000-40,000) was slowly added into the warm water until it became well-dispersed. Afterward, the hot plate was turned off to allow the solution to cool down to room temperature, enabling rapid dissolution of the dispersed polymer. Homogeneous and bubble-free MC solution was obtained after degassing in a vacuum oven overnight. A clean 4-inch silicon wafer was used as the casting substrate to fabricate MC films. After overnight drying under a fume hood at ambient conditions (~22 °C), MC films could be peeled off the wafer.

Thermal Gravimetric Analysis (TGA instrument Specialists TGA 1000) was employed to evaluate the remaining water content of as-fabricated MC films. A 3 mg MC film was placed in a platinum sample pan and heated to 200 °C at a rate of 20 °C/min. Mass variation was monitored at the same time and used to obtain initial water content in MC substrates.

To perform tensile stress test, Two rectangular MC films (5 cm in length, 1.5 cm in width and 40 μm in thickness) were prepared. Water mist generated by a spray brush (Badger 200NH) was applied to both MC surfaces to be laminated. Films were then manually aligned and rapidly transferred onto a preheated hot plate (100 °C) to heat for 10 minutes. The overlapping area between MC substrates was 1.5 cm<sup>2</sup>. Tensile tests (Instron 5944), as schematically illustrated in Figure 3.3a, were performed on samples with/without heat-aided welding. The bonding strength of samples processed under different conditions was directly extracted using Bluehill software.

As schematically illustrated in Figure 3.5a, 4g parylene-C pellets (Specialty Coating Systems) were used to deposit films onto 3 pieces of 4-inch silicon wafers (i). Then, a 200 nm thick aluminum (Al) film was thermally evaporated on top of the deposited parylene substrates at deposition rate of 40 Å/s (Angstrom Resistive Evaporator). 1-μm thick S1813 resist was coated above the Al layer and photolithographically patterned using a mask aligner (Karl Suss MA6) (ii). After development, patterns were further transferred into the Al layer by etching exposed Al away using Al etchant (Transene, type A) (iii). Next, any remaining photoresist was stripped off using acetone. The patterned Al layer served as an etch mask to enable the removal of the exposed parylene layer by oxygen plasma reactive ion etching for 480 s (Trion Phantom RIE ICP). The operating RIE power was 150 W and O<sub>2</sub> flow rate was 50 sccm. After parylene etching, the remaining Al layer was removed using Al etchant. This process ended up leaving a patterned parylene stencil on top of the silicon wafer (iv). AgNWs in ethanol were purchased

from ACS Materials (AgNWs-L50). Prior to casting AgNWs, the 4% (w/v) AgNW suspension was sonicated for 30 min to prevent aggregation. Then, 4% (w/v) AgNW suspension was cast over the fabricated parylene stencil using a pipette and dried under fume hood (v). After carefully peeling the parylene stencil off the wafer (vi), a 3% (w/v) MC solution was subsequently cast over the patterned AgNW circuits (vii). After drying overnight, the MC substrate with AgNWs embedded on the top surface was peeled off the silicon wafer.

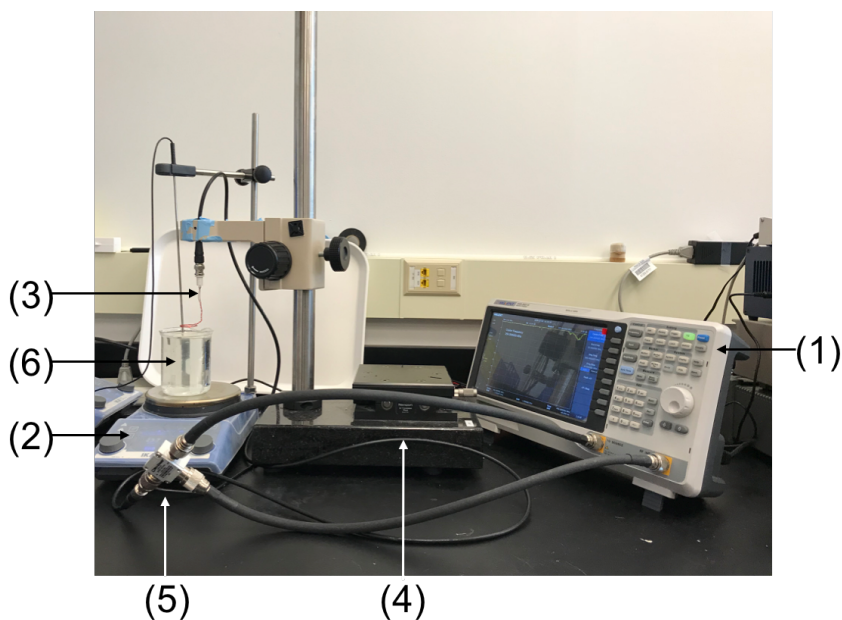


**Figure 3. 2** A photograph showing equipment for measurement of S11 relative to varying solution temperature. (1) - (6) represent the spectrum analyzer, computer-controlled hot plate, two-turn probe, XYZ control stage, directional coupler, and beaker filled with PBS solution respectively.

The experimental setup used to measure return loss (S11) included a spectrum analyzer (Siglent SSA3021X), a directional coupler (Mini Circuits, ZFDC-10-5-N+), and a hand-wound two-turn external probe with diameter of 2.5 cm. A detailed experimental setup is provided in Figure S4. The transient antenna was immersed in a warm water bath that was heated by a

computer-controlled hot plates (IKA/RET control-visc). The probe, connected to the directional coupler and spectrum analyzer, was placed 2 mm above the transient antenna. A LabVIEW program continuously monitored both return loss and resonant frequency, as well as the bath water temperature as reported by the hot plate.

### 3.3 Results and Discussion

The MC substrate was prepared by casting 3% (w/v) MC solution (detailed description in experimental section) on a clean 4-inch silicon wafer. After degassing and drying overnight in a fume hood, the MC substrate (with an average thickness of  $15 \pm 4 \mu\text{m}$ ) was peeled off the wafer. In order to form well-adhered MC structures, it is critical that the surface roughness of fabricated substrates is small. Based on extracted results using an atomic force microscope (AFM, Bruker Dimension Icon), the root mean square (RMS) roughness of fabricated MC substrates is 1.55 nm (Figure 3.4b), suggesting possibilities to be combined with fabrication techniques such as transfer printing.<sup>116</sup>

In order to extend the applicability of MC, we systematically studied a collection of properties of fabricated MC substrates. As shown in Figure 3.4a, the measured optical transmittance (UV spectroscopy, Varian Cary 5000) of MC substrates is 92%, which indicates high transmittance and would be of interest for emerging optogenetic applications where highly transparent substrates are required for efficient light (acting as a stimulus) transmission.<sup>117</sup> The inset photo shows a hand-held MC substrate placed in front of a computer screen, illustrating good transparency. Additionally, it has been suggested that thin polymeric substrates with high flexibility are of particular interest for construction of bioelectronic systems.<sup>38</sup> Figure 3.4c shows a 4-inch MC substrate bending, indicating good flexibility of these MC substrates.

In order to encapsulate patterned AgNW circuitry inside MC substrates, we developed a

strategy that utilizes water mist to act as adhesive agent, followed by heat-aided multilayer welding. Briefly, water mist generated by an air-brush was first applied to the top of a MC film (adhesive substrate). Then, the adhesive MC substrate was manually aligned and attached to the target MC substrate. To create strong interlayer bonding, the device was immediately transferred onto a preheated hot plate to complete heat-aided welding at 100 °C for 10 min. For the fabrication of most organic electronics, polymeric substrates that exhibit high-temperature stability is preferred. Thus, it is advantageous that MC substrates can survive such thermal treatment. Additionally, the glass transition temperature of MC ( $T_g = 184\text{-}197\text{ }^\circ\text{C}$ )<sup>118</sup> is larger than polyethylene terephthalate (PET,  $T_g = 67\text{-}81\text{ }^\circ\text{C}$ ), a widely used plastic substrate in organic electronics.

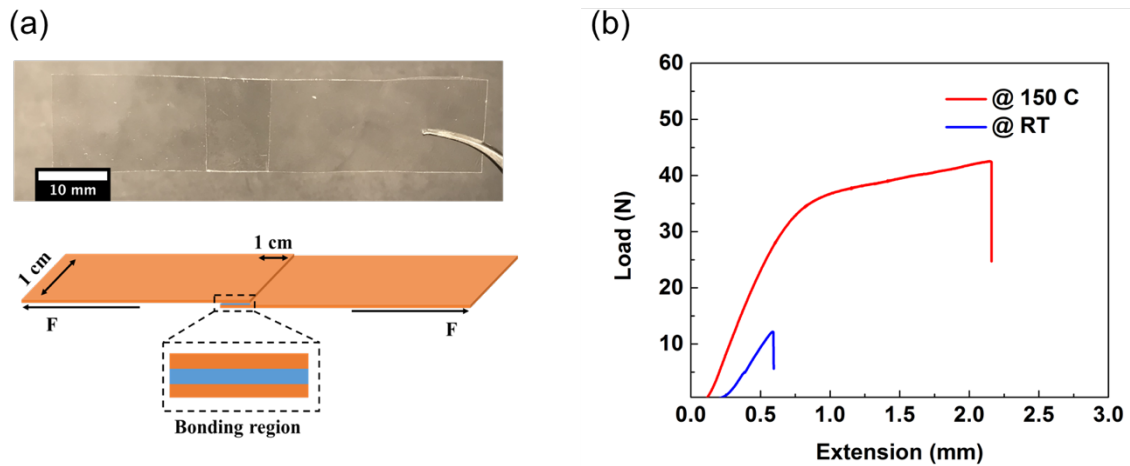


**Figure 3. 3** Tensile testing sample photo (top) and schematic representation (bottom), indicating bonding locations and overlapping areas used in test. (b) Measured results of bonding strength of laminated MC samples with/without thermal treatment. Red curve represents MC sample heated at 100 °C and blue curve represents MC sample annealed at room temperature.

As schematically illustrated in Figure 3.3, the interlayer bonding strength with and without thermal welding treatment was examined by measuring the shear stress acting in parallel to the

bonded interfacial section. Two MC substrates with dimensions of 30 mm in length, 10 mm in width and 40  $\mu\text{m}$  in thickness were bonded together, followed either by heating at 100  $^{\circ}\text{C}$  for 10 minutes or by drying at room temperature (22  $^{\circ}\text{C}$ ). Then, tensile testing was performed to extract the value of corresponding bonding strength. In Figure 3.4d, the bond strength of thermally processed samples ( $\sim 33$  MPa) is three times larger compared to those without heating treatment ( $\sim 11$  MPa). Moreover, results of thermal gravimetric analysis (TGA) revealed that 5% of residual water content of fabricated MC films can be removed during the heating process (Figure 3.4e). The removal of additional water by heating at 100  $^{\circ}\text{C}$  also contributes to enhanced interfacial bond strength. To understand the underlying mechanism, we characterized the cross-section of the bonding interface by scanning electron microscope (SEM). As shown in Figure 3.4f, thermal treatment aids in rapid removal of residual water in the overlapping region, resulting in a good interface with few defects. In contrast, for those samples without thermal treatment (Figure 3.4g), we notice the existence of many gaps/cavities along the bonding interface, which leads to decreased contact area and lower bonding strength.

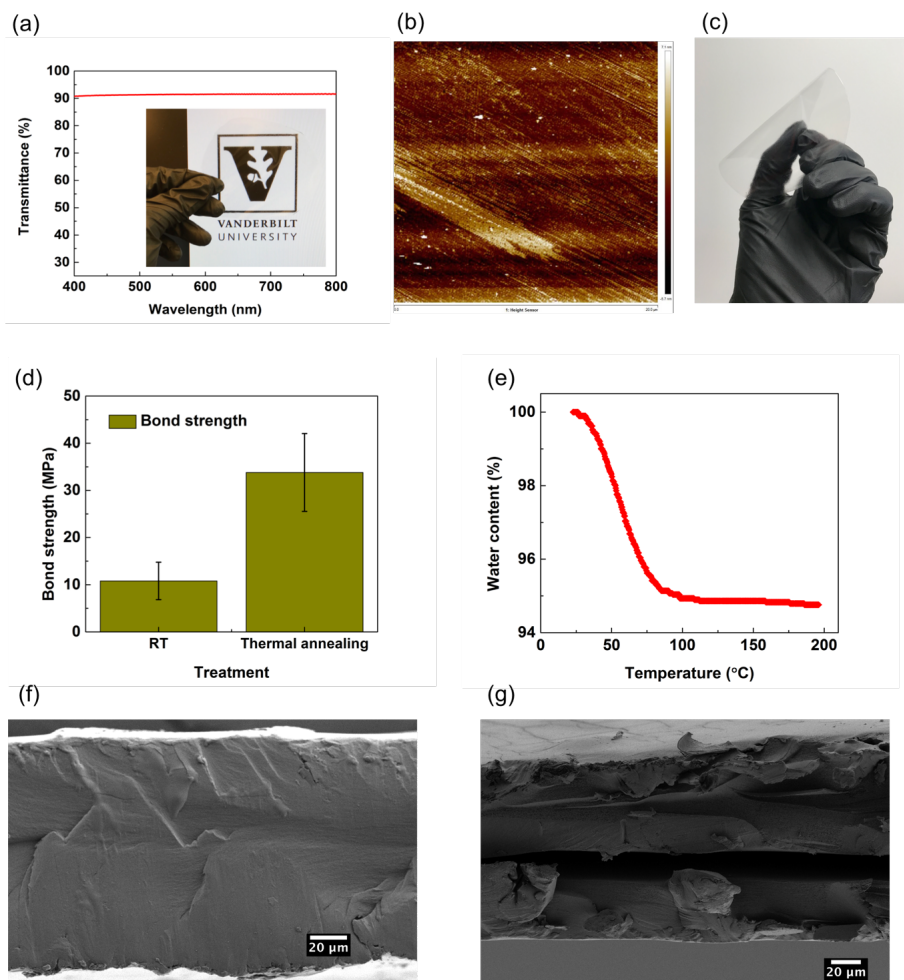


**Figure 3. 4** (a) Measured optical transmission of a 10  $\mu\text{m}$  thick MC film. Inset photo shows a hand-held MC film placed in front of a computer screen, illustrating high optical transparency. (b) AFM surface height profile of fabricated MC substrates. (c) A photo showing a flexible MC film. (d) Measured bond strength of MC samples with and without thermal soldering. (e) Thermal gravimetric analysis of fabricated MC substrates, showing water content variation relative to initial conditions. (f) A SEM image of a cross-section of laminated MC substrates annealed at 100  $^{\circ}\text{C}$ . (g) A SEM image of a cross-section of laminated MC substrates annealed at room temperature.

While conventional hydrolysis-based transient systems primarily utilize deposited metal thin films (e.g. magnesium, tungsten) to form conductors, such continuous conductive films are not suitable for constructing thermoresponsive transient systems, as the hydrolysis of metal traces in aqueous environments ultimately leads to loss of device function regardless of whether on-

demand substrate transience is triggered.<sup>34</sup> Recently, our work has provided an alternative approach by demonstrating conductive thermoresponsive composites where percolating AgNW networks, acting as conductive components, are embedded into the polymeric matrix.<sup>110</sup> Building on our previous work, we now focus on demonstrating thermoresponsive transient antennas that exhibit stable response in warm solution but disintegrate upon a cooling stimulus in an on-demand fashion.

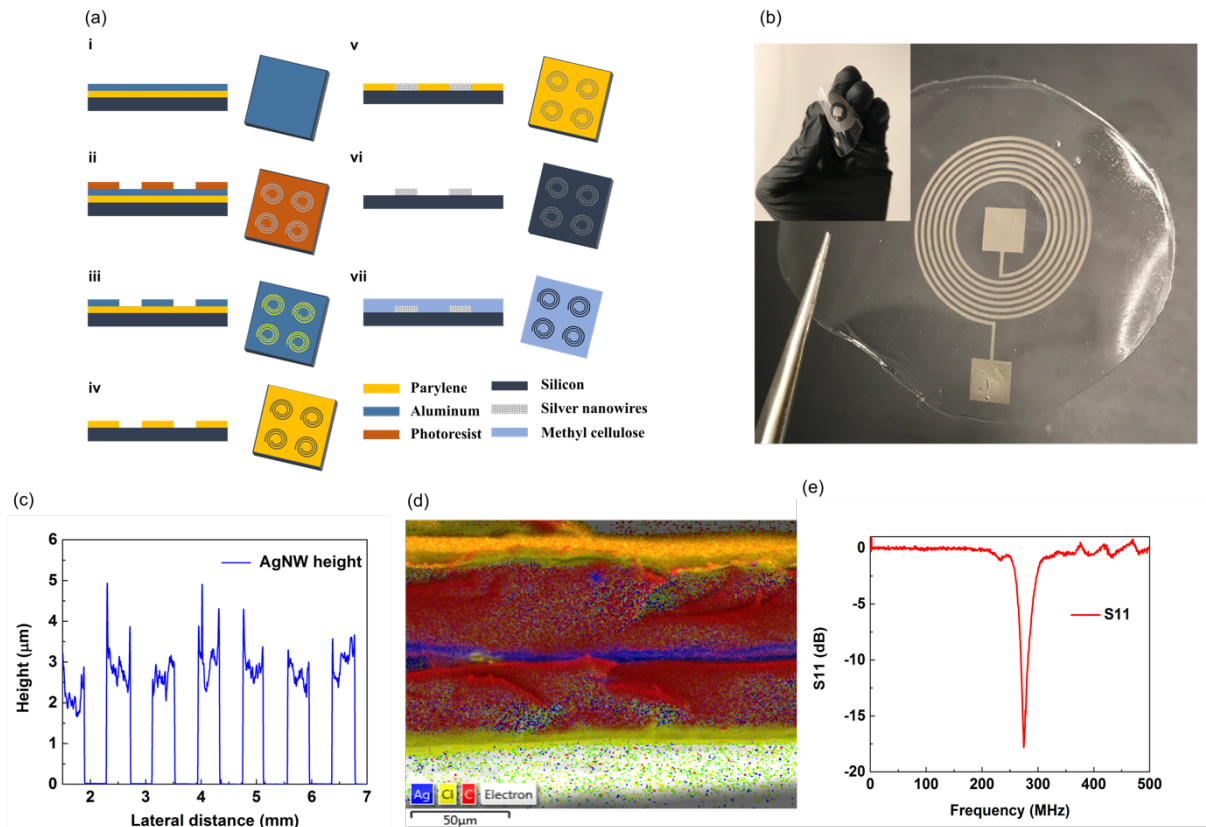


**Figure 3. 5** (a) Schematic illustration of critical steps for parylene stencil fabrication. (b) A photograph showing fabricated transient RF antenna based on AgNWs and MC and the inset image showing a device deformed by hand (c) Measured height profile of patterned AgNW traces on top of a silicon wafer. (d) SEM-EDS elemental analysis of fabricated transient antenna device. Yellow, red and blue represent chloride (parylene), carbon (MC), and silver (AgNWs), respectively. (e) Measured return loss (S11) of transient RF antenna in ambient dry environment.

To construct such thermoresponsive transient wireless systems, we employed a



photolithographically patterned parylene stencil to pattern solution-cast AgNWs.<sup>119,120</sup> The complete fabrication process is schematically depicted in Figure 3.5a. Detailed fabrication steps are provided in the experimental section. Figure 3.6 shows the measured height profile of the parylene stencil as characterized by profilometry (Veeco Dektak 150). Figure 3.5c shows the height profile of patterned AgNW network traces on top of the silicon wafer. The height of the AgNW network traces can be tuned (up to at least tens of microns) by repeatedly casting a AgNW suspension over the parylene mask.

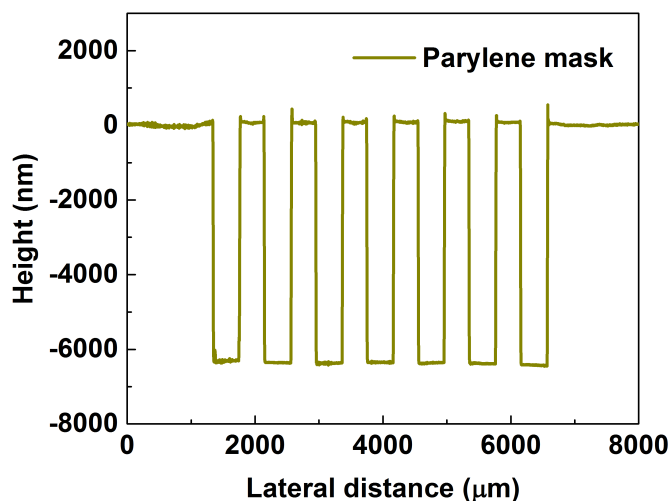


**Figure 3. 6** Measured height profile of fabricated parylene stencil mask used for subsequently patterning nanowires.

In order to reduce undesired MC swelling in warm water, 1- $\mu\text{m}$ -thick parylene film was deposited over the assembled device using Parylene Deposition System (SCS Labcoter, PDS 2010). Afterward, the device was manually trimmed using a surgical blade along the edge to expose the encapsulated MC substrate cross-sections. To characterize the assembled device architecture, we conducted SEM-EDS elemental analysis to visualize the various layers. As

illustrated in Figure 3.5d, two yellow layers (Cl) on the top and bottom represent deposited parylene films. In-between, two red layers (C) represent the bonded MC substrates and the middle blue layer (Ag) represents the patterned AgNWs. Figure 3.7 shows SEM-EDS elemental maps showing the presence of Cl, Ag, and C, respectively. To confirm the reproducibility of this approach, we have conducted testing on multiple samples, none of which exhibits noticeable delamination between bonding interfaces. Thus, we envision this protocol would greatly extend the use of MC substrates for constructing thermally sensitive bioelectronic systems.

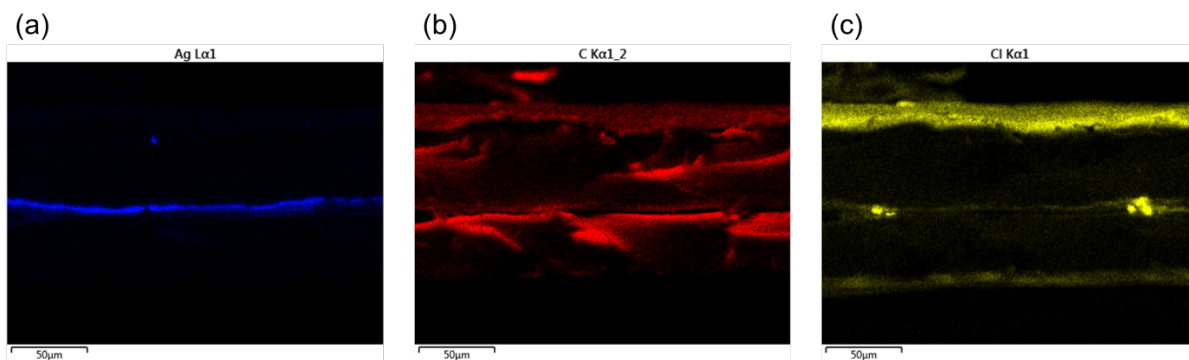


**Figure 3. 7** SEM-EDS elemental mapping showing different constituent materials including AgNWs in blue (a), MC in red (b), and parylene in yellow(c).

Antenna-based passive devices such as RFID tags that can be interrogated wirelessly have found increasing use in many applications, including low-cost item tracking, livestock monitoring, and personal healthcare.<sup>121–123</sup> Moreover, there is a growing tendency to construct wireless sensing systems by coupling biocompatible materials with functional circuits because such systems can be easily adopted for monitoring physiological parameters of interest in a noninvasive manner.<sup>124,125</sup> Here, we provide a proof-of-concept demonstration by fabricating a transient radio frequency (RF) antenna that can be triggered to destruct upon cooling. Figure 3.5b shows a photograph of the fabricated device made of MC and AgNWs. Additionally, the antenna

is mechanically robust and highly flexible (inset image of Figure 3.5b) and thus can be transferred and adhered onto curved surfaces which are frequently found in biomedical sensing applications. Due to the use of percolating networks made of conductive nanowires, the resulting circuitry exhibit marginal variation on electrical conductance over repeated bending test.

The passive MC-based antenna can be modeled as a LC resonator and the resonant frequency ( $f_0$ ) can be calculated by the expression of  $f_0 = 1/2\pi\sqrt{LC}$ , where L is the inductance, C is the capacitance. The resonant behavior is primarily related to factors such as circuit geometry (e.g. line gap, line width and number of turns), dielectric properties of encapsulating and substrate materials, and the surrounding environment.<sup>126</sup> Figure 3.5b shows an image of MC-based antenna consisting of a seven-turn spiral trace with a line width of 400  $\mu\text{m}$  and an overall size of 30\*30  $\text{mm}^2$ . To characterize its resonant behavior, a transmission antenna was used to wirelessly interact with the fabricated transient antenna at a fixed distance of  $\sim 2$  mm. The S11 parameter was evaluated using a spectrum analyzer and a directional coupler. Figure 3.5e depicts the measured S11 of a thermoresponsive transient antenna whose  $f_0$  appears at 274.7 MHz with a magnitude of -18 dB in the dry state.

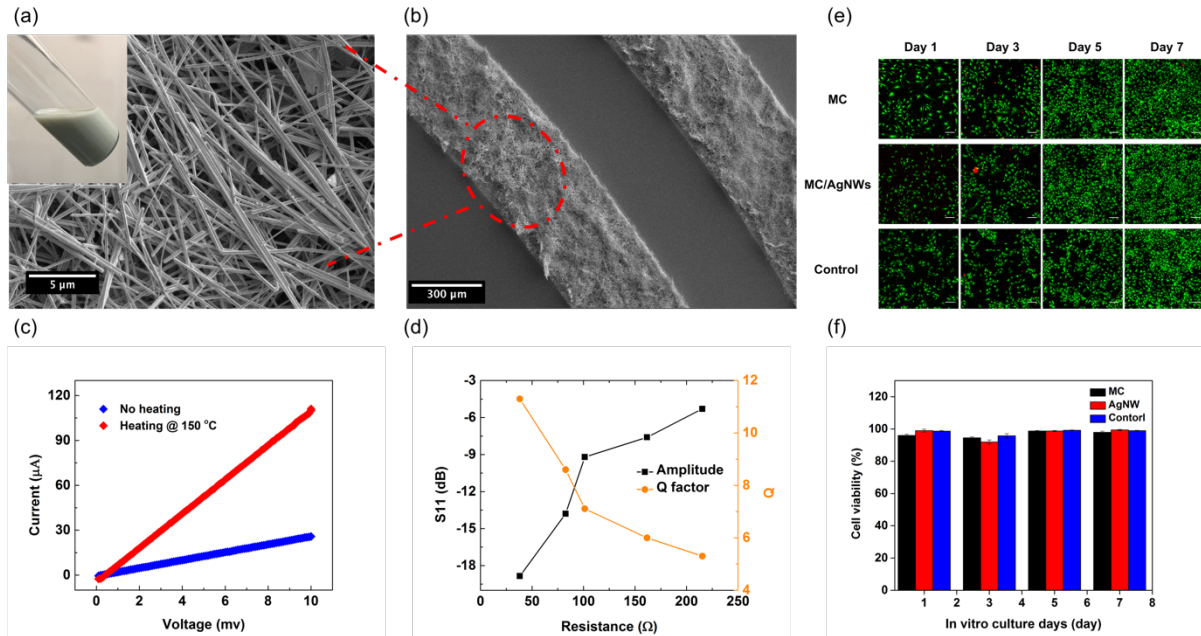


**Figure 3. 8** (a) A SEM image showing percolating conductive AgNW network. The inset photograph depicts a bottle of 4% (w/v) AgNW suspension. (b) A SEM image of patterned AgNW traces on top of a clean silicon wafer. (c) Measured resistance of patterned AgNW circuits processed at different temperatures. (d) Measured results showing the correlation between antenna resistance versus the amplitude of S11 parameter and the Q factor. (e) Fluorescence microscopy images of Human Umbilical Vein Endothelial Cells (HUVECs) stained with calcein-AM (green/live), and propidium iodide (red/dead). (Scale bar: 200  $\mu\text{m}$ ). (f) Statistical result of viability of HUVECs in the presence of MC, MC/AgNWs composites and no additional treatment on day 1, 3, 5, and 7 of culture.

To ensure stable and useful performance in a warm aqueous environment, it is crucial to first optimize the resonant behavior of the patterned antenna circuits prior to being embedded into polymeric matrix. One primary aspect is to achieve efficient coupling between the primary probe and fabricated circuits such that majority of the electromagnetic energy can be delivered to the antenna at resonant frequency. To achieve this, we attempted to minimize impedance mismatch by reducing the contact resistance of the conductive nanowire networks.<sup>90,127</sup> Figure 3.8b shows a SEM image of a patterned spiral AgNW circuit on top of a silicon wafer. The dimensions of the individual silver nanowires were 50 nm diameter and 100-200  $\mu\text{m}$  length. The measured

conductivity of 3- $\mu\text{m}$  high patterned AgNW traces is  $9100 \text{ S cm}^{-1}$  (sheet resistance of  $\sim 0.04 \text{ } \Omega/\text{sq}$ ). Figure 3.8a depicts a higher magnification view of this AgNW network and the inset photo shows a bottle of 4 wt% AgNW suspension in ethanol employed for solution casting. To avoid nanowire aggregation, the AgNW suspension was sonicated for 30 min prior to use.

Previous work has demonstrated that high-temperature thermal treatment of percolating AgNW networks yields enhanced electrical conductance due to the reduction of junction resistance among nanowires, which under this context gives an improved return loss.<sup>128</sup> Therefore, to improve the performance of the antennas based on conductive nanowires, we exploited a thermal sintering approach by heating percolating AgNW networks in a vacuum oven at  $150 \text{ } ^\circ\text{C}$  for 30 min. Figure 3.8c shows characteristic results of identical circuits with and without thermal treatment. The blue plot represents I-V curve of a sample prepared at room temperature and the measured conductance was  $0.0028 \text{ S}$ . In contrast, after heating at  $150 \text{ } ^\circ\text{C}$  for 30 min (red curve), the measured conductance was  $0.01 \text{ S}$ , indicating a roughly 3-fold improvement. Quality factor (Q) and return loss are two critical parameters that describe the resonant behavior of RF antennas. To investigate the correlation between the conductance of resulting circuits and S11/Q factor, we fabricated several antenna devices, all of which shared the same geometry but exhibited different resistances. Upon measuring such devices, there is a clear trend that antennas with smaller resistance exhibit higher Q factor and larger amplitude of S11, demonstrating enhanced resonant behavior (Figure 3.8d). For example, Q factor and  $|S_{11}|$  of an antenna whose resistance is  $36 \text{ } \Omega$  is 11 and 18 dB, which, in contrast, is one order of magnitude higher than those whose resistance is larger than  $300 \text{ } \Omega$ .

In our attempt to verify the biocompatibility of construction materials, cell culture experiments were performed using standard cell culture plates (6-well) coated with pure MC or

composites made of MC and AgNWs. Human umbilical vein endothelial cells (HUVECs, Angio-Proteomie) were grown in the presence of three different conditions: pure MC, composites made of MC and AgNWs, and standard tissue culture plastic (as a control). For all conditions, the surface was first treated with 0.1% porcine gelatin to enhance adhesion. To visualize viability, HUVECs were subsequently stained with calcein-AM (live/green), and propidium iodide (dead/red). As shown in Figure 3.8e and f, materials used for construction of thermoresponsive transient systems exhibit marginal cytotoxicity to HUVECs from day 1 to day 7.

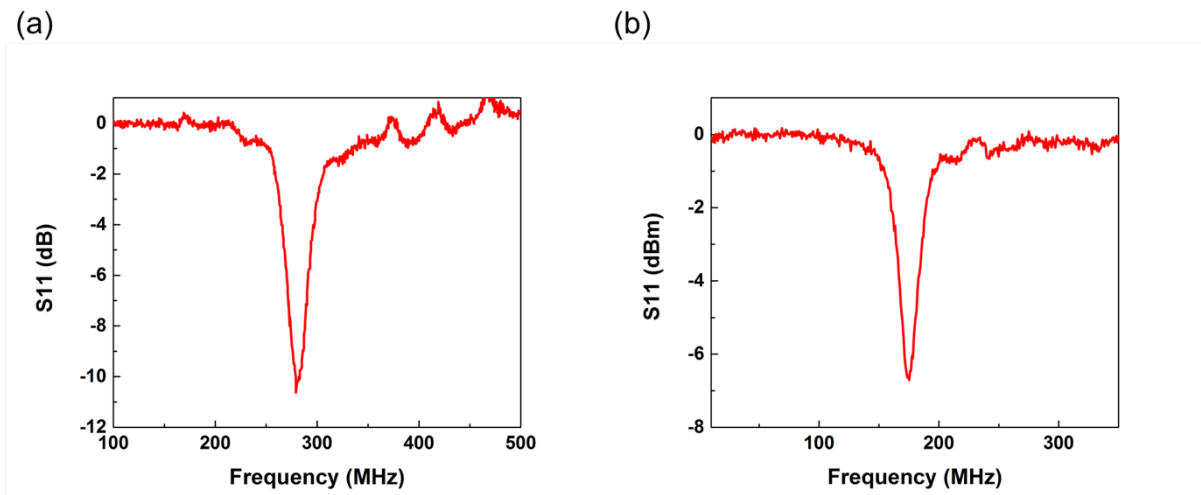


**Figure 3. 9** Measured S11 of MC-based RFID device in ambient dry environment (a) and immersed in warm solution (b)

In order to demonstrate on-demand transience triggered by cooling, we immersed a MC-based transient antenna into phosphate buffered saline (PBS) solution, which was preheated to 50 °C using a computer-controlled hot plate (IKA/RET control-visc). As schematically illustrated in Figure 3.10a, a LabView interface was used to monitor S11 versus frequency over the 10 MHz to 500 MHz frequency range throughout the entire experiment. When the device was initially immersed in PBS, we observed a shift in resonant frequency as shown in Figure 3.9, which is

likely caused by changes in the dielectric properties and swelling of the MC substrates. Figure 3.10b shows S11 measured via a wireless interface from the same transient device in response to temperatures above (red curve) and below (blue curve) the LCST. As the solution temperature was initially above the LCST, we first measured a sharp resonant peak appearing at 153.8 MHz with an amplitude of 7 dB. However, as the solution temperature cooled below LCST, this resonant response quickly disappeared. In order to examine the stability of this response in a warm bath, wireless measurements of S11 of a transient antenna were performed at 5-minute intervals. As illustrated in Figure 3.10d and 3.10e, a stable S11 spectrum can be wirelessly obtained over 7 days from an antenna immersed in a warm PBS bath. More importantly, when the solution temperature was allowed to cool below the LCST, an abrupt loss of resonant response was quickly observed due to the dissolution of the MC substrates (which in turns led to disintegration of the embedded conductive network) (Figure 3.10f). Figure 3.10c shows photographs of a thermoresponsive transient antenna at different solution temperatures. The transient circuit survived (but swelled) when immersed in warm PBS solution ( $T_{\text{PBS}} > \text{LCST}$ ). Then, the entire transient circuit gradually dissolved when the solution temperature dropped below the LCST. Finally, complete dissolution of MC substrates and disintegration of nanowire-based circuits were observed, leaving only the parylene encapsulating layers floating in the bath.

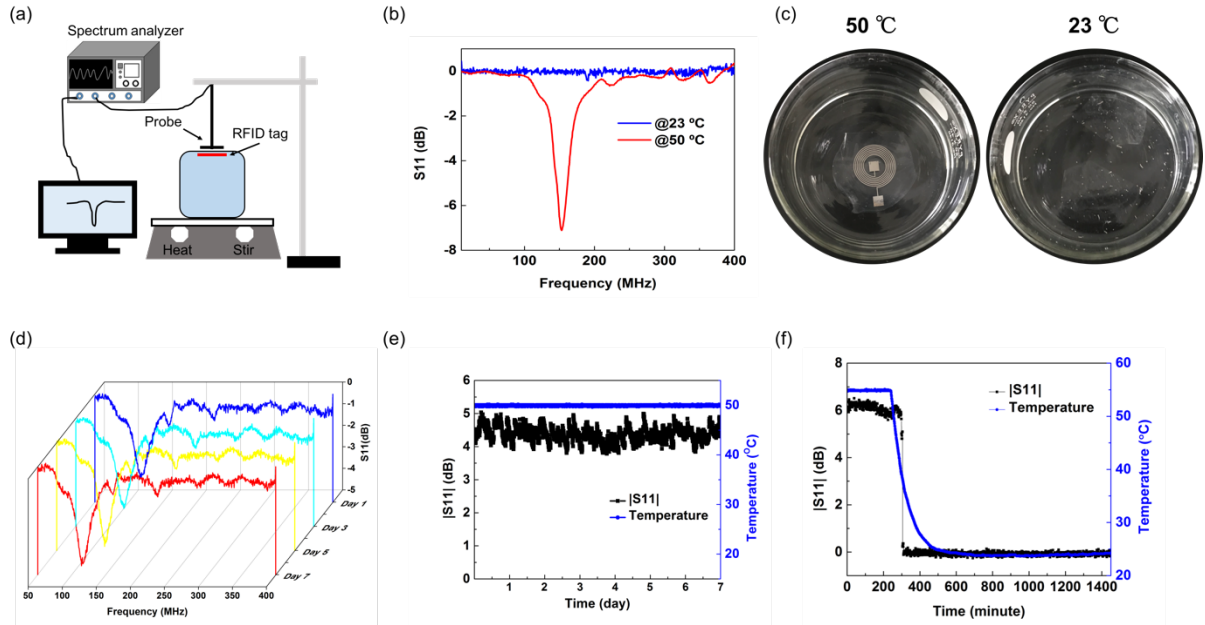


**Figure 3. 10** (a) Experimentally measured return loss of a transient RFID antenna in warm/cold water. (b) Stability test showing the variation of amplitude of S11 over 24 h in 50 °C water bath. (c) Thermally triggered transient behavior that shows dramatic S11 change due to a cooling trigger, occurring at 38 °C. (d)-(f) A set of photographs that visualize morphology alteration of transient RFID antenna in a water bath at 50, 38, and 22 °C.

### 3.4 Conclusion

In conclusion, a suite of techniques was developed to enable fabrication of temperature-sensitive transient RF antennas that can provide stable wireless response in warm aqueous environments but disintegrate and no longer respond when cooled below a critical temperature. Finally, our thermoresponsive transient RF antenna represents an important step towards the realization of wireless medical implants whose transience can be triggered at any given time by an external cooling stimulus.



## Chapter 4 Thermal Transport in Electrospun Polymer Nanofiber

### 4.1 Introduction

Polymers are an important class of materials due to their desirable and tunable properties, abundance, and low cost. A long-standing issue for polymeric materials that limits their applications in many fields is their extremely low thermal conductivities (on the order of  $0.1 \text{ W m}^{-1} \text{ K}^{-1}$ ), which is due to the random network formed by the carbon backbone and the weak inter-chain interactions mediated by weak van der Waals forces. This leads to poor heat dissipation that largely restricts polymer usage and imposes severe limitations in various applications such as light-emitting devices,<sup>129,130</sup> photovoltaic cells,<sup>131,132</sup> and flexible thin-film transistors.<sup>133,134</sup> To address this issue, a significant amount of efforts have recently been dedicated to enhancing the thermal conductivity ( $\kappa$ ) of polymeric materials.<sup>135–141</sup>

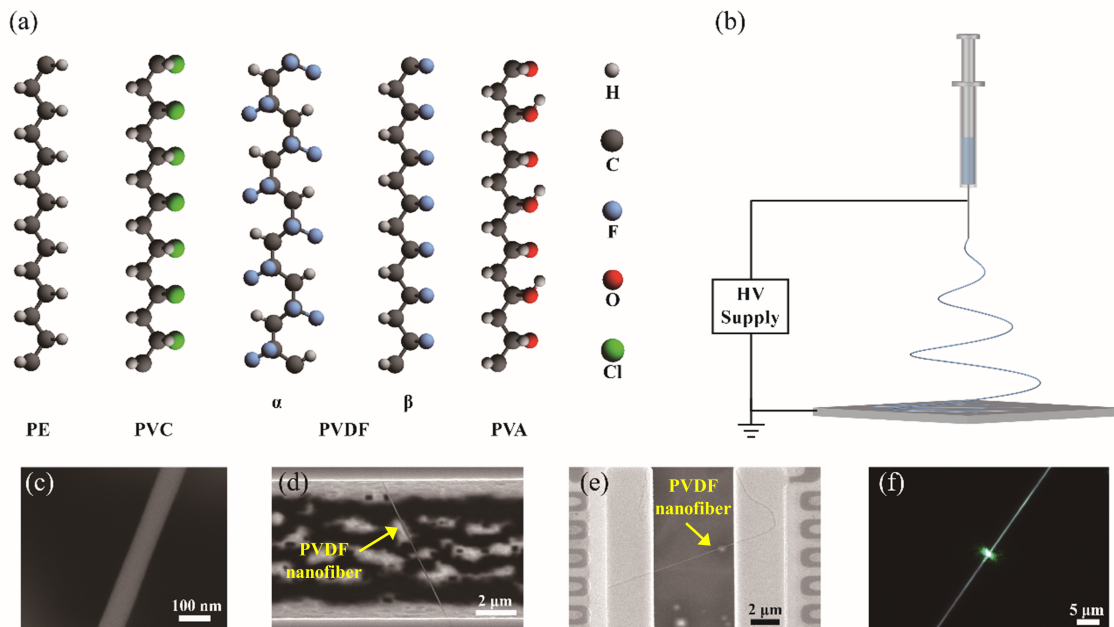
It is well-known that the low thermal conductivity of most polymeric materials is a result of their molecular structure generally consisting of coiled-up chains entangled together. The thermal conductivity along individual molecular chains, however, can actually be quite good because of the strong intra-chain covalent bonding between atoms. In fact, a recent molecular dynamics (MD) simulation<sup>135</sup> has suggested that an isolated single polyethylene (PE) molecule may possess very high thermal conductivity, up to  $\sim 350 \text{ W m}^{-1} \text{ K}^{-1}$ . Inspired by this prediction, several experimental efforts have focused on enhancing the thermal transport properties of polymer nanofibers with aligned molecular chains.<sup>136,140,142–144</sup> The highest experimentally measured thermal conductivity of a polymeric material was reported by Shen et al.,<sup>136</sup> who reported on single ultra-drawn PE nanofibers with thermal conductivity values as high as  $\sim 104 \text{ W m}^{-1} \text{ K}^{-1}$ . This dramatic enhancement of thermal conductivity is due to the fact that small

crystallites, split from the crystalline lamellas and connected by microfibrils, are aligned along the fiber axis during the drawing process, yielding a high degree of molecular orientation.<sup>136</sup>

Electrospinning has become a popular approach to prepare nanofibers for various applications, with polymers being the most common type of materials used for electrospun fiber production. During electrospinning, a strong electric field forces a liquid jet from a droplet of dissolved polymer chains, and a continuous nanofiber is formed as the solvent evaporates in flight. The strong elongational flow in this jet often results in fibers with substantial molecular orientation, which may lead to significantly enhanced thermal conductivity along the fiber direction. For example, it has been shown that the thermal conductivity of single Nylon-11 electrospun fibers may be as high as 1.6 W/m-K, nearly one order of magnitude higher than the typical bulk value of  $\sim 0.2$  W/m-K.<sup>142</sup> In addition, Canetta et al. measured the thermal conductivity of individual electrospun polystyrene nanofibers, obtaining values ranging from 6.6 to 14.4 W/m-K, a significant increase from typical bulk values.<sup>144</sup> Ma et al. recently showed that the thermal conductivity of electrospun PE nanofibers may be as high as  $9.3 \text{ W m}^{-1} \text{ K}^{-1}$  at 300 K, over 20 times higher than the bulk value, an increase that was attributed to ordered molecular chain alignment and enhanced crystallinity as indicated by Raman spectroscopy.<sup>140</sup>

In addition to chain alignment and crystallinity, polymer topology and morphology has also been demonstrated to affect the thermal conductivity of polymeric materials.<sup>145,146</sup> For example, a recent MD simulation has shown that longer side chain of bottlebrush polymers will increase interchain phonon scattering and decrease the thermal conductivity;<sup>145</sup> and for  $\pi$ -conjugated 2D polymers, the calculated lower thermal conductivity with increasing porosity is attributed to the increased chain disorder and segmental rotation.<sup>146</sup> While notable progress has been made, several key questions related to the effects of molecular structure on thermal transport in

electrospun polymer nanofibers still remain to be answered. For example, no experimental study has been done to investigate the effects of molecular weight (i.e. chain length) and side groups on thermal transport in individual electrospun polymer nanofibers. In this paper, we show how these two factors influence the thermal conductivity of electrospun vinyl nanofibers, which share the same planar-zigzag carbon backbone. Given that electrospinning has become a widely-adopted approach to produce large amount of polymer nanofibers, this study could provide knowledge to fine tune the electrospinning process to obtain high thermal conductivity electrospun polymer nanofibers.

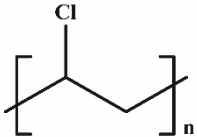
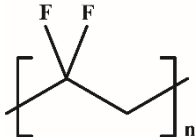
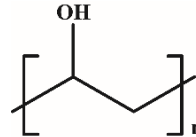
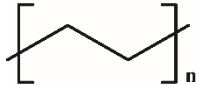


**Figure 4. 1** (a) Molecular structure of PE, PVC, PVDF ( $\alpha$  &  $\beta$  phase) and PVA. (b) Schematic of electrospinning setup. (c) An SEM micrograph of a PVDF nanofiber. (d) An SEM micrograph of a PVDF nanofiber suspended over a Si trench. (e) An SEM micrograph of a PVDF nanofiber suspended on thermal measurement device. (f) Optical image showing the laser focused on individual nanofiber for Raman measurement.

## 4.2 Methods and Materials

To investigate the effects of molecular weight ( $M_w$ ) and side groups, we prepared four

different kinds of electrospun vinyl nanofibers: PE, polyvinylidene fluoride (PVDF), polyvinyl alcohol (PVA) and polyvinyl chloride (PVC). Based on the PE powders that were commercially available, we fabricated PE nanofibers with four different  $M_w$  (chain lengths), namely 35,000, 125,000, 420,000, and 3,000,000 (Supporting Information). For the other three materials used, we tried to keep the chain length as similar as possible (as listed in Table 1). These vinyl polymers have similar chain structures (Figure 4.1a), with identical carbon backbones but different side group atoms. Since it has been shown that the electric field strength in the electrospinning process plays a critical role in the thermal conductivity of resulting PE nanofibers,<sup>140</sup> in this study we adopt fixed values for both the applied voltage (30 kV) and the distance (15 cm) between the syringe tip and the collector to keep the electric field constant, as shown in Figure 4.1b. Figure 4.1c shows a high magnification scanning electron microscopy (SEM) micrograph of an individual electrospun PVDF nanofiber. During the electrospinning process, the nanofibers can be collected on silicon chips that have pre-patterned trenches (Figure 4.1d) for micro-Raman studies and Young's modulus characterization. For thermal conductivity characterization, the fibers were collected with a piece of polydimethylsiloxane (PDMS) to facilitate subsequent sample transfer to the measurement device (Figure 4.1e), which was then measured following a well-established approach.<sup>147-151</sup> As it has been shown that storage in a vacuum chamber can help to remove solvent residues,<sup>140</sup> all fibers were kept in a vacuum chamber overnight prior to any measurements.

	PVC	PVDF	PVA	PE
<b>Formula</b>				
<b>M<sub>w</sub></b>	~233,000	~180,000	146,000 -186,000	~125,000
<b>Monomer Weight</b>	62.50	64.03	44.05	28
<b>Chain Length</b>	~3728	~2811	3314 - 4222	~4464
<b>K<sub>Bulk</sub> (W m<sup>-1</sup> K<sup>-1</sup>)</b>	0.13 <sup>152</sup>	0.13 <sup>152</sup>	0.31 <sup>153</sup>	0.3-0.42 <sup>154</sup>
<b>K<sub>Fiber</sub> (W m<sup>-1</sup> K<sup>-1</sup>)</b>	0.5±0.033	0.91±0.094	1.58±0.071	1.91±0.12
<b>Density (kg/m<sup>3</sup>)</b>	1380	1780	1190	910-940
<b>E<sub>single chain</sub> (GPa)</b>	160 <sup>155</sup>	77(α) / 237(β) <sup>156</sup>	287 <sup>156</sup>	374 <sup>157</sup>
<b>T<sub>g</sub> (°C)</b>	80 <sup>158</sup>	-35 <sup>154,159</sup>	85 <sup>154</sup>	-78 <sup>160</sup>

**Table 4. 1** Properties of four vinyl polymer materials, including: formula, molecular weight ( $M_w$ ), monomer weight, molecular chain length, room temperature thermal conductivity ( $k$ ), calculated single chain Young's modulus ( $E_{\text{single chain}}$ ), and glass transition temperature ( $T_g$ ).

### 4.3 Results and Discussion

Figure 4.2a shows the measured thermal conductivity for PE nanofibers composed of molecular chains with four different values of  $M_w$ . For each  $M_w$ , we tested three samples, and it can be seen that even though some variations exist for samples within each group, there is a clear trend of higher thermal conductivity for fibers with larger  $M_w$ . Specifically, the room-temperature thermal conductivity increases from 1.2 to 4.8 W/m-K as  $M_w$  increases from 35,000 to 3,000,000. The relationship between the thermal conductivity and  $M_w$  for bulk PE was studied back in the 1960s but without much follow-up work since then. For molten PE at 140°C, it was

shown that the thermal conductivity increases with  $M_w$  (roughly proportional to  $\sqrt{M_w}$ ) and saturates as  $M_w$  approaches  $\sim 140,000$ .<sup>161,162</sup> As Umklapp scattering becomes important at room temperature, we plot the measured thermal conductivity of the PE nanofibers at 200 K as shown in Figure 4.2b, which displays a thermal conductivity escalation at a rate that is approximately proportional to  $\sqrt{M_w}$ . However, a notable difference is that for nanofibers, the increasing trend does not saturate until a much higher molecular weight, at  $M_w > 1,000,000$  as projected from the plot. It is not surprising that the saturation regime depends on the phase of the sample (solid vs molten), as the anisotropy in the electrospun nanofiber (unlike in the stationary molten sample) allows for a greater degree of molecular orientation and thus more potential for thermal conductivity enhancement at higher  $M_w$ . In other words, in a static molten sample, the advantages provided by high  $M_w$  are only manifested to a relatively low level due to lack of molecular orientation.

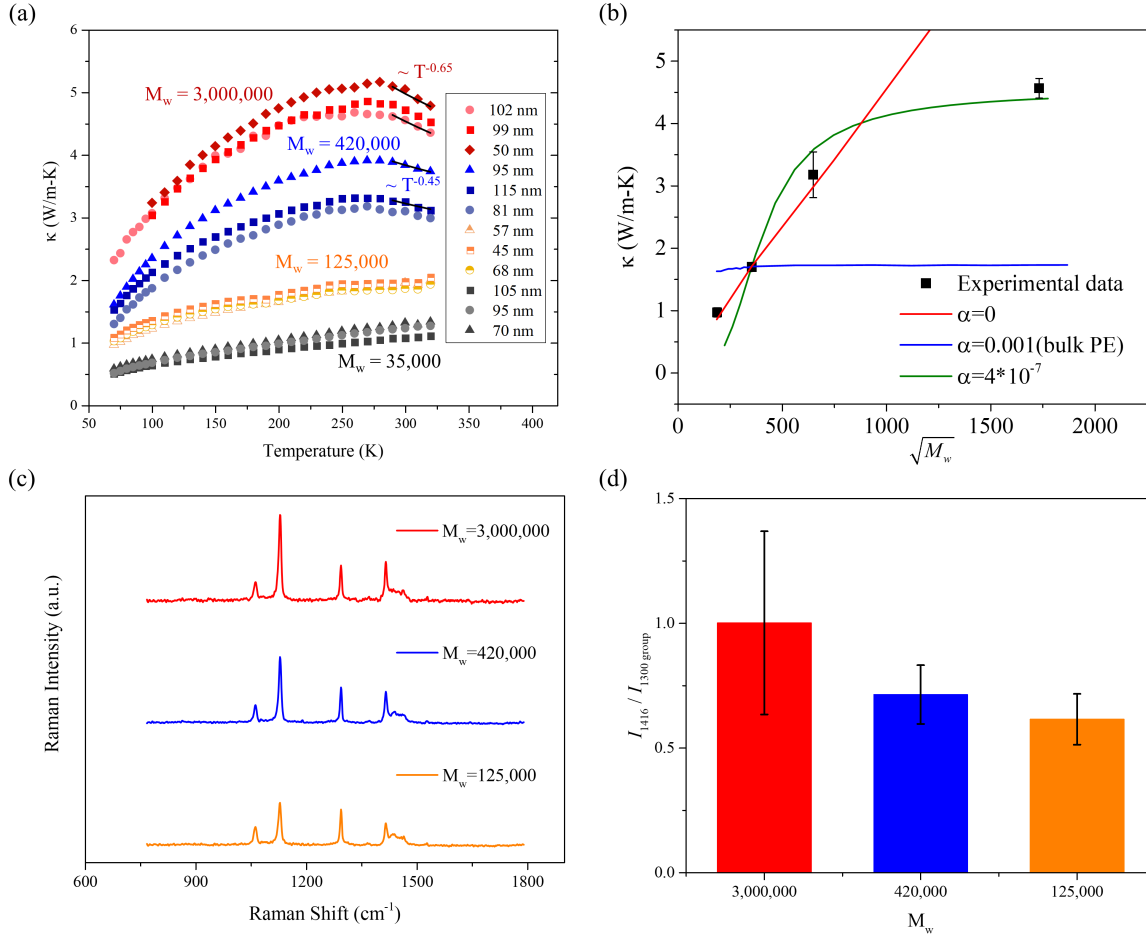


**Figure 4. 2** (a) Measured thermal conductivity of PE nanofibers with different molecular weights in the temperature range of 70-320 K. (b) Measured thermal conductivity of PE nanofibers at 200 K as a function of the square root of the molecular weight. The green curve is a fit from a model that considers the anisotropic heat flux along and across the molecular chains,<sup>161,162</sup> and the red as well as blue lines are the calculated results when  $\alpha = 0$  or 0.001 (bulk PE), respectively. (c) Raman spectra acquired for PE nanofibers with  $M_w$  of 3,000,000, 420,000, and 125,000, respectively. (d) The calculated intensity ratio of I1416/I1300 group, indicating the fraction of orthorhombic crystalline phase of PE nanofibers, increases with molecular weight. The error bars indicate the standard deviation of the intensity ratio of I1416/I1300 group measured from several nanofibers.

The relation between thermal conductivity and  $M_w$  for bulk isotropic polymers has been explained by a theoretical model developed by Hansen and Ho,<sup>161,162</sup> and it is shown that the conductivity increase depends strongly on a parameter  $\alpha$ , which is related to the ratio of inter-

chain to intra-chain interaction strength. When this ratio goes to zero, a linear relationship between the thermal conductivity and  $\sqrt{M_w}$  can be obtained. We note that Hansen and Ho indicated that, for bulk isotropic polymers, while the ratio of inter-chain to intra-chain interaction strength is quite small with  $\alpha \sim 0.001$ , the dependence of thermal conductivity on  $M_w$  for bulk polymers can still deviate significantly from the theoretical  $\sqrt{M_w}$  dependence. For the electrospun PE nanofibers tested in this work, we applied the same theoretical model,<sup>161,162</sup> and the best fit to the experimental data yielded an  $\alpha$  value of  $4 \times 10^{-7}$  (Figure 4.2b). This suggests that the improved chain alignment in these polymer nanofibers may enhance thermal energy transfer along the chain (relative to cross chain transfer), which leads to saturation at a higher  $M_w$ , as well as an enhanced thermal conductivity at saturation (compared to bulk amorphous PE). It is worth noting that the model was developed for bulk isotropic polymers, so the above fitting results should only be viewed as a qualitative understanding of the trend.

The temperature dependence of the thermal conductivity of electrospun PE nanofibers for different  $M_w$  also presents interesting trends. In Figure 4.2a, the PE nanofibers with lower  $M_w$  (35,000 and 125,000) exhibit monotonically increasing thermal conductivity *versus* temperature, typical for amorphous materials. However, for higher  $M_w$  (420,000 and 3,000,000), a peak thermal conductivity appears as temperature increases, which is a signature of phonon Umklapp scattering occurring in crystalline solids. For fibers with a molecular weight of 420,000, the thermal conductivity data demonstrate a  $T^{-0.45}$  temperature dependence in the high temperature regime. As  $M_w$  further increases to 3,000,000, the drop rate escalates to a  $T^{-0.65}$  temperature dependence, indicating increased crystallinity. Interestingly, this trend is different from what has been observed in other PE systems which have crystallized from a molten state and show decreased crystallinity at higher  $M_w$ .<sup>163–167</sup>



To further understand this, we measured the crystallinity of PE nanofibers with different  $M_w$  using Raman spectroscopy.<sup>140</sup> Figure 4.2c shows the Raman spectra of PE nanofibers with  $M_w$  of 125,000, 420,000 and 3,000,000. For low  $M_w$  PE (which is expected to contain numerous small and imperfect lamellar crystallites) the crystalline units have been shown to melt at relatively low temperature.<sup>168</sup> Notably, Samuel *et al.*<sup>169</sup> observed that small temperature increases could cause the crystalline degree of PE with  $M_w = 35,000$  to drop even at temperatures slightly above room temperature. Thus, the Raman spectra of PE nanofibers with  $M_w = 35,000$  are unlikely to reflect their as-fabricated crystallinity due to heating from the laser; these fibers were therefore not included in this comparison. However, when the  $M_w$  is increased to 52,000, previous research indicates that PE crystallinity is insensitive to temperature until it reaches close to the melting point.<sup>169</sup> It is well established that the Raman band at  $1416\text{ cm}^{-1}$  is due to the orthorhombic crystalline phase of polyethylene.<sup>167,169-171</sup> The  $\text{CH}_2$  twisting vibration modes around  $1300\text{ cm}^{-1}$  are generally used for normalization.<sup>171</sup> According to Naylor's model,<sup>171</sup> the orthorhombic crystallinity can be calculated using:

$$\% \text{ orthorhombic crystallinity} = \left( I_{1416} / I_{1300 \text{ group}} \right) \times (100 / 0.45) \times K, \quad (1)$$

where  $I_{1416}$  refers to the area of the Raman band at  $1416\text{ cm}^{-1}$ ,  $I_{1300 \text{ group}}$  is the area underneath the  $1300\text{ cm}^{-1}$  band group (internal standard), and  $K$  is a constant correction factor. As shown in Figure 4.2d, the  $I_{1416}/I_{1300 \text{ group}}$  ratio increases with  $M_w$ , suggesting that the electrospun PE nanofibers with higher  $M_w$  have a larger volume fraction of orthorhombic crystalline phase, consistent with both the observed molecular weight dependence and temperature dependence of the measured thermal conductivity in Figure 4.2a.

In addition to the molecular chain length, it has been predicted that the side groups in vinyl polymers may alter the vibrational properties of thermal phonons and have important effects on

the thermal conductivity.<sup>141,172</sup> However, to date, no systematic experimental studies have been conducted to compare the effects of side groups. As such, we also measured three other types of vinyl polymer nanofibers (PVA, PVC, and PVDF), and compared their thermal conductivities with that of PE. The four groups of vinyl polymers all have the same carbon backbone with different side groups, as described in Table 1. In considering the side group effects, we carefully select the molecular weight to ensure that the molecular chain length is similar for different vinyl nanofibers.

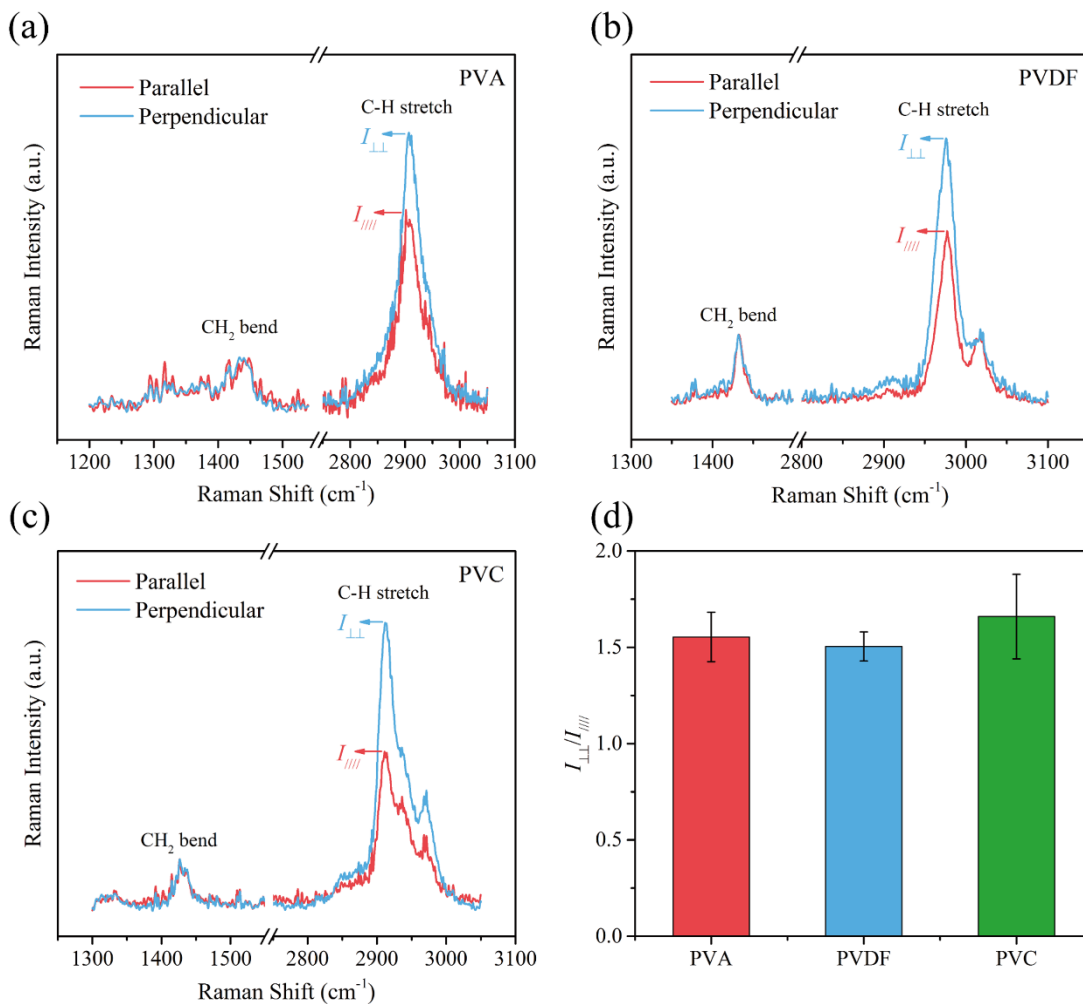


**Figure 4. 3** Polarized Raman spectra of (a) PVA, (b) PVDF, and (c) PVC nanofibers with the laser beam polarized parallel (the red curve) and perpendicular (the blue curve) to the fiber axis. (d) Values for  $P = I_{\perp} / I_{\parallel}$ , a ratio that semi-quantitatively characterizes the molecular orientation in PVA, PVDF, and PVC nanofibers.

In a previous study, we used Raman spectroscopy to characterize the molecular chain orientation in electrospun PE nanofibers.<sup>140</sup> However, unlike PE, for which comprehensive Raman studies have been reported and specific parameters corresponding to different vibration modes are known and can be used to characterize the molecular chain alignment, the Raman information for the other three vinyl fibers is not as extensive. Nonetheless, we were still able to obtain some information about molecular chain alignment with polarized Raman spectroscopy on PVA, PVC, and PVDF nanofibers.

During these Raman studies, we first confirmed that laser irradiation of individual polymer nanofibers did not cause structural damage by performing the Raman spectroscopy at the same position five times in a row. For PVA, PVC, and PVDF nanofibers, the intensities of the C-H stretching vibration modes at 2900 to 3000  $\text{cm}^{-1}$  strongly depend on the angle between the incident laser polarization and the fiber axis, and the intensity reaches its maximum and minimum at the angle of  $90^\circ$  and  $0^\circ$ , respectively. Therefore, these bands can be used to semi-quantitatively evaluate the degree of chain orientation in the nanofibers. Following the same approach as in a previous study,<sup>173</sup> we examine the parameter,  $P = I_{\perp\perp} / I_{\parallel\parallel}$ , as an index of the molecular orientation in the nanofibers. Here  $I_{\perp\perp}$  and  $I_{\parallel\parallel}$  refer to the intensities of the C-H stretching vibration modes when the polarizations of the incident and scattered laser light are perpendicular and parallel to fiber axis, respectively. As shown in Figure 4.3a-c, for all PVA, PVC, and PVDF,  $I_{\perp\perp}$  is stronger than  $I_{\parallel\parallel}$  and the derived  $P$  values (Figure 4.3d) are all around 1.5, indicating that the molecular chains are aligned along the nanofiber axis direction as a result of the strong elongational force during the electrospinning process. We note that for bulk polymers with randomly oriented molecular chains, the  $P$  value is approximately unity.

The measured thermal conductivities in the temperature range of 100 K to 320 K for all four

kinds of vinyl polymer nanofibers are shown in Figure 4.4a. For PE, we used nanofibers with  $M_w \sim 125,000$  for comparison, as this molecular weight gives a molecular chain length similar to the other three types of fibers. This way, the difference in thermal conductivity between different varieties of nanofiber is most likely due to the variation in side groups, instead of other factors. Compared to the thermal conductivities for bulk polymers (Table 1), Figure 4.4a indicates that all the electrospun polymer nanofibers have enhanced thermal conductivities that are approximately 4-7 times higher than the corresponding bulk value at room temperature, again suggesting more aligned molecular chains in the electrospun nanofibers.

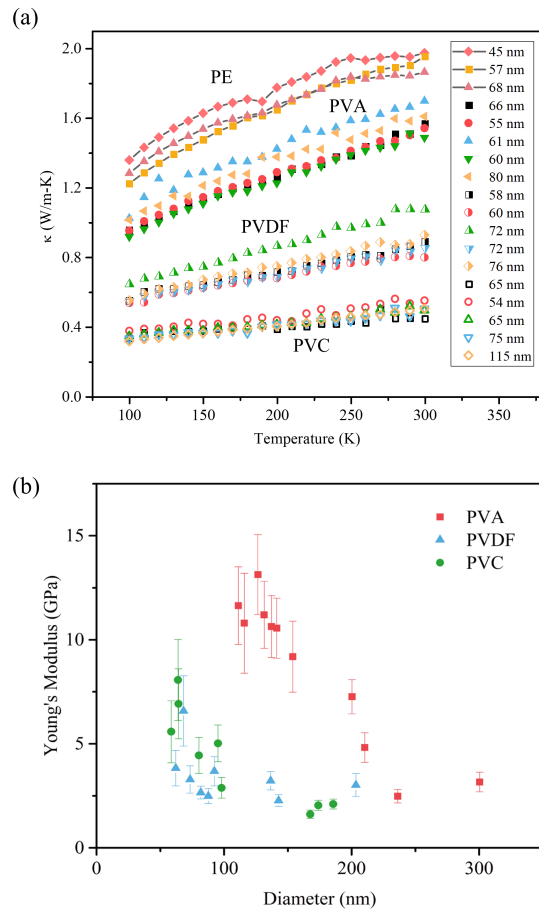


**Figure 4. 4** (a) Comparison of measured thermal conductivity of electrospun PE, PVA, PVDF, and PVC nanofibers. (b) Measured Young's moduli of PVA, PVDF and PVC nanofibers of different diameters.

Figure 4.4a also indicates that even though the thermal conductivity for each type of vinyl polymer fibers varies from fiber to fiber, the difference between different types of fibers is large enough to draw the conclusion that  $\kappa_{PE} > \kappa_{PVA} > \kappa_{PVDF} > \kappa_{PVC}$ . This represents a general trend that the thermal conductivity decreases as the side groups becomes heavier. It has been shown theoretically that thermal phonons preferentially transport along the covalently-bonded carbon-carbon backbones in PE, and with the light hydrogen atoms as the side group, acoustic phonons in the range of 0~15 THz are the dominant heat carriers due to their high group velocities and long mean free paths.<sup>135,141,174</sup> As one hydrogen atom is replaced by a heavier group (OH, Cl or F), the unit cell becomes heavier and new optical phonon mode branches with lower frequencies appear. It is generally accepted that heavier unit cells correspond to lower phonon group velocities and hence lower thermal conductivity.<sup>175-177</sup> In addition, the reduced energy gap between acoustic and optical phonons may facilitate phonon Umklapp scattering to pose more resistance to thermal transport. Indeed, our experimental data are consistent with numerical modeling results showing that as the side group atomic mass increases, the acoustic phonons in the same frequency range contribute much less to thermal transport due to mismatch between the vibration modes of neighboring carbon atoms along the molecular chain.<sup>141</sup> In fact, it is shown that the acoustic phonon contribution becomes very low as the side group atomic weight increases to 127 g/mol.<sup>141</sup>

One more observation is that, while the atomic masses of the side groups for PVDF and PVC are similar (40 g/mol *versus* 38.5 g/mol), the thermal conductivities of these two groups of nanofibers can still be quite different. In fact, the measured room-temperature thermal conductivity of PVDF nanofibers is roughly 80% higher than that of PVC nanofibers, which suggests that, in addition to the side group weight, the atomic structure or arrangement may also

play a role. It is worth noting that while both  $\alpha$  and  $\beta$  phases may exist in electrospun PVDF nanofibers, our Raman data indicate that the intensity of the Raman peak at  $839\text{ cm}^{-1}$  is much stronger than that at  $794\text{ cm}^{-1}$ , suggesting that the  $\beta$  phase is the predominant crystal form in the fiber.<sup>178</sup>  $\beta$  phase PVDF shares the same planar-zigzag carbon backbone structure as PE, PVA, and PVC, ensuring a fair comparison between these different polymer nanofibers.

When comparing the molecular structure of PVC to that of PE, one can see that, in a PVC molecule, each monomer unit has one side H atom substituted with a Cl atom. In a PVDF molecule, however, both H atoms (attached to the same C atom) are replaced by F atoms, as shown in Figure 4.1a. While the details behind the reason for why the PVDF nanofibers exhibit higher thermal conductivity than the PVC nanofibers will have to be determined by future in-depth molecular modeling, we believe that the increased symmetry found in the arrangement of the F atoms in PVDF might play a role. In an earlier report, a molecular dynamics simulation on a single PE molecule indicated that the thermal conductivity drops significantly when 25% of the side H atoms are replaced by heavier F atoms (drop of 64%) or Cl atoms (drop of 66%).<sup>141</sup> However, when 50% of the H atoms are replaced in a uniformly spaced arrangement, the thermal conductivity is 60% (F substitute) and 32% (Cl substitute) higher than the 25% replacement situation, respectively, indicating that symmetry plays an important role.<sup>141</sup> These modeling predictions suggest that phonons travel along polymer chains more effectively when side groups are either lighter or more symmetric.

It has been shown that the Young's modulus of ultra-drawn PE fibers is much higher than bulk values, and this enhancement may correlate with significantly enhanced thermal conductivity.<sup>157</sup> As such, we also examined the Young's moduli of electrospun PVA, PVC, and PVDF nanofibers and compared the results with the relative magnitude of their thermal

conductivities. As we did previously for Si nanoribbons and polymer nanofibers,<sup>179</sup> the Young's modulus was characterized by performing three-point bending tests on individual suspended nanofibers using an atomic force microscope (AFM, Bruker Dimension Icon). It can be seen from Figure 4.4b that different types of polymer nanofibers all demonstrate a higher Young's modulus value for smaller diameter samples, with a stronger size dependence for PVA and PVC than that for PVDF nanofibers. In fact, similar behavior has also been observed in other polymer nanofibers,<sup>180-182</sup> and the size-dependent Young's modulus could be attributed to the confinement of polymer chains near surfaces and in amorphous regions, the reduction of polymer chain entanglement, and the increase of the chain alignment for smaller sized nanofibers.<sup>180-183</sup>

Moreover, as shown in Figure 4.4b, the Young's moduli of the PVA nanofibers are much higher than those of the PVDF and PVC nanofibers (comparing nanofibers with similar diameters). Because the three different groups of polymer nanofibers are of the same backbone structure (planar zigzag) and similar in molecular chain length, the variations in the measured Young's modulus along the axial direction are likely due to differences in side group structure. It is known that Young's modulus is inherently related to atomic bond stiffness, and the stiffer bonds (higher modulus) observed in PVA (as compared to PVC) correlate well with the observed higher thermal conductivity. The Young's moduli of the PVDF nanofibers are, however, slightly lower than those of the PVC nanofibers, which is the opposite of the trend we observed for thermal conductivity. This is likely due to the different room temperature states for the different polymers. For semi-crystalline materials with amorphous regions, the Young's moduli will drop dramatically when the temperature increases from below to above the glass transition temperature,  $T_g$ .<sup>180</sup> In our experiments, the Young's moduli were all measured at room temperature, which is higher than the  $T_g$  of PVDF (-35°C)<sup>154,159</sup> but lower than the  $T_g$  of PVC

and PVA.<sup>154,158</sup> In this case, some secondary bonds of PVDF are broken, and molecules start sliding against each other.<sup>184</sup> Thus, during the measurements, the amorphous regions in the PVDF nanofibers were in a rubbery state (whereas the PVC and PVA were in a glassy state) which is likely the reason for the relatively low Young's moduli that were measured for the PVDF nanofibers. It is worth noting that for nanofibers,  $T_g$  could be slightly different from that of the bulk; however, the shift of  $T_g$  is usually not very significant. For example, for electrospun PVDF nanofibers with diameter from 50 nm-700 nm,  $T_g$  only increases up to  $-29.2^\circ\text{C}$ ,<sup>51</sup> still much lower than the room temperature at which we conducted the Young's modulus measurements.

#### **4.4 Conclusion**

We measured the thermal conductivity of individual nanofibers composed of various vinyl polymers with different molecular weights and side group atoms. Due to the fact that vibrational energy can propagate along the molecular chain more efficiently than between chains, the measured thermal conductivity increases monotonically with molecular chain length. By comparing the measured thermal conductivity of vinyl polymer nanofibers with different side groups, we found that phonons travel along polymer chains more effectively when side groups are either lighter or more symmetric. This knowledge describing the relationship between molecular structure and enhanced thermal properties in electrospun polymer nanofibers will help to better design future high-performance polymeric materials.



## Chapter 5 [ $^{18}\text{F}$ ]Fallypride Synthesis Using a Simple Microfluidic Device

### 5.1 Introduction

Non-invasive positron emission tomography (PET) is a valuable medical imaging method that relies on radioactive tracers to monitor specific physiological processes in the body.<sup>185</sup> A radiotracer is a chemical compound with one or more atoms replaced by short-lived positron-emitting radioisotopes, such as  $^{18}\text{F}$  or  $^{11}\text{C}$ , used to gather physiological information to assess health conditions.<sup>43</sup> The development of PET tracers has been impeded by the enormous infrastructure requirements needed to perform the necessary radioisotope production and subsequent radiochemical reactions that result in the desired radiotracer. Prohibitively large and expensive facilities, such as large-scale automated synthesis modules and “hot cells” widely used for the synthesis of radiopharmaceuticals, thwart the extensive distribution of PET tracers among less-developed but demanding communities. Additionally, due to radioactive decay, the transit time required to move reagents from a PET tracer production site to a clinic limits the flexibility and availability of critical imaging procedures, as a precise schedule involving numerous production facilities, professional technicians and patients must be assured in advance. Typically, the preparation of PET tracers is conducted near the cyclotron producing the radioisotope, which is not necessarily close to the patients requiring the necessary scans. The transit process from production site to imaging clinic results in a significant loss of radioactivity, which is particularly undesired for  $^{11}\text{C}$ -type short half-life radiotracers (half-life of 20.2 minutes).

The advantages of microfluidics, including high surface-to-volume ratio, minimized consumption of expensive chemicals and improved thermal exchange and reaction rate, suggest that this platform is particularly well suited for PET tracer production.<sup>29,186,187</sup> Several

microfluidic approaches pursuing rapid and efficient radiolabeling reactions have been reported in the past decade. Quake and colleagues first reported multistep synthesis of [ $^{18}\text{F}$ ]FDG based on a multi-layered microfluidic system incorporating on-chip pneumatically-actuated valves for fluid control.<sup>30</sup> While this system reported the production of 190  $\mu\text{Ci}$  of [ $^{18}\text{F}$ ]FDG with an impressive radiochemical yield of 38%, the limited capacity of the ion exchange volume significantly hindered the potential for processing more than 2-3 ml of [ $^{18}\text{F}$ ]fluoride mixture, and the multilayer on-chip valve system imposed a high level of complexity on microfluidic device fabrication and integration. Another microfluidic approach using an electrowetting-on-dielectric (EWOD) platform to control droplet movement demonstrated successful synthesis of four different radiotracers. However, the mechanism used for fluoride concentration in that platform limited its ability to handle several ml of the fluoride mixture, as repeatedly loading droplets of fluorine (in hundred- $\mu\text{l}$  volumes) would unavoidably lengthen the overall synthesis time.<sup>51,52</sup> Also, purification of the synthesized radiotracers was achieved via conventional off-chip processes, which hindered this platform's universality. The first human use of [ $^{18}\text{F}$ ]fallypride produced by a microfluidic batch-reactor has also been reported recently.<sup>56</sup> However, while this recent report did use a microfluidic chip as microreactor for the fluorination step, the fluoride concentration subsystem utilized a commercial ion-exchange cartridge (off-chip), and final purification step was accomplished via conventional HPLC (also off-chip), thereby missing the opportunity of integrating all steps of the production within a single, compact microfluidic chip. Although there has been exciting progress employing microfluidic technology for PET tracer synthesis, most efforts focus primarily on the investigation of a single step in the process, leaving other essential steps to be performed via conventional off-chip means. For instance, some articles have described various flow-through microfluidic devices for on-chip pre-concentration of

[<sup>18</sup>F]fluoride.<sup>188–190</sup> Moreover, numerous publications have reported the investigation of utilizing microfluidic chip for efficient radiochemical labeling reaction.<sup>45,50,53,191–195</sup> As a result, there is an opportunity to integrate all the essential modules onto a single microfluidic chip, enabling the synthesis of PET tracer from the very beginning (radioactive [<sup>18</sup>F]fluoride mixture) to the final stage (radiotracer ready for injection).<sup>45</sup> The goals of this highly-integrated microfluidic platform would include the following: (1) The entire production process should be fast and efficient, minimizing the decay of radionuclide and consuming minimal reagents. (2) The shield needed to protect users from radiation on the microfluidic chip should be simply achieved by using lead bricks, avoiding the need for large, bulky hot cells. (3) The microfluidic chip should be low-cost and disposable, and a fresh chip should be used for each individual radiotracer production run. (4) The microfluidic chip should be able to produce purified products in sufficient doses, ready for animal or human imaging. (5) The technique to produce the on-chip columns should be flexible enough to enable the production of various PET radiotracers by simply switching the materials packed inside the microchannel.

To achieve these desired goals and facilitate the development of novel PET tracers for both research and clinic applications, we report a simple microfluidic system that integrates several modules on a single chip to accomplish all principal steps for radiotracer production. To demonstrate the utility of this microfluidic chip, [<sup>18</sup>F]fallypride, a widely used radiotracer in PET imaging, is synthesized starting with [<sup>18</sup>F]fluoride retrieved from a nearby cyclotron (Figure 5.1). Instead of relying on complicated on-chip flow control components that require multiple levels of lithography and feature alignment (e.g. elastomer valves formed via aligned multilayer PDMS),<sup>193</sup> we employed simple off-chip mechanical valves to provide convenient and reliable control of reagent transfer between various modules. We also use an on-chip ion-exchange

column that is capable of concentrating a quantity of fluoride sufficient for several human doses. Inspired by previous designs of microfluidic batch reactors for radiochemical synthesis, we used an on-chip cavity that facilitates rapid drying and enables subsequent fluorination reaction. However, unlike previous efforts where HPLC or commercial C<sub>18</sub> cartridges were utilized for purification of the final product, we employed an on-chip C<sub>18</sub> column that was integrated with the previous modules. It is noteworthy that the microfluidic chip, incorporating all the on-chip modules for [<sup>18</sup>F]fallypride radiotracer production, is low-cost and disposable, allowing an operator to use a fresh chip for each on-demand PET radiotracer production run. The flow control elements (syringe pumps and mechanical valves) can be easily cleaned using ethanol or other appropriate solvents and are thus reusable. Using this microfluidic device, a small shielded space composed of several lead bricks would satisfy the requirements for radiation shielding, eliminating the need for a standard hot cell. Moreover, further automation of the pumps and valves could accelerate the entire process and shorten the overall synthesis time period, minimizing the loss of imaging reagents due to the decay of radionuclides. Variation of either the solid phase extraction (SPE) material or the elution methodology could allow our microfluidic platform to produce additional radiotracers. To adapt this microfluidic chip to a clinical setting, further development of the purification method is also required to achieve sufficient chemical purity. With excellent throughput, radiochemical purity and disposability, our microfluidic system represents a viable means to facilitate the production of radiotracers on demand and promote both the distribution and use of PET technology.

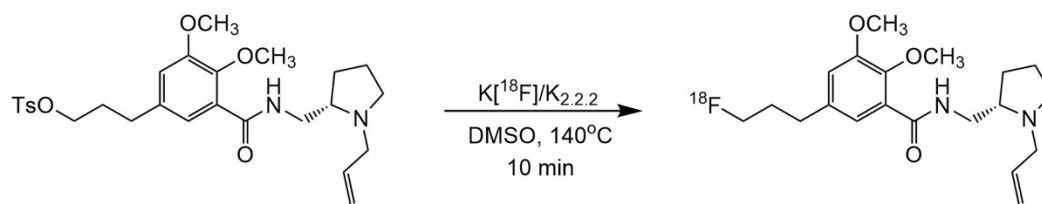


**Figure 5. 1** Synthesis process for the production of  $[^{18}\text{F}]$ fallypride.

## 5.2 Materials and Methods

The microchannel pattern was fabricated using facilities within the cleanroom affiliated with the Vanderbilt Institute of Nanoscale Science and Engineering (VINSE). A laser writer (Heidelberg  $\mu\text{PG}$  101) was utilized to create patterns on a silicon wafer using a 60  $\mu\text{m}$  thick layer of mr-DWL 40 resist. Then, liquid polydimethylsiloxane (PDMS) (Sylgard 184, part A and part B mixed in 10:1 ratio and degassed) was poured onto the resist-patterned silicon wafer located in a petri dish to produce a 1 cm thick layer. After curing in an oven (Thermo Scientific Lindberg/Blue M) at 65 °C for 12 h, the PDMS layer was peeled off the resist mold, and holes were punched at the inlet and outlet of the microchannels using a 1.5 mm internal diameter punch (Ted Pella). The patterned PDMS layer, along with a glass microscope slide (Fisher Scientific, Premium Plain Glass Microscope Slides), was exposed to an oxygen plasma (Harrick Plasma, PDC-001) for 60 seconds. Then, the two plasma-treated surfaces were bonded together and baked on a hot plate at 60 °C for 1 h before use. Next, the top surface of the microfluidic chip and a 0.2 mm thick PDMS film with a 1.5 mm size hole in the center were plasma treated again.

The square PDMS film was manually aligned such that the hole on the PDMS film was located at the center of reaction cavity, and subsequently bonded to the top of the reaction cavity. A coned NanoPort assembly (IDEX, N-333) was aligned and placed on top of the PDMS layer. Well-mixed PDMS was used as an adhesive and applied on the edge of the coned assembly, and then baked in an oven at 65 °C for 2 hours, such that the NanoPort was firmly attached to the top of the PDMS film. The microbore tubing (0.02" ID and 0.06" OD) was purchased from Cole-Parmer and inserted directly into the PDMS layer without using any tubing connectors. The average length of tubing used between the chip and the external valves was ~5cm. In all experiments, the microfluidic chip, hot plate and syringe pump were set inside a hot cell and we manually switched and reconnected the syringe for loading different reagents and N<sub>2</sub> behind the hot cell.

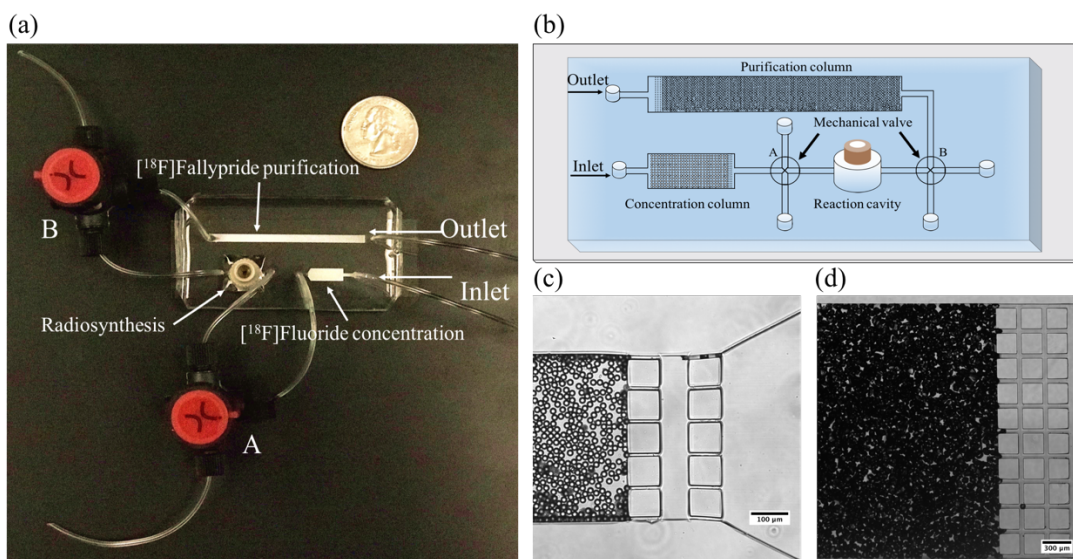


**Figure 5. 2** (a) A photograph of the microfluidic chip with an American twenty-five cent coin placed above. (b) A schematic illustration of the microfluidic chip employed for [<sup>18</sup>F]fallypride production, including a [<sup>18</sup>F]fluoride concentration column, fluorination reaction cavity and [<sup>18</sup>F]fallypride purification column. (c) A photograph of anion exchange beads trapped inside a microchannel by 10 μm gap PDMS pillars. (d) A photograph of reverse phase C<sub>18</sub> microparticles trapped inside a microchannel with 40 μm gap PDMS pillars.

Figure 5.2 shows both a schematic illustration and image of the microfluidic chip used for fallypride synthesis. Our device was composed of three main modules that served to concentrate the diluted [ $^{18}\text{F}$ ]fluoride mixture, perform the heat-assisted fallypride fluorination reaction, and purify the synthesized [ $^{18}\text{F}$ ]fallypride. The on-chip concentration column was 5 mm in width, 10 mm in length and 60  $\mu\text{m}$  in height. Anion exchange beads (Source 15Q, GE healthcare) were packed into the concentration column by introducing an ethanol solution containing suspended beads (10 mg/ml concentration) into the microfluidic channel. The desired quantity (3  $\mu\text{l}$ ) of anion exchange beads was trapped by a triple row of square PDMS pillars with 10  $\mu\text{m}$  gap near the outlet of microchannel. Unless noted elsewhere, we utilized 3  $\mu\text{l}$  anion exchange beads in later experiments and rat imaging. Then, the anion exchange beads were activated using 1.0 M of  $\text{KHCO}_3$  (0.2 ml) followed by flushing with 0.5 ml DI water (18  $\text{M}\Omega$ , Milli-Q Integral ultrapure water). The central reaction cavity was fabricated using an 8 mm inner diameter punch (Ted Pella). As our device was composed of a 1 cm thick PDMS top layer, the maximum volume allowed inside the cavity was 500  $\mu\text{l}$ . The fallypride purification column was prepared using the same technique used to form the concentration column, inserting a triple row of square PDMS pillars with 40  $\mu\text{m}$  gap near the outlet of microchannel. Reverse phase  $\text{C}_{18}$  (Fisher Scientific, Acros Organics, size 40-63  $\mu\text{m}$ ), suspended in pure ethanol, was introduced through the inlet of the purification microchannel, and was trapped inside to form the desired column. The dimension of the fallypride purification column was 4.8 cm in length, 4 mm in width and 60  $\mu\text{m}$  in height, allowing 7.2  $\mu\text{l}$  (~20 mg) reverse phase  $\text{C}_{18}$  microparticles to be packed inside. The purification column was activated before the experiment by flowing 0.5 ml DI water through it. Off-chip mechanical valves (Upchurch Valves, V-100D) were used to control the transit of reagents among these three modules. A syringe pump (New Era Pump Systems, NE-300) was

used to control flow of the various reagents. A hot plate (IKA, Control-VISC) placed under the microfluidic chip was used to heat the entire device during solvent evaporation and fluorination reaction steps.

[<sup>18</sup>F]Fluoride ion was obtained by cyclotron (GE Healthcare PETtrace 880) irradiation of [<sup>18</sup>O]-enriched water. Anhydrous acetonitrile (MeCN, 99.8%), anhydrous methanol (MeOH, 99.8%) were purchased from Sigma Aldrich and used without further purification. Fallypride precursor was purchased from ABX Chemicals (Dresden, Germany). K<sub>222</sub>/K<sub>2</sub>CO<sub>3</sub> eluting solutions was prepared in the mixture of 250 mg of K<sub>222</sub> dissolved in 6 ml acetonitrile and 140 mg of K<sub>2</sub>CO<sub>3</sub> in DI water.

A Hitachi HPLC (LaChrom Elite, Pump L-2130) equipped with a wavelength UV detector (L-2400) and inline radiation detector (Inline Carroll & Ramsey) was used for radiochemical analysis. A Phenomenex C<sub>18</sub> column (Luna 5µm C18(2) 100Å LC Column 250 x 4.6mm) was utilized and the flow rate of isocratic mobile phase of 55% ethanol and 45% 15mM Na<sub>2</sub>PO<sub>4</sub> buffer was 0.9 ml/min. Total radioactivity was measured using calibrated dose calibrators (Capintec, CRC-25PET).



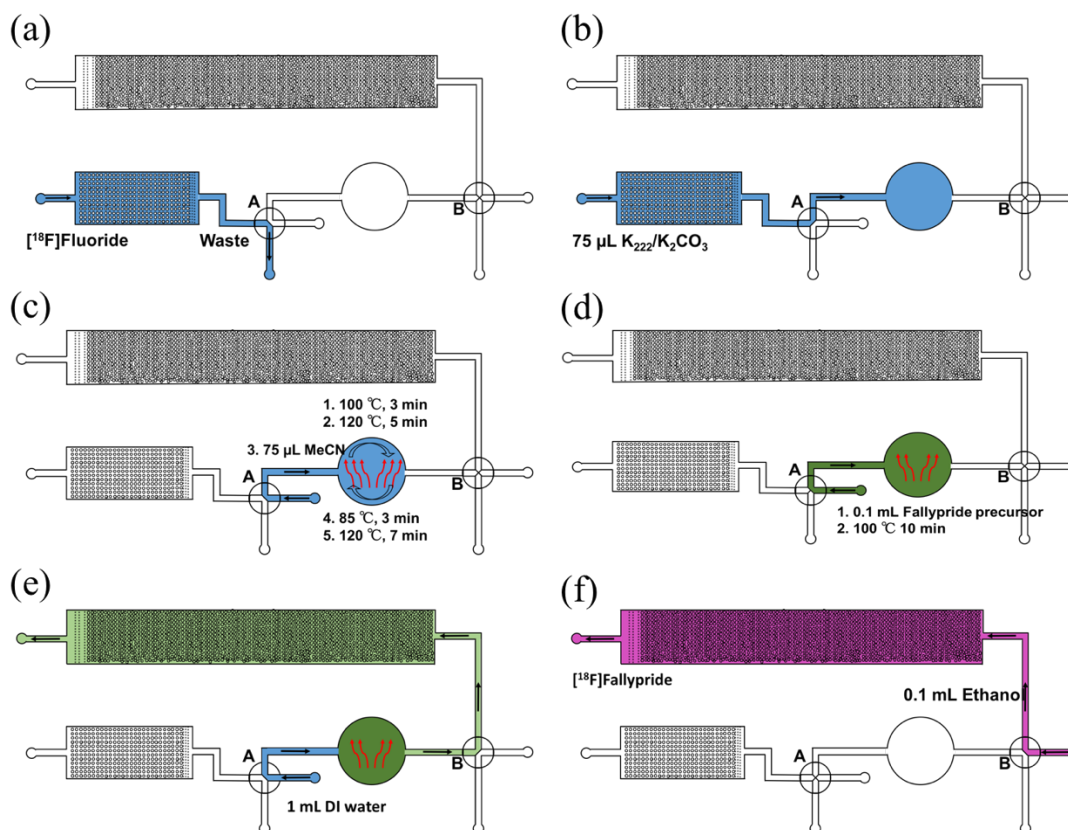


**Figure 5.3** Schematic representation of the steps used for the production of  $[^{18}\text{F}]$ fallypride on our integrated microfluidic chip. The six steps shown are: (a) concentrate  $[^{18}\text{F}]$ fluoride using anion-exchange column, (b) release trapped  $[^{18}\text{F}]$ fluoride off the column and transfer into reaction cavity, (c) evaporate to achieve an anhydrous environment by heating and  $\text{N}_2$  drying, (d)  $[^{18}\text{F}]$ fallypride fluorination, (e) isolate undesired products using purification column, (f) collect purified  $[^{18}\text{F}]$ fallypride off chip.

Figure 5.3 illustrates the steps required for fallypride radiosynthesis on our microfluidic chip. Radioactive  $[^{18}\text{F}]$ fluoride in  $[^{18}\text{O}]$ -enriched water was obtained immediately after cyclotron irradiation. Unless noted elsewhere, the amount of radioactivity used in our experiments was  $\sim 30\text{mCi}$  in  $\sim 0.1\text{ ml}$  irradiated target wash water. In Figure 5.3a, the  $[^{18}\text{F}]$ fluoride mixture was introduced into the inlet of the on-chip concentration column using the syringe pump with a  $30\ \mu\text{l}/\text{min}$  loading rate followed by  $0.1\text{ ml}$  of air at a loading rate of  $50\ \mu\text{l}/\text{min}$  allowing all liquid to be pushed through the tubing connection and column. The liquid coming out from the

concentration column was collected in a glass vial, and typically contained a negligible amount of radioactivity (less than 2  $\mu\text{Ci}$ ). The radioactivity of the initial [ $^{18}\text{F}$ ]fluoride loading, captured inside the concentration column, and the [ $^{18}\text{F}$ ]fluoride residue left in the syringe were measured separately via a dose calibrator. To measure the amount of radioactivity concentrated on chip, we placed the whole chip in a dose calibrator. The efficiency of the concentration column was calculated after accounting for the decay of the radioisotope.

To release the captured [ $^{18}\text{F}$ ]fluoride as shown in Figure 5.3b, 75  $\mu\text{l}$  of  $\text{K}_{222}/\text{K}_2\text{CO}_3$  eluting solution was injected into the inlet of the concentration column at a 30  $\mu\text{l}/\text{min}$  loading rate. At the same time, the mechanical valve A, connected between the concentration column and batch reactor, was set to direct the released reagent into the reaction cavity. Another 0.1 ml air was injected from the inlet of the concentration column to push all the remaining liquid into the reaction cavity. Because the fluorination reaction requires anhydrous conditions shown in Figure 5.3c, the microfluidic chip was first placed on a hot plate at 100  $^\circ\text{C}$  for 3 minutes and then at 120  $^\circ\text{C}$  for 5 minutes. The heated water inside the reaction cavity evaporated through the 1.5 mm hole on the top. The microfluidic chip was then removed from the hot plate for 2 minutes, allowing the entire chip to cool down below the boiling point of acetonitrile. To completely remove residual moisture inside the reaction cavity, 75  $\mu\text{l}$  anhydrous acetonitrile was loaded from the inlet of the reaction cavity and the entire chip was placed on another hotplate at 85  $^\circ\text{C}$  for 3 minutes, and then at 120  $^\circ\text{C}$  for 7 minutes. Constant  $\text{N}_2$  flow at 0.2 psi was applied through the inlet of the reaction cavity to facilitate the removal of residual moisture during the entire evaporation process. After these drying steps, solid residue was observed at the bottom of the cavity (Figure 5.4). The on-chip radioactivity after evaporation was measured and the loss of radioactivity was less than 5%.

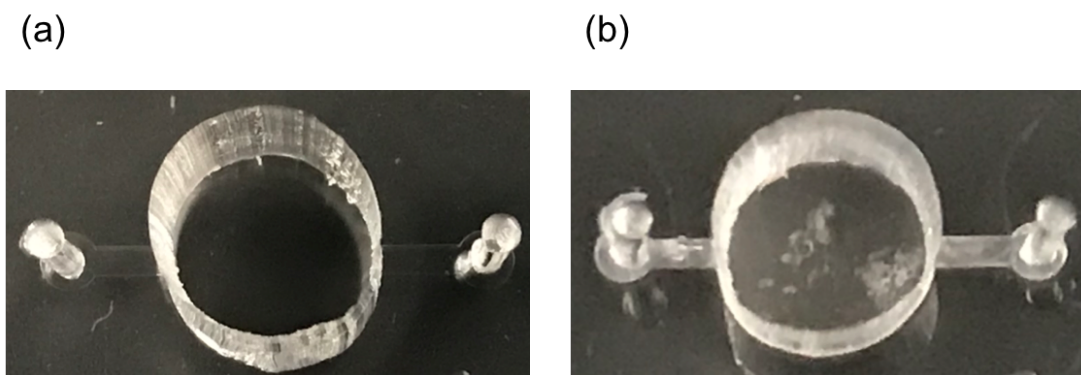


**Figure 5. 4** Photograph of on-chip reaction cavity with no reagent inside (a) and after water evaporation (b).

After achieving the anhydrous conditions necessary for fallypride fluorination, 0.1 ml dimethyl sulfoxide (DMSO) containing fallypride precursor (3 mg), vortex-mixed for 30 minutes in advance, was injected from the inlet of the reaction cavity and the cavity was immediately sealed by screwing in a male nut (Fisher Scientific) into the NanoPort, minimizing the loss of radioactivity during the fluorination process. As shown in Figure 5.3d, the chip was heated at 100 °C for 10 minutes to produce the radioactive fallypride. The successful synthesis of [ $^{18}\text{F}$ ]fallypride was validated via radio-HPLC analysis, the radioactive peak eluting at 11-12 minutes matching the reference standard.

To obtain chemically pure [ $^{18}\text{F}$ ]fallypride suitable for PET imaging, the crude production material was purified using a column containing monodisperse  $\text{C}_{18}$  stationary phase. Before transferring all liquid through the on-chip purification column, 0.1 ml DI water was loaded from the inlet of the purification column to fully rinse the  $\text{C}_{18}$  gel. Subsequently, valve A and valve B were set in the fashion shown in Figure 5.3e to allow flow from the reaction cavity to the purification column. The flow rate produced by the syringe pump was 50  $\mu\text{l}/\text{min}$ . The tight seal

of the reaction cavity provided by the male nut allowed the synthesized compound to be injected into the purification column without leakage. Undesired compounds, including unreacted fallypride precursor, any remaining [ $^{18}\text{F}$ ]fluoride, and various by-products were thereby pushed off-chip, only leaving the desired [ $^{18}\text{F}$ ]fallypride trapped on-chip. Next, another 0.1 ml DI water was passed over the purification column to totally remove unreacted [ $^{18}\text{F}$ ]fluoride ion, which would lower the overall radiochemical purity and confound imaging procedures. Finally, trapped [ $^{18}\text{F}$ ]fallypride was eluted off of the chip using 0.1 ml pure ethanol and collected in a glass vial (Figure 5.3f).

### 5.3 Results and Discussion

To synthesize [ $^{18}\text{F}$ ]fallypride or other radiotracers with a microfluidic chip, the first critical step is to concentrate [ $^{18}\text{F}$ ]fluoride that is provided as a diluted solution in [ $^{18}\text{O}$ ]-enriched water. We employed PDMS pillars to form physical barriers near the end of the microchannel, thus trapping desired anion exchange microparticles inside the concentration column. Figure 5.2c shows an optical image of anion exchange beads packed inside the concentration column. Experimental results (Table S1) suggested that the on-chip concentration column can accomplish efficient enrichment of a sufficient quantity of [ $^{18}\text{F}$ ]fluoride with minimal radioactivity loss, comparable or better than performance achieved with a commonly used purification cartridge (Waters Sep-Pak QMA).

Volume of Beads ( $\mu\text{L}$ )	Initial syringe radioactivity (mCi)	Final syringe radioactivity (mCi)	Waste vial radioactivity (mCi)	Radioactivity trapped on chip (mCi)	Efficiency
0.62	10.3	0.6	0.9	8.93	90.1%
0.62	8.7	0.6	0.7	7.5	92.2%
0.62	35.8	1.8	12.6	21.5	65%
0.62	39.1	1.5	14.3	20.9	59.7%
3	95.7	0.34	0.01	93.0	97.7%
3	128.6	4.8	0.1	123.0	95.9%

**Table 5. 1** The relationship between the volume of anion exchange beads inside the concentration column and the radioactivity trapped on the microfluidic chip. All listed values are decay-corrected to the time point of initial radioactivity in the syringe.

As expected, the maximum quantity of [ $^{18}\text{F}$ ]fluoride that could be captured by the concentration column was related to the volume of anion exchange beads packed inside the microchannel. Considering that the goal of our microfluidic chip is to synthesize multiple doses of radiotracer sufficient for human imaging, the on-chip concentration module, must be capable of capturing radioactivity in the range of 100 mCi (3700 MBq). To determine the relationship between the volume of anion exchange resins and the captured radioisotope, we fabricated several versions of ion exchange columns with varying dimensions. Raw [ $^{18}\text{F}$ ]fluoride with radioactivity values as high as 130 mCi (4810 MBq) was then loaded into each column to evaluate the trapping efficiency and determine the optimal dimension. Table S1 summarizes the results of these experiments. It turned out that 3  $\mu\text{L}$  (~10 mg) of anion exchange resin was able to capture over 100 mCi [ $^{18}\text{F}$ ]fluoride with the efficiency  $98 \pm 1\%$  (n=5) over a loading period of ~6 minutes. However, a reduced timespan may be achieved with additional optimization of column geometry (i.e., wider microchannel) to allow higher reagent loading rate.

To release the captured [ $^{18}\text{F}$ ]fluoride from the concentration column, 75  $\mu\text{L}$  of  $\text{K}_{222}/\text{K}_2\text{CO}_3$  solution, was introduced into the anion exchange column channel, after which the released

solution was directed to the reaction cavity. During reagent transfer process, valve A and valve B was set in the fashion shown in Figure 5.2b to allow minimal liquid stuck in tubing connection. In our attempt to reduce the overall synthesis time the volume of  $K_{222}/K_2CO_3$  eluting solution required to fully release all  $[^{18}F]$ fluoride off the concentration column was optimized. In this system, a large portion of the production time is devoted to achieving a completely anhydrous state prior to the synthesis reaction, and thus optimizing the volume of eluting solution helps promote the overall production efficiency and minimizes the decay of radioisotope. We compared the release efficiency with various volumes and the results indicated that 75  $\mu$ l of the  $K_{222}/K_2CO_3$  was the optimal amount for releasing  $[^{18}F]$ fluoride with radioactivity loss less than 5% (Table S2).

<b>Volume of <math>K_2CO_3/K_{222}</math> (<math>\mu</math>l)</b>	<b>On-chip radioactivity (mCi)</b>	<b>Released radioactivity (mCi)</b>	<b>radioactivity left on-chip (mCi)</b>	<b>Efficiency</b>
50	7.5	4.8	1.7	74%
50	4.6	3.58	0.94	77%
75	4.25	3.84	0.23	95%
100	6.2	5.48	0.1	98%

**Table 5. 2** The relationship between the volume of  $K_{222}/K_2CO_3$  used for releasing trapped  $[^{18}F]$ fluoride off the concentration column and the releasing efficiency. The efficiency is calculated accounting for the decay of the radionuclide over time.

To achieve anhydrous conditions inside the reaction cavity, the entire chip was placed on a hotplate and a temperature gradient (100 °C for 3 minutes and 120 °C for 5 minutes) was set, instead of direct heating at extremely high temperature, to avoid violent boiling, which could result in the liquid splashing out from the upper hole. A slow nitrogen flow was introduced via the inlet of the reaction cavity to facilitate the evaporation process. After the first round of heating, azeotropic distillation was employed by injecting 75  $\mu$ l anhydrous MeCN into the

reaction cavity to completely remove any remaining moisture. In conventional macroscopic radiotracer production, 2-3 cycles of azeotropic distillation are typically performed to guarantee an anhydrous environment. In contrast, using our microfluidic platform, only one cycle of azeotropic distillation is sufficient to enable the subsequent nucleophilic substitution reactions, thus shortening the required production timeframe. Figure 5.4 shows an optical image of the solid salt deposited on the bottom of the reaction cavity after evaporation.

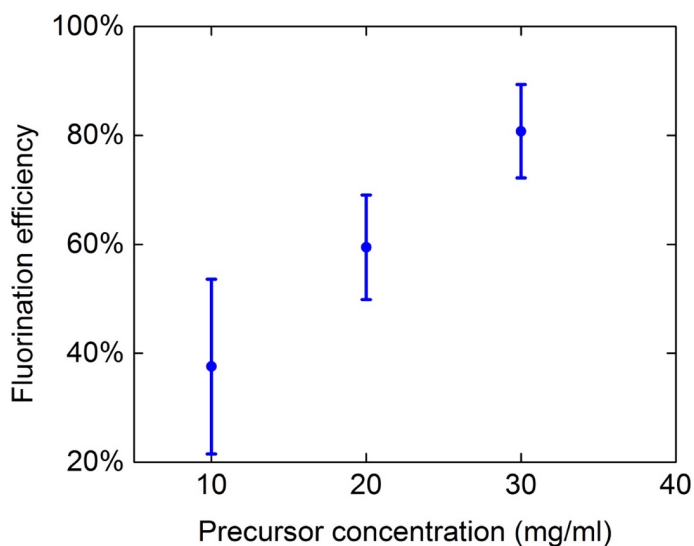


**Figure 5. 5** The relationship between precursor concentration and fluorination efficiency.

The fluorination reaction is performed after introducing the fallypride precursor, dissolved in a polar aprotic solvent, into the reaction cavity containing the concentrated, dried fluoride-kryptofix complex. Instead of employing a low-boiling-point solvent, such as acetonitrile, the fallypride precursor was dissolved in DMSO and loaded into the reaction cavity. Though acetonitrile has been widely used in clinical production and has the benefit of being easily removed later, the required temperature for nucleophilic substitution reactions with [ $^{18}\text{F}$ ]fluoride

(usually around 100 °C), exceeds the boiling point of acetonitrile, which would increase the pressure inside the sealed cavity and possibly lead to leakage. Employing the high boiling point solvent DMSO avoids these issues. Based on a report by Javed et al., the concentration of fallypride precursor plays a significant role in final crude radiochemical yield in a batch microfluidic reactor.<sup>50</sup> To optimize the yield of [<sup>18</sup>F]fallypride in our microfluidic chip, we further investigated the relationship between the concentration of fallypride precursor and the overall conversion efficiency. Similar to previous reports, we observe a rise of fluorination efficiency as the concentration of fallypride precursor increases (Figure 5.5). The successful synthesis of [<sup>18</sup>F]fallypride was confirmed via HPLC analysis (Figure 5.6a). The result indicated that the labeling efficiency during fluorination process was ~ 87%, higher than what can be typically obtained using conventional automated methodologies.<sup>196</sup>

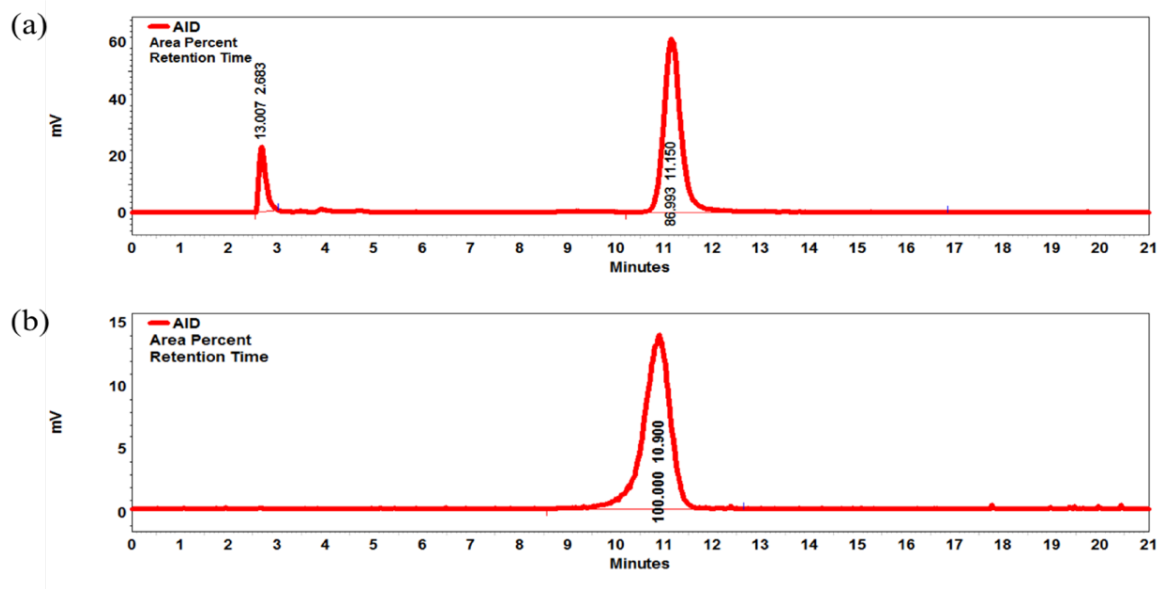


**Figure 5. 6** (a) Crude radio-HPLC of [<sup>18</sup>F]fallypride synthesized inside the reaction cavity. (b) Radio-HPLC of [<sup>18</sup>F]fallypride eluted from the on-chip purification column.



After the fluorination reaction, the product exists in a solution containing unwanted quantities of unreacted [ $^{18}\text{F}$ ]fluoride,  $\text{K}_{222}$ , and other undesired byproducts. Thus, the crude [ $^{18}\text{F}$ ]fallypride mixture must be purified. We accomplish this using an integrated on-chip purification column. The purification column was fabricated in a manner identical to the concentration column. Figure 5.2d shows an optical image of reverse phase  $\text{C}_{18}$  particles packed inside a microchannel forming the purification column. After the fluorination reaction, the hot microfluidic chip was allowed to cool down to approximately room temperature. Meanwhile, 0.1 ml DI water was loaded through the purification column to fully activate reverse phase  $\text{C}_{18}$ . Next, 1 ml DI water was injected at the inlet of the reaction cavity, pushing the reacted solution (with the products in DMSO) through the purification column. To minimize any potential loss of [ $^{18}\text{F}$ ]fallypride, the volume ratio of DMSO to water was tuned to 1:10 such that it was able to carry all crude radiochemical mixture in the reaction cavity but didn't wash the captured [ $^{18}\text{F}$ ]fallypride off the on-chip purification column. The overall time needed for the purification step was  $\sim 20$  minutes. HPLC analysis of the outlet waste indicated negligible [ $^{18}\text{F}$ ]fallypride loss during this step (Fig. S2). Finally, the trapped [ $^{18}\text{F}$ ]fallypride was released by injecting 0.1 ml pure ethanol into the inlet of purification column. Fig. 5(b) shows radio-HPLC analysis of the eluted [ $^{18}\text{F}$ ]fallypride, which exhibited 100% radiochemical purity.

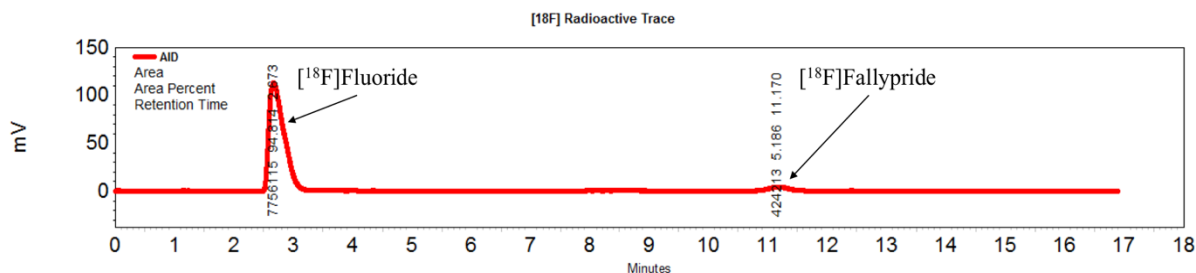


**Figure 5. 7** Radio-HPLC analysis of the waste mixture passed through the  $\text{C}_{18}$  column. This injection was taken using the mixture solution flowing out from the purification column after labelling reaction. 95% [ $^{18}\text{F}$ ]Fluoride was washed off the purification column, and only 5% [ $^{18}\text{F}$ ]fallypride was lost at this step.

The overall radiochemical yield (RCY) ( $10\pm 3\%$ ,  $n=5$ ) is calculated as the ratio of the decay-corrected radioactivity of the resulting [ $^{18}\text{F}$ ]fallypride released off the chip, divided by the initial radioactivity of [ $^{18}\text{F}$ ]fluoride loaded into the microfluidic chip (trapped by the on-chip concentration column). The radioactivity of the [ $^{18}\text{F}$ ]fluoride loaded into the microfluidic chip was measured by placing the whole chip in a dose calibrator. The average radioactivity used for those productions was  $\sim 50$  mCi and the volume of anion exchange beads and reverse phase  $\text{C}_{18}$  was  $3.2\ \mu\text{l}$  and  $7.2\ \mu\text{l}$ , respectively. The whole process was completed in approximately 60 minutes starting from the loading of [ $^{18}\text{F}$ ]fluoride to the collecting of purified [ $^{18}\text{F}$ ]fallypride, which could likely be further shortened using automated external valves and programmable syringe pumps. As reported by Elizatov, PDMS may react with [ $^{18}\text{F}$ ]fluoride ions, which could reduce the overall radiochemical yield.<sup>45</sup> Future efforts will focus on reducing this loss by either coating the inner walls of the channels with an inert layer<sup>197,198</sup> or modifying the chip fabrication material.<sup>54,199</sup>

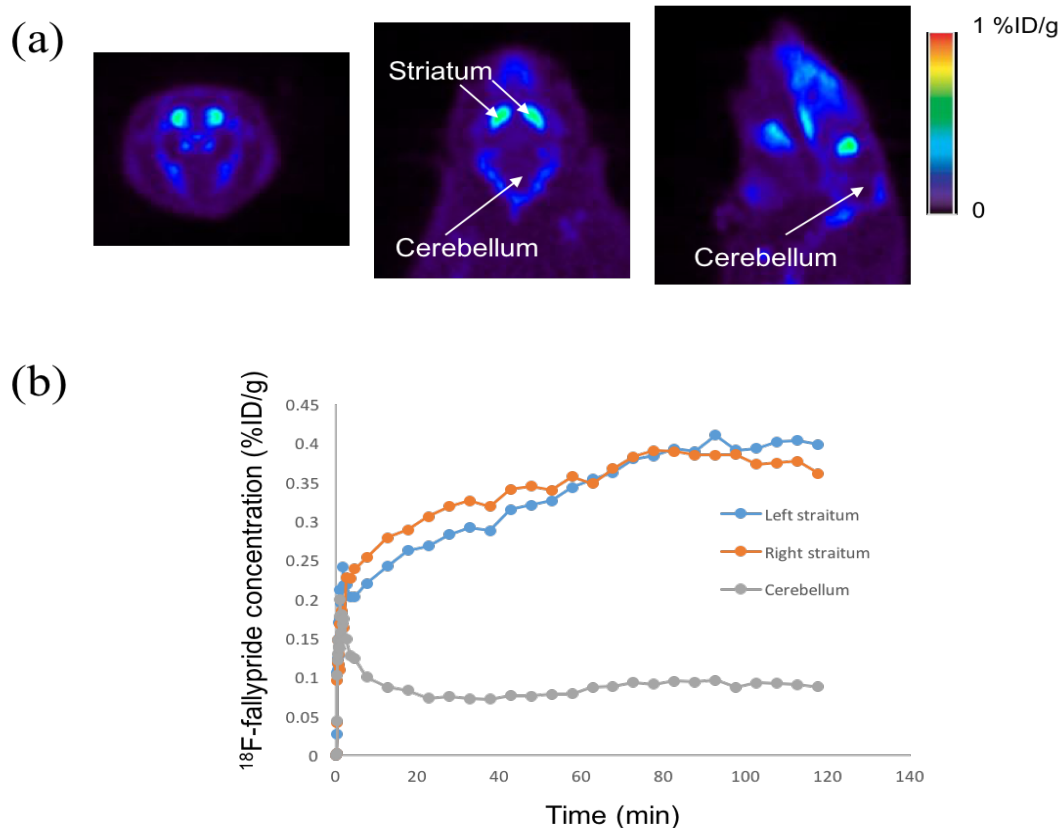


**Figure 5. 8** (a) PET image of rat brain using [ $^{18}\text{F}$ ]fallypride produced in a microfluidic chip. (b) The variation of [ $^{18}\text{F}$ ]fallypride concentration imaged in the microPET for 2 hours.

To further verify the utility of the resulting [ $^{18}\text{F}$ ]fallypride, we produced (using our integrated microfluidic chip) a dose of 300  $\mu\text{Ci}$  with 19.55  $\text{Ci}/\mu\text{mol}$  (723.35  $\text{GBq}/\mu\text{mol}$ ) of specific activity and 98.62% of radiochemical purity, and obtained PET data from a rat brain. The time point used to calculate the specific activity was at the end of production, namely the time when the purified [ $^{18}\text{F}$ ]fallypride was retrieved from chip. The rat was brought to the imaging lab to habituate 3 hours prior to imaging. 0.1 ml purified [ $^{18}\text{F}$ ]fallypride was flowed through a 0.45  $\mu\text{m}$  filter (Millex-HV) and 0.9 ml saline was added to formulate the PET probe used for rat injection. Fig. 6 shows the resulting PET imaging data. The accumulation and

pharmacokinetics of [<sup>18</sup>F]fallypride were as expected when evaluated in the rat brain.<sup>200</sup> A typical UV spectrum, indicating some observable chemical impurities, is given in Fig. S3. Though the chemical purity has been dramatically improved from the crude product mixture, further purification is needed.

Publication	Starting [ <sup>18</sup> F]fluoride	Fluorination efficiency	Purification method	Dose amount	Specific activity	Overall RCY	Synthesis time	PET imaging
Lu et. al <sup>195</sup>	0.5 - 2.5 mCi	Up to 88%	HPLC	0.5-1.5 mCi	Not reported	Not reported	~50 min	No
Chen et. al <sup>51</sup>	Not reported	65 ± 11% (n = 6)	No	Not reported	19 Ci/μmol	Not reported	~31 min	No
Lebedev et. al <sup>56</sup>	370 mCi	Not reported	HPLC	~27mCi	Not reported	37±5%	~45 min	Human
Our work	~50 mCi	80 ± 8% (n = 4)	On-chip module	~3 mCi	19.55 Ci/μmol	10±3%	~60 min	Rat

**Table 5. 3** Operational performances of our microfluidic platform compared to several reported results based on microfluidic [<sup>18</sup>F]fallypride production. All efficiencies and yields are calculated based on decay-corrected values.

A general performance comparison to previously reported results from other platforms (including information regarding fluorination efficiency, purification method, synthesis time, resulting dose amount, specific activity and overall radiochemical yield) is summarized in Table 1. Our microfluidic platform exhibits comparable performance in terms of fluorination efficiency and specific activity. Further optimization and automation of various operational parameters may increase the overall radiochemical yield and reduce the entire synthesis time.

In terms of disposability, the microfluidic chip may be discarded after each PET tracer production once any residual on-chip radioactivity has decayed to a safe level. Off-chip flow control components, such as pumps and mechanical valves, may be cleaned using ethanol or other appropriate solvents, and are thus reusable. Future work will focus on creating a fully automated heating and fluid flow control system (microcontroller, solenoid valves, remote

control pump system, etc.) that will enable PET probe production runs without the need for operator intervention at every step.

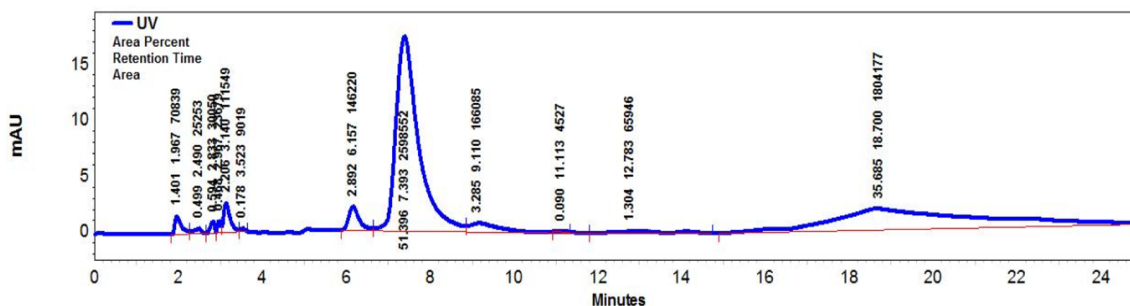


**Figure 5. 9** A typical UV spectrum for the purified [ $^{18}\text{F}$ ]fallypride, showing product peak at 11.11 min. The presence of minor impurities is observed throughout the spectrum.

## 5.4 Conclusion

We have developed a simple, economic and efficient microfluidic platform to aid both radiochemistry research efforts and clinical efforts by rapidly producing ultrapure radioactive fallypride on demand. This highly integrated configuration enables all essential steps needed for [ $^{18}\text{F}$ ]fallypride production without any off-chip treatment, starting from reaction reagents and ending with a purified product. These disposable chips may allow high throughput investigations of novel radiotracer chemistry, as well as the mass-production of established PET tracers. By using this microfluidic device, we envision that clinicians may overcome a significant bottleneck imposed by limited access to an onsite cyclotron, as they could easily utilize delivered radionuclides and produce imaging reagents as needed without relying on centralized facilities. The integration of this microfluidic device within current clinical environments would be a relatively straightforward task, and serve as a solution to the high cost of standard radiopharmaceutical production. Moreover, the methodology used for constructing the

microfluidic system is simple and the chip can easily be customized by replacing the packing materials inside each column, making it suitable for production of other PET tracers.

## Chapter 6 High-yielding Radiosynthesis of $^{68}\text{Ga}$ -PSMA-11 Using a Low-cost Microfluidic Device

### 6.1 Introduction

Positron emission tomography (PET) is a powerful imaging technique widely utilized in healthcare for disease diagnosis and staging; numerous clinical applications include oncology, neurology, cardiology and beyond. PET imaging requires the administration of biologically active tracers, whose accumulation reflects specific underlying biological processes associated with health and disease.<sup>1</sup> Although hundreds of distinct PET tracers have been reported for many potential indications to date, one particular tracer, [ $^{18}\text{F}$ ]fluorodeoxyglucose (FDG), is utilized in more than 90% use of clinical PET scans.<sup>2</sup> Factors that contribute to the lack of PET tracer availability in both the commercial and academic settings include extremely high infrastructure and personnel costs associated with production. Cost associated with facility operational rise dramatically with the number of unique PET tracers produced; commercial distribution of PET tracers tends to favor centralized models, where large batches of a small number of unique tracers are produced on a regular basis. This setting financially favors tracers with large distribution potential on a per batch basis (*i.e.*,  $^{18}\text{F}$ -FDG; one batch, many doses), whereas PET tracers produced on a single batch-dose basis tend to be prohibitively expensive. From both economic and logistical standpoints, the current model of distribution is not capable of supplying the breadth of PET tracers needed to advance the field of molecular imaging to its fullest potential. For PET to realize its fullest impact in the era of precision medicine, tracer production must become capable of supplying single patient-dose batches of a wide variety of unique PET tracers, on demand, and in an economically feasible way.

Microfluidics has been proposed as a strategy to both reduce the costs associated with PET tracer production and expand the breadth of tracers routinely available.<sup>3,4</sup> Compared to routine macroscale automated synthesis, microfluidic platforms exhibit many advantages such as the ability to work with small liquid volumes, limited consumable utilization, rapid reaction kinetics, reduced radiation shielding requirements, and small footprints; each of these factors are major drivers of costs in traditional PET tracer production.<sup>5</sup> To date, several microfluidic systems for tracer production have been reported and include capillary-based microfluidic synthesis platforms and lab-on-a-chip devices.<sup>6-12</sup> In general, these devices either illustrate improved performance on one particular step (*i.e.*, radioisotope concentration or radiochemical incorporation) or improved radiochemical yield. However, many of the prior reported designs remain costly to produce and difficult to operate, and also do not exhibit the level of integration necessary to perform the entire tracer generation process on-chip; instead, they require many steps (*i.e.*, pre-concentration, purification, etc.) to be performed off-chip, leading to unwanted loss of radioactivity and lower efficiency. In addition, most of the products resulting from such devices are not suitable to be directly used for human scanning; additional processing is required. Consequently, it is critical to explore advanced integrated microfluidic platforms such that PET imaging probes resulting from a device exhibit both high radiochemical and chemical purity, enabling compliance with rigorous quality control (QC) testing. We recently reported an integrated microfluidic device capable of pre-concentrating [<sup>18</sup>F] at levels appropriate for human dosages, synthesizing [<sup>18</sup>F]fallypride with high labelling efficiency, and purifying the reaction product on-chip so as to yield a radiochemically pure quantity of tracer sufficient for imaging purposes. We thereby demonstrated a cost effective microfluidic platform that enables synthesis of radiopharmaceuticals at a dose-on-demand level where the isolated products, after



formulation, are qualified for direct injection. In this work, we take the next step to demonstrate that this concept is flexible enough to be used for a different PET tracer, employing a different radionuclide as well as different reaction chemistries requiring additional fluidic complexity. This highlights the flexibility and wide applicability of this approach for integrated, on-demand production of PET tracers.

Prostate cancer (PC) is the second leading cause of deaths among adult males worldwide and the fourth most common cancer overall.<sup>13</sup> Because of its high expression on the surface of prostate cancer cells, prostate-specific membrane antigen (PSMA) has been identified as a target for PET molecular imaging and for targeted radioligand therapy. For diagnostic imaging of PC, one popular radionuclide is gallium-68 due to several intrinsic advantages. First, it has a physical half-life of 68 min, which is suitable to be applied in macroscale synthesis systems. Second, instead of relying on an on-site cyclotron, <sup>68</sup>Ga can be conveniently obtained from a commercially available <sup>68</sup>Ge/<sup>68</sup>Ga generator. Moreover, recent studies have suggested that <sup>68</sup>Ga-PSMA likely possesses more sensitivity than <sup>18</sup>F-fluoromethylcholine or <sup>11</sup>C-choline for evaluation of recurrent prostate cancer.<sup>14,15</sup> As a consequence, there has been a growing demand for the use of <sup>68</sup>Ga-labelled PSMA for imaging of PC.

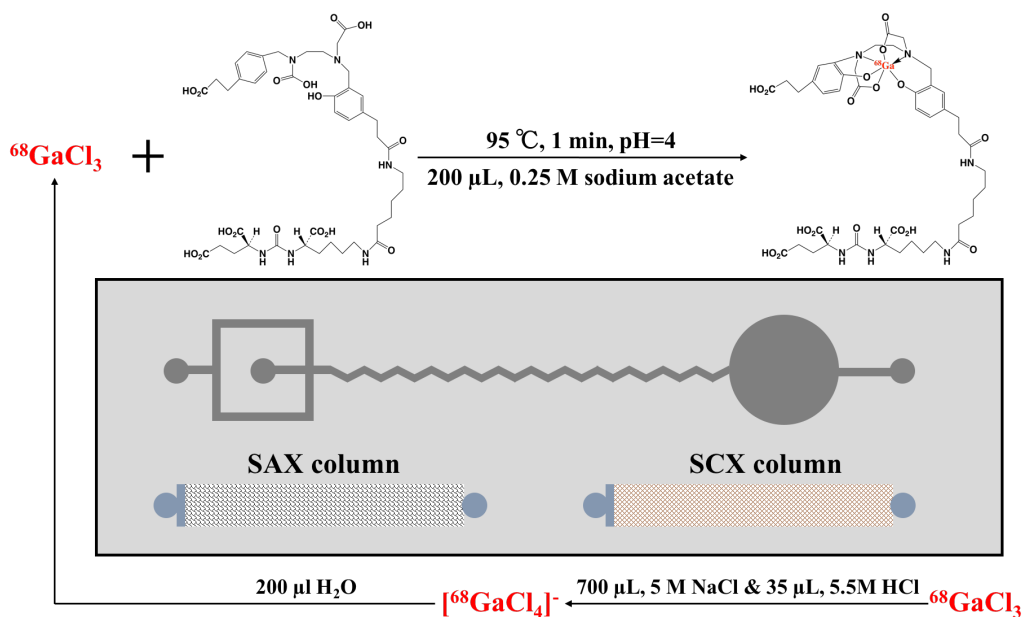


**Figure 6. 1** Schematic representation of a chip designed for the synthesis of  $^{68}\text{Ga}$ -PSMA, including an SCX column, SAX column, passive mixing module and reactor for the labelling reaction.

In this study, we report the development of a miniaturized device that enables radiosynthesis of  $^{68}\text{Ga}$ -PSMA-11 at very low cost and with high yield. Our microfluidic system consists of several miniaturized modules, which can be used to achieve all critical steps such as radioisotope concentration, passive on-chip mixing and a heated labeling reaction without the need of any off-chip manipulation. By starting with a full elution from the  $^{68}\text{Ge}/^{68}\text{Ga}$  generator, the microfluidic device can generate several doses of  $^{68}\text{Ga}$ -PSMA that can be subsequently qualified for direct administration to patients. The isolated final product solution is thoroughly examined following standard quality control (QC) procedures to ensure full compliance with Good Manufacturing Practice (GMP) guidelines. Towards the dose-on-demand concept, we envision this reported work would aid in the expansion and availability of PET technology by enabling cost-effective production of various radiopharmaceuticals.

## 6.2 Materials and Methods

Materials and facilities used for microfluidic chip fabrication were described in our previous work.<sup>211</sup> Briefly, soft lithography was employed to pattern channels in polydimethylsiloxane (PDMS), which was then bonded to a glass slide after exposing to oxygen plasma. Off-chip mechanical valves (Upchurch Valves, V-100D) were used to control the transit of reagents between modules. Syringe pumps (New Era Pump System, NE-300) was used to load solution at controlled flow rate. A hot plate (IKA, Control-VISC) was used to heat the entire microfluidic device during on-chip mixing and labeling reaction.

As schematically illustrated in Figure 6.1, the microfluidic chip was constructed with three key components: an on-chip strong cation exchange (SCX) column, an on-chip strong anion exchange (SAX) column, and a passive in-plane mixing/reaction module. Specifically, it is designed to sequentially complete steps: concentrate gallium-68 delivered from the gallium-68 generator, mix eluted gallium-68 with PSMA-11 precursor, and perform heat-aided labelling reaction.

The dimensions of the on-chip SCX/SAX column were as follows: 5 mm in width, 20 mm in length, and 100  $\mu\text{m}$  in height. Maxi-Clean SCX/SAX resins (GRACE, 600 mg, particle size 50  $\mu\text{m}$ ) were suspended in ethanol (5 w/v%) and loaded into each column using syringe pumps (loading rate: 100  $\mu\text{l}/\text{min}$ ). All resins can be trapped by rows of PDMS obstructions, thus allowing for the construction of columns with demanded functionalities. The in-plane passive mixing module adopted a flow-focusing geometry at the entrance. The dimension of zigzag mixing channel was 500  $\mu\text{m}$  in width, 34 mm in length and 100  $\mu\text{m}$  in height. In addition, the width and height of rhombus-shaped obstructions were 50  $\mu\text{m}$  and 100  $\mu\text{m}$ , respectively. The

sizes of all of mixers were equal. The on-chip reaction cavity was fabricated using an 8-mm-diameter punch (Ted Pella) and a 1-mm thick PDMS membrane was aligned and plasma bonded on top of the reactor, allowing for maximum volume of 500  $\mu\text{l}$ .

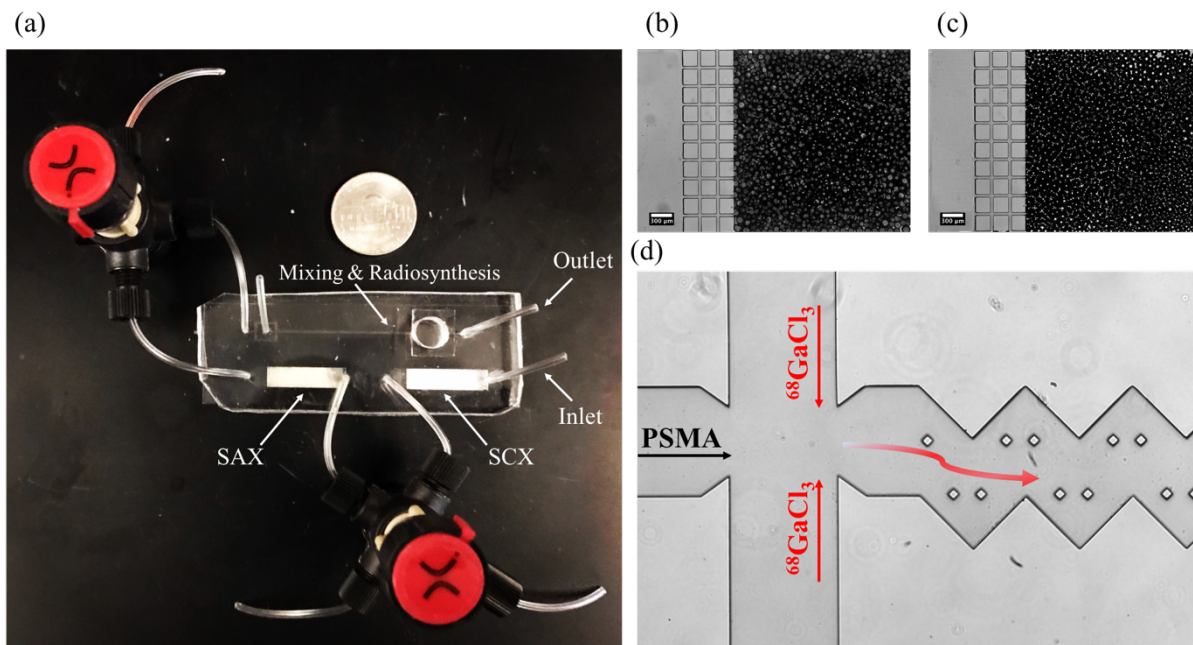


**Figure 6. 2** Photographs of the fabricated microfluidic device for the radiosynthesis of  $^{68}\text{Ga}$ -PSMA-11 (a), SCX (b) and SAX (c) resins trapped inside microchannels, and the entrance of mixing module (d) with diamond-shape obstructions inserted throughout the zigzag microchannel.

All other reagents were of analytical grade, and purchased from commercial source and used as received. For all experiments, gallium-68 was obtained from a  $^{68}\text{Ge}/^{68}\text{Ga}$ -generator (ITG, Munich Germany) that was eluted using sterile, GMP certificated 0.05 M HCl solution. The amount of radioactivity loaded at the beginning was  $\sim 30$  mCi. The GMP-grade PSMA-11 precursor was purchased from ABX (Dresden, Germany). 0.25 M sodium acetate buffer was injected and fully mixed with PSMA-11 precursor prior to labeling reaction. Resins obtained from Maxi-Clean SCX/SAX (GRACE, 600 mg, particle size 50  $\mu\text{m}$ ) cartridges were used to

form on-chip columns. On-chip SCX and SAX modules were preconditioned using 1 mL 5.5 M HCl, followed by rinsing with 5 mL DI water (18 M $\Omega$ , Milli-Q Integral ultrapure water). Notably, all experiments were performed using facilities with the lowest possible metal content to avoid unfavorable interference with  $^{68}\text{Ga}$ -PSMA labelling reaction.

A Hitachi HPLC (LaChrom Elite, Pump L-2130) equipped with a wavelength UV detector (L-2400, 254 nm) and inline radiation detector (Inline Carroll & Ramsey) was used to evaluate radiochemical purity. A C<sub>18</sub> column (Phenomenex Gemini, particle size 10  $\mu\text{m}$ , 150  $\times$  4.6 mm ) was used. For the mobile phase, acetonitrile (referred as A) mixed with water containing 0.1% trifluoroacetic acid (TFA) (referred as B) was used with gradient as following: 0% A /100% B for 0-2 min, 100% A/ 0% B for 8-10 min. The flow rate was constantly set as 1 mL min<sup>-1</sup>. Moreover, radiochemical purity was also examined by radio thin layer chromatography (TLC) using ITLC (instant TLC) paper strips (Varian). The TLC buffer consisted of a mixture of 70% ethanol and 0.9% saline in 1:3 volume ratio. All experiments that involved radioactivities were performed in a lead-shielded hot cell. The value of radioactivity was measured using a calibrated dose calibrator (Capintec, CRC- 25PET). The radiochemical yields were evaluated as a percentage of total activity of  $^{68}\text{GaCl}_3$  initially delivered from the generator. Unless specified elsewhere, all efficiencies are calculated based on decay-corrected values.

COMSOL Multiphysics was used to carry out numerical simulation of mixing of two streams in the microchannel. Mixture model (transport of diluted species) was used to extract the concentration profile of PSMA-11 precursor throughout the mixing zone. The dispersion of two miscible streams in a laminar-flow channel was driven by the velocity profile of the flow. The initial loading velocities from all three inlets were set to be 100  $\mu\text{l}/\text{min}$ . The initial concentration of PSMA-11 precursors and gallium-68 was set to be 100 and 0, respectively. To

simplify the model, the properties of two streams were defined as incompressible water. The boundary condition for the inner walls of microchannels was set as no slip condition.

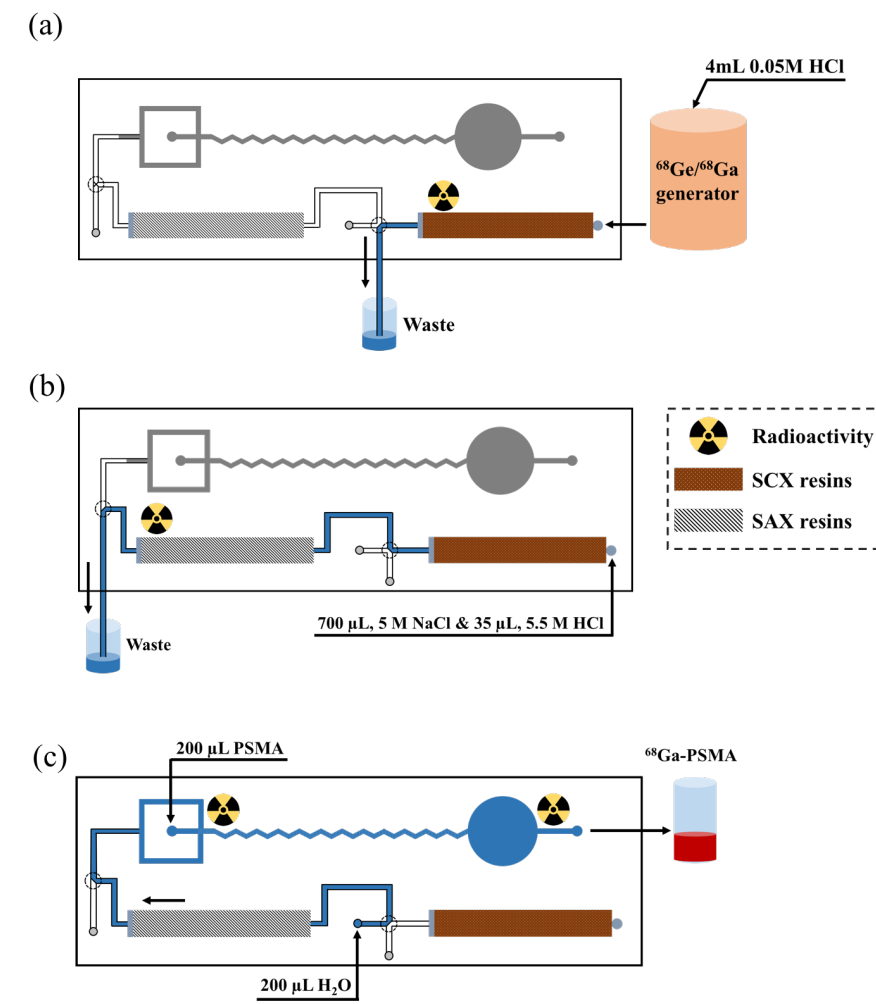


**Figure 6. 3** Schematic diagrams showing the three sequential labelling steps: (a) concentration of generator-obtained  $^{68}\text{Ga}^{3+}$  using an on-chip SCX column, (b)  $^{68}\text{Ga}^{3+}$  elution from the SCX, followed by trapping on the SAX in the form of  $[\text{}^{68}\text{GaCl}_4]^-$ , (c) release  $^{68}\text{Ga}^{3+}$  with water, followed by mixing with PSMA precursor to accomplish the formation of  $^{68}\text{Ga-PSMA}$ .

Figure 6.3 is schematic diagrams that show the three most critical steps of  $^{68}\text{Ga-PSMA}$  production in the microfluidic device. The amount of radioactivity of eluted gallium-68 used in

experiments was  $29.8 \pm 1.15$  mCi in 4 ml 0.05 M HCl elution. First, a full elution of the gallium-68 generator was concentrated by the on-chip SCX column using a syringe pump with an  $800 \mu\text{l min}^{-1}$  loading rate (Figure 6.3a). Then, 0.1 mL air was loaded at the same loading rate to ensure that all liquid completely passed through the column. The isolated waste was collected in a glass vial and the remaining activity was immediately measured. The amount of radioactivity of initial gallium-68 elution for injection, concentrated on the SCX column, and collected in the glass vial was separately measured. Thus, we can map out the correlation between the mass of packed SCX resins and the concentration efficiency.

Second, elution off of the SCX column and onto the SAX column was achieved using a mixture of  $700 \mu\text{l}$  of 5M NaCl and  $35 \mu\text{l}$  of 5.5M HCl. As shown in Figure 6.3b, the solution was injected from the inlet of the SCX column at a loading rate of  $200 \mu\text{l/min}$ . Meanwhile, released solution was controlled by an off-chip valve to slowly pass through the SAX column. Similarly, another 0.1 mL air was injected from the inlet of the SCX to enable all solution to flow sequentially through all columns.

Next, to release trapped isotopes off the on-chip SAX module,  $200 \mu\text{l}$  DI water was injected from the inlet of the SAX column with a loading rate of  $200 \mu\text{l min}^{-1}$  (Figure 6.3c). Simultaneously, the released gallium-68 was mixed with PSMA precursor by flowing through an in-plane mixing channel. The precursor solution was prepared by dissolving  $10 \mu\text{g}$  PSMA-11 ligand in 1 mL of 0.25 M sodium acetate buffer, resulting in a  $10 \mu\text{g/mL}$  concentration. Next, the microfluidic chip was heated at  $95 \text{ }^\circ\text{C}$  on a preheated hot plate to complete labelling reaction. The final volume of synthesized product was  $400 \mu\text{L}$ , which can be further diluted to desired volume for dose administration and imaging injection.

### 6.3 Results and Discussion

The goal of concentration step focuses on effectively capturing majority of  $^{68}\text{Ga}$  from a full elution of the generator (4 mL) using miniaturized microfluidic columns. While numerous methods have already been developed and employed in clinical production, most of these methods primarily rely on the use of commercially available cation/anion exchange cartridges.<sup>212</sup> More importantly, marginal effort has been devoted to determining advantages and disadvantages of these approaches when applied in a microfluidic system.

Previous studies have reported several different strategies that are routinely used for efficient  $^{68}\text{Ga}$  concentration in practical production.<sup>212,213</sup> Since the goal here is to process a full elute of  $^{68}\text{Ga}$  from the original generator, we hence employ a two-step approach that relies on combined effects of cationic concentration and anionic purification. This approach is extremely advantageous when applied in a microfluidic system due to the following aspects: first, it does not involve the addition of buffer solution or organic solvents, thus eliminating the necessity of purification; second, the combination of the SCX and SAX provides the capability to handle a full elution of  $^{68}\text{Ga}$ , demonstrating the capability to produce several imaging doses; third, released  $^{68}\text{Ga}$  in small volume of pure water exhibits high radionuclide and chemical quality, and low acidity, thereby allowing for direct use for a variety of radiolabeling reactions.

Both on-chip SCX and SAX columns were constructed by trapping different functional resins inside microchannels based on previously reported strategy.<sup>211</sup> Figure 6.2b and 6.2c show optical images of SCX and SAX resins densely packed by the end of microchannels. To examine the performance of on-chip columns, we carried out trapping and releasing trials separately on each column. Based on the measured radioactivity using a dose calibrator, the radioactivity concentration efficiency (RCE) and radioactivity release efficiency (RRE) was determined by the



following expression.

$$\text{RCE} = \frac{\text{On - chip trapped radioactivity}}{\text{Initially loaded radioactivity}}$$

$$\text{RRE} = \frac{\text{Released radioactivity}}{\text{On - chip trapped radioactivity}}$$

Additionally, several operating parameters including mass of loaded resins, solution loading rate, and volume of releasing buffer were comprehensively studied. Since the underlying mechanism for  $^{68}\text{Ga}$  concentration relies on the fact that  $^{68}\text{Ga}^{3+}$  eluted off the generator should be absorbed on the surface of silica-based SCX resins, it is thus critical to determine the correlation between mass of loaded resins and concentration efficiency. Rigorous testing revealed that 8 mg of the SCX resins (RCE=96%, n=5) and 10 mg of the SAX resins (RCE=91%, n=5) were required to achieve efficient trapping performance over a loading duration of 5 min.

To release pre-trapped  $^{68}\text{Ga}^{3+}$  off the SCX column, we employed a method described by Mueller et al. where a concentrated NaCl solution containing a very low amount of HCl was used to convert the cationic  $^{68}\text{Ga}^{3+}$  to the anionic  $[\text{}^{68}\text{GaCl}_4]^-$ .<sup>214</sup> As illustrated in Figure 6.3b, elution released off the SCX column was immediately directed to pass through the SAX column, where  $[\text{}^{68}\text{GaCl}_4]^-$  can be absorbed by SAX resins. Hence, it is critical to optimize elution solution to enable both efficient desorption of  $^{68}\text{Ga}^{3+}$  and efficient adsorption of  $[\text{}^{68}\text{GaCl}_4]^-$ . By adjusting the volume ratio of 5.5 M HCl relative to 5 M NaCl, we found that an elute consisting of 700  $\mu\text{L}$  of 5M NaCl and 35  $\mu\text{L}$  of 5.5M HCl enabled the best performance (SCX RRE =90.8%, n=5 and SAX RCE=89.5%, n=5) (Figure 6.4). As the solution was slowly loaded through the SAX column, the excess of HCl can be directly removed from the microfluidic chip. After eluting with 200  $\mu\text{L}$  pure water, the collected isotope, now in the form of  $^{68}\text{Ga}^{3+}$ , exhibited a high chemical and radiochemical purity.

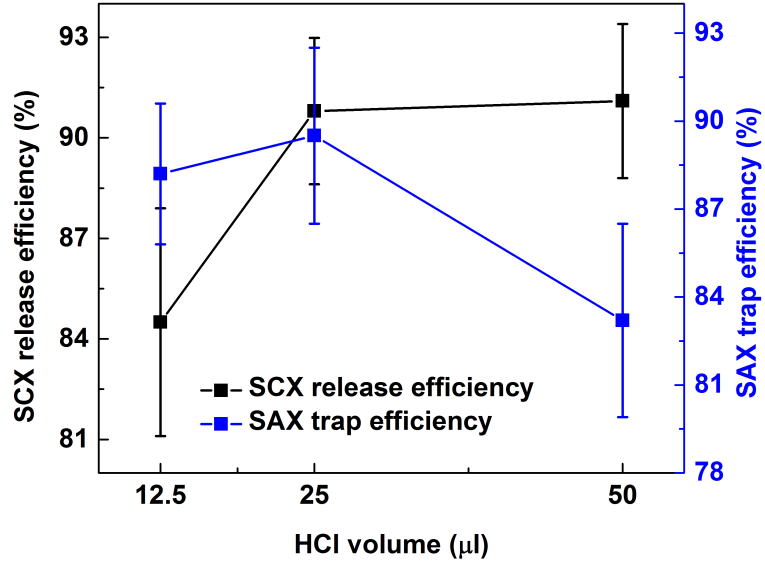


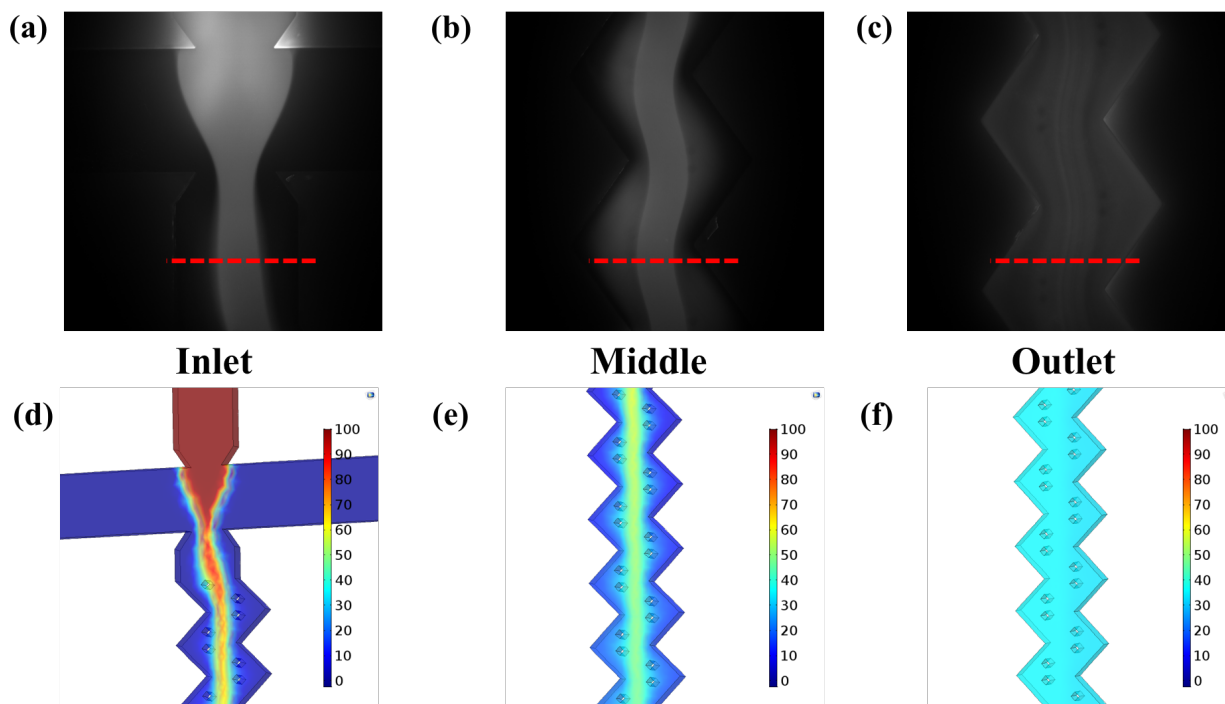
**Figure 6. 4** The relation between volume of HCl and both SCX release efficiency and SAX trap efficiency.

As summarized in Table 1, the alteration of radioactivity was measured at critical steps to assess the efficiency of each process and identify potential areas for optimization. Starting from a full  $^{68}\text{Ga}$  elution from the generator, the total trapping efficiency of the combination of SCX and SAX columns is 73.7%. The total time period required for completing gallium-68 concentration is ~12 min. It is noteworthy to mention that additional optimization on factors such as the selection of SCX and SAX materials (e.g. use of resins with higher porosity and larger surface area) and microchannel design could lead to better overall RCE performance.

<b>Parameter</b>	<b>Run 1</b>	<b>Run 2</b>	<b>Run 3</b>	<b>Run 4</b>	<b>Run 5</b>	<b>Average</b>
<b>Loaded activity (mCi)</b>	30.2	28.4	31.4	29.1	30.1	29.8±1.15
<b>SCX RCE (%)</b>	96.8	97.0	97.1	97.9	93.8	96.5±1.58
<b>SCX RRE (%)</b>	87.3	90.4	91.0	92.5	92.7	90.8±2.18
<b>SAX RCE (%)</b>	87.6	93.3	92.3	87.3	87.2	89.5±3.00
<b>SAX RRE (%)</b>	93.0	94.2	95.0	93.5	93.7	93.9±0.76
<b>Total loss (%)</b>	31.2	22.9	22.5	26.1	29	26.3±3.75
<b>Total trapping (%)</b>	68.8	77.1	77.5	73.9	71	73.7±3.78

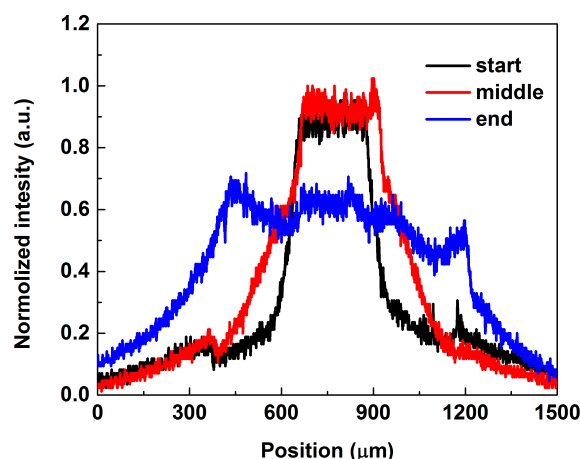
**Table 6. 1** Experimental results of the efficiency of miniaturized SCX and SAX columns at critical steps. All efficiencies are calculated based on decay-corrected values.

Because of the short time period required for gallium-68 incorporation reaction in a microfluidic system (Figure 6a), it is therefore crucial to achieve thorough mixing prior to heating in reactors. It is known that mixing of several streams of solution inside a microfluidic channel depends primarily on diffusion, which occurs in an unfavorably slow manner due to the small Reynolds number ( $Re \ll 1$ ). In this study, we employed a passive microfluidic mixing system that combined the effect of in-plane obstructions inside microchannels and repetitively wavy microchannels (Figure 6.2d). Due to the fact that passive mixing neither complicates device fabrication nor requires additional power, such system hence provides a simple yet efficient fashion to achieve enhanced mixing performance.



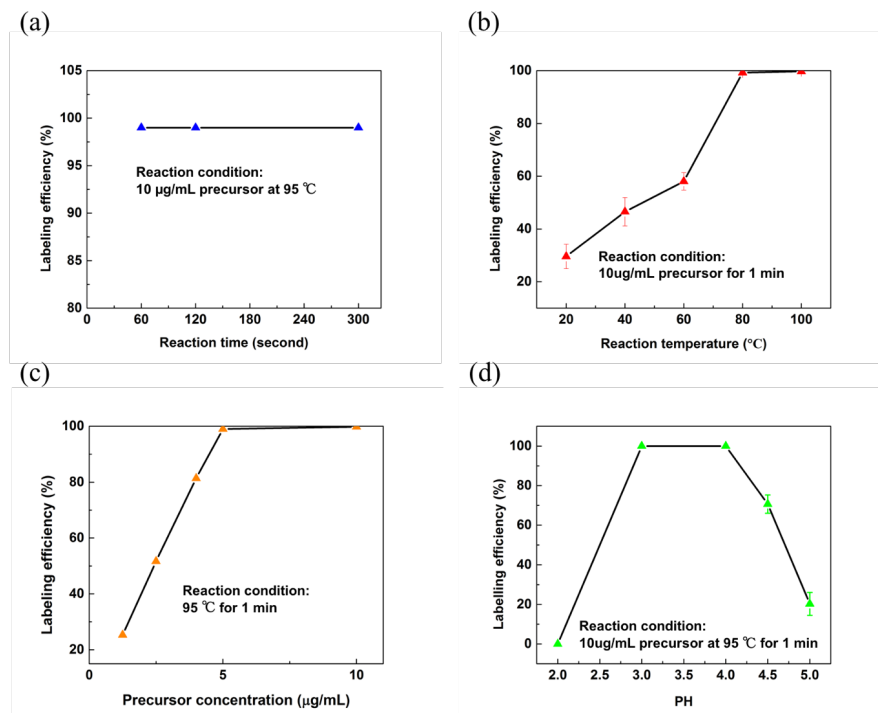
**Figure 6. 5** Experimental evaluation of the mixing performance using the combination of inserted obstructions and zigzag microchannels. The captured fluorescent images indicate mixing results at inlet (a), middle (b) and outlet (c), respectively, which are in good agreement with corresponding numerical simulation.

As shown in Figure 6.2d, a flowing focusing geometry was used at the entrance of mixing section by simultaneously loading released  $^{68}\text{Ga}^{3+}$  from the top and bottom channels and PSMA-11 precursor from the middle channel. In order to characterize its mixing performance, fluorescent beads suspended in water was injected from the middle channel while pure water was injected at the same time from the other two channels. The solution was loaded using two syringe pumps at the rate of  $100\ \mu\text{L}/\text{min}$ . A digital microscope camera (Zeiss) was used to record and visualize the mixing performance along the flow direction at different positions.



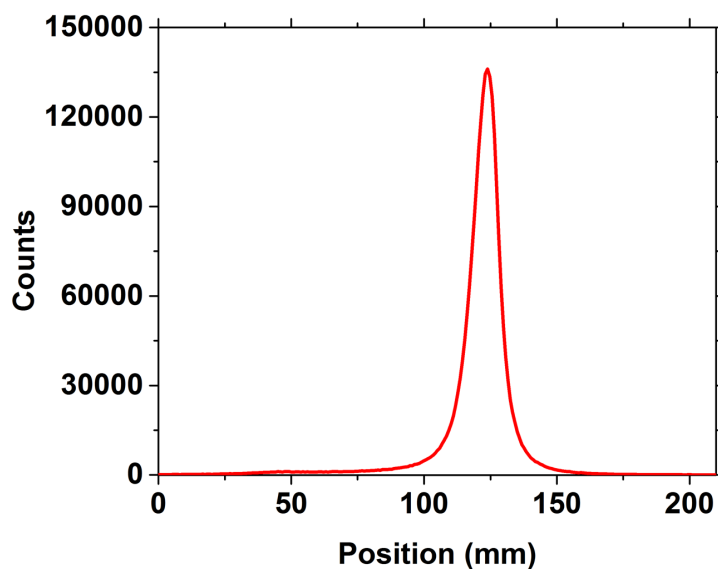
**Figure 6. 6** Normalized fluorescent intensity for characterization of mixing performance after passing through the on-chip mixing module.

Figure 6.5a-c describes captured fluorescent images at the inlet, middle, and outlet of the mixing channel. By visually observing the width alteration of the middle fluorescent stream, it is clear to conclude that sufficient mixing is achieved near the end of channel. Moreover, the mixing performance was quantified by measuring the fluorescent intensity perpendicular to the flow direction (illustrated by red dashed lines) using Image J. Figure 6.6 depicts measured results of the normalized fluorescent intensity versus the width of fluorescent stream. Additionally, COMSOL numerical simulation was performed to predict the mixing tendencies of two solutions based on devised micro-mixers. The red stream injected from the middle channel represents PSMA-11 precursor and the blue streams injected from two side channels represent pre-concentrated gallium-68. The variation of concentration profiles at various positions along the microchannel are shown in Figure 6.7d-f. As expected, simulated mixing patterns are in good agreement with experimental results, indicating the realization of complete mixing after flowing through the micro-mixer.



**Figure 6. 7** Comprehensive investigations regarding optimal reaction conditions for  $^{68}\text{Ga}$  labeling reaction using the developed microfluidic device. Several parameters including reaction time (a), reaction temperature (b), precursor concentration (c), and pH (d) are studied.

Because of enhanced mass and heat transfer in a microfluidic system, traditional reaction conditions that are routinely adopted for macroscale synthesis are not optimal for microfluidic systems. In order to improve microfluidic-based RCY without affecting labelling efficiency, we conducted a systematic study by examining a variety of reaction parameters such as reaction time, reaction temperature, pH, and precursor concentration. In our preliminary investigation, we started from well-established macroscale protocols, specifically heating the mixture consisting of 100 µL concentrated  $^{68}\text{Ga}$  and 100 µL, 10 µg/mL PSMA-11 precursor in a sealed vial at 100 °C for 10 min. Subsequently, we only altered one reaction factor at a time, leaving the other factors unchanged. Therefore, the impact of targeted parameter can be determined using radio-TLC analysis.



**Figure 6. 8** Analytical TLC profile of <sup>68</sup>Ga-PSMA synthesized using the microfluidic chip, showing quantitative conversion.

In our efforts to reduce total synthesis time, we first investigated the correlation between reaction time and resulting reaction efficiency as shown in Figure 5a. We found that our microfluidic system can obtain high conversion efficiency at substantially reduced duration. Specifically, labeling efficiency of ~99% was achieved by heating at 100 °C for 1 min, which consumed one-tenth of the time taken by clinically relevant reactors. Afterwards, we studied the impact of reaction temperature by performing radiosynthesis at diverse temperatures ranging from 20 to 100 °C for 1 min. As shown in Figure 5b, it is clear that sufficient heating is indispensable in order to obtain exceptionally high labeling efficiency. Interestingly, we observed there might exist a threshold temperature (~80 °C) above which labeling efficiency of 99% can be reliably achieved.

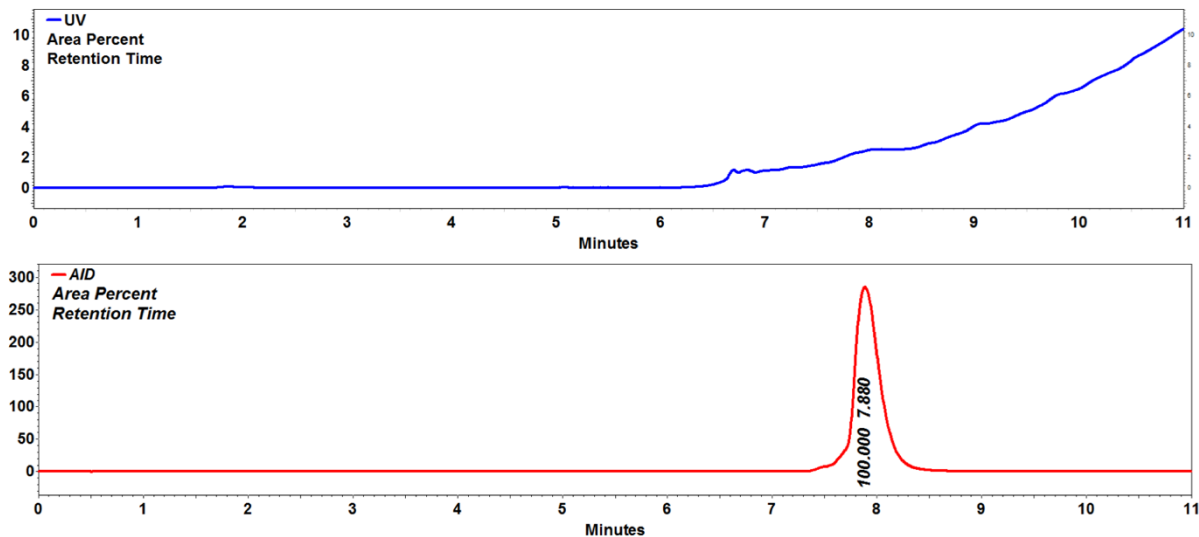


**Figure 6. 9** Analytical HPLC trace of  $^{68}\text{Ga}$ -PSMA. The top blue curve and bottom red curve indicate chemical and radiochemical purity, respectively. The retention time of  $^{68}\text{Ga}$ -PSMA is 7.88 min.

Specific activity of PET tracers is one of the most critical factors that are typically used to evaluate the portion of nonradioactive form of the tracer, which can saturate rare biological receptors, and worsen image quality. In our attempt to achieve high specific activity, experiments focusing on lowering the concentration of PSMA-11 precursor were conducted by performing radiosynthesis under identical conditions (heating at 100 °C for 1 min) except varying on concentration of precursor. As shown in Figure 5c, it is found that 5  $\mu\text{g}$  /mL PSMA-11 precursor is sufficient to result in labeling efficiency of ~99%. Furthermore, the specific activity of isolated product is 20 mCi/ $\mu\text{g}$ , which is 16 times greater than that of routinely produced doses in clinical environment. Additionally, the appropriate range of pH that enabled high-efficiency reaction was found to be 3-4 (Figure 6.7d), which is consistent with macroscale production.

Building on abovementioned results, the optimal reaction conditions in our microfluidic system involve the use of 5  $\mu\text{g}$  /mL PSMA-11 precursor by heating at 100 °C for 1 min. To



guarantee high success, it is essential to note that the complete synthesis must be carried out without the presence of any trace of heavy-metal contaminations. Using developed protocol, tens of synthesis runs have been successfully obtained.

	<b>Traditional</b>	<b>This report</b>
Reactor type	Glass vial (5-20 mL)	Microfluidic device
Radiolabeling conditions	100 °C, 10 min	100 °C, 1 min
Radiochemical purity (%)	>95	>99
Purification	Solid phase purification	Not required
Total time (min)	25- 20 min	15 min
Average RCY (%)	90	70
Specific activity (mCi/ug)	1.25mCi/μg	20 mCi/μg

**Table 6. 2** Production performance comparison between routinely employed system and reported microfluidic system.

To evaluate the overall radiochemical yield of isolated  $^{68}\text{Ga}$ A-PSMA-11, full production runs including concentration, radiosynthesis, and formulation were performed using reported microfluidic platform. The final formulated product was collected as a clear, sterile, and injectable solution. As listed in Table 6.2, total production time, radiochemical yield, and specific activities are compared to those that are routinely obtained in clinical environment. Generally, the developed microfluidic platform demonstrates improved overall performance in terms of reaction efficiency, overall yield, and specific activity than macroscale automated production.

A radio-TLC chromatogram of synthesized product is shown in Figure 6.8 and the  $^{68}\text{Ga}$ -labelled peptide has an approximate retardation factor of 0.8-1.0. Using our microfluidic device, the incorporation efficiency of 100% can be consistently achieved as determined by radio HPLC

chromatogram (Figure 6.9). The only peak at 7.88 min corresponds to the retention time for synthesized  $^{68}\text{Ga}$ -PSMA-11, indicating no remaining of free  $^{68}\text{Ga}$ . It is noteworthy to mention that such high chemical and radiochemical purities allow for further simplification of synthesis procedures as it can eliminate the need of HPLC purification which is routinely required in macroscale system. Additionally, the stability of final product at room temperature was examined by radio-HPLC for duration up to 4 hours. Based on obtained results, no discrepancy on retention time or product purity was observed, suggesting good stability.

<b>Clinical QC test</b>	<b>Clinical acceptance criteria</b>	<b>Analysis of on-chip synthesized PET probes</b>
Appearance	Clear and particle-free	Clear and particle-free
Filter integrity	Meet pressure specify by manufacture	Meet pressure specify by manufacture
pH	4 - 8	4
Radiochemical purity (%)	>90	>99
Identity	Matches retention time of standard (TLC)	Matches retention time of standard (TLC)
Half-life (min)	64-72	68
Sterility	No growth observed for 14 days	No growth observed for 14 days
$^{68}\text{Ge}$ breakthrough	<0.01% of the total radioactivity is $^{68}\text{Ge}$ at the time of product expiration	<0.01% of the total radioactivity is $^{68}\text{Ge}$ at the time of product expiration
Residual solvents	Dependent on methodology	Not required

**Table 6. 3** A comparison between clinical acceptance criteria and quality control tests of synthesized  $^{68}\text{Ga}$ -PSMA using developed microfluidic system.

After adding 2 mL sodium acetate buffer into isolated reaction mixture, the final pH of formulated product was 6-7. After sterile filtration, the reaction mixture exhibited a

radiochemical purity of 100% that satisfied the standard release criterion and the final product can be diluted for dose administration to any desired volume for animal or clinical use. The formulated solution was examined by standard quality control tests to assess its compliance with U.S. Food and Drug Administration requirements for injectable PET tracers (Table 6.3).

After labeling reaction, final isolated products were further processed by quality control, neutralization, and sterile filtration prior to being administered to patients. Standard quality control procedures including TLC, HPLC and measurement of pH value are conducted.

#### **6.4 Conclusion**

We developed a high-yielding and cost-effective microfluidic synthetic platform that can be easily adaptable to clinical environment in synthesis of  $^{68}\text{Ga}$ -PSMA for molecular imaging and  $^{177}\text{Lu}$ -PSMA for targeted therapy. Our microfluidic device demonstrated many desirable characteristics by enabling preparation of diverse radiopharmaceuticals in a fast, efficient and cost-effective manner. Without the need of any additional procedures, isolated final products were in superior compliance with QC requirements, thus allowing for direct administration to patients. Notably, achieving radiosynthesis of highly demanded  $^{68}\text{Ga}$ -PSMA and  $^{177}\text{Lu}$ -PSMA in a low-cost fashion represent a significant advancement towards the realization of personalized medicine.

## Chapter 7 Summary and Outlook

This thesis work has covered three diverse research areas, ranging from the development of temperature-sensitive transient composites and antenna circuits, development of compact microfluidic systems for synthesis of various PET radiotracers, and investigation the thermal and mechanical properties of electrospun polymer nanofibers. In this dissertation, efforts are devoted to advancing our understanding and expanding the range of applications in each specific field.

First, the recent emergence and rapid development of transient electronics have found extensive use in areas such as zero-waster electronics, information-sensitive storage, and retrieval-free biomedical implants. The current research focus from the perspective of material science is to develop novel constituent materials that enable triggered transience upon an external stimulus, such as pH, light, temperature, and mechanical stress. To construct advanced transient systems that can respond to external stimuli, I primarily focused on a class of biocompatible polymeric materials that exhibit LCST (i.e. PNIPAm and MC). First, a thermoresponsive conductive composites was developed by mixing LCST polymers with conductive nanofillers. When the solution temperature was above LCST, such composites maintained stable conductance. However, abrupt loss of conductance and physical disintegration was observed as the solution temperature dropped below LCST. In particular, methyl cellulose was comprehensively investigated to demonstrate its potential for thermally triggered transient systems. A set of relevant techniques was developed to enable the construction of MC-based transient RFID device that can be wirelessly interrogated in bio-mimic environment.

There are several directions that researchers can take to advance this technology. First, future effort may attempt to verify its thermally triggered transient behavior after surgical

implant in mice. It is critical to make sure that developed MC-based transient RFID device can demonstrate wanted thermoresponsive transience without causing adverse reaction such as inflammation. Moreover, exploration on alternative stimuli-responsive materials could also be of interest because such polymers serve as the foundation for construction of novel stimuli-responsive transient systems. Pursuing in this direction requires close collaboration with polymer chemists and it might be promising to first focus on modification of those well-established smart polymers. Furthermore, silver nanowires are not completely biocompatible. Thus, it would be of significance to replace AgNWs with other conductive fillers (i.e. gold nanowires, carbon nanotubes), which can eliminate concerns regarding toxicity.

Second, PET is a powerful, non-invasive imaging technique that has been increasingly employed for disease diagnosis and targeted treatment. Though we have witnessed successful development of a multitude of PET radiotracers in research laboratories, there are only a handful of those are routinely produced for clinical use because of the complexity and high-cost associated with radiosynthesis. In this work, I attempt to leverage the confluence of microfluidics and radiopharmaceutical synthesis by developing disposable microfluidic systems to enable low-cost and high-yielding production of novel PET molecular probes. Miniaturized on-chip columns were developed to enable trapping and release of radioisotopes of interest. Chemical synthesis in microfluidic reactors has been proved to be an efficient approach with rapid reaction kinetics and high labelling efficiency. Furthermore, we achieved on-chip purification of crude [ $^{18}\text{F}$ ]fallypride and delivered isolated products with qualities suitable for preclinical imaging. In addition, another versatile microfluidic system was developed to synthesize both  $^{68}\text{Ga}$ -PSMA and  $^{177}\text{Lu}$ -PSMA. Analysis of isolated products were in good agreement with clinical acceptance criteria, thus suggesting promising potential for use in clinical production. Future work may focus on

integrating automatic control systems with disposable microfluidic platforms to enable on-demand synthesis of PET radiotracers. Though a collection of proof-of-principle microfluidic systems have demonstrated particular advantages for PET synthesis in the past decades, it is still ambiguous that any of these platforms is currently mature enough to be adapted for large-scale clinic production. Hence, there still are exciting opportunities to further optimize reaction procedures, reduce the overall cost, and realize on-demand synthesis of radiotracers of interest.

Though bulk polymeric materials are generally regarded as poor thermal conductors and have thermal conductivity on the order of  $0.1 \text{ W m}^{-1} \text{ K}^{-1}$ , recent efforts including both numerical simulation and experimental verification revealed that polymer nanofibers consisting of a handful of individual chains can have significantly high thermal conductivity (up to  $\sim 104 \text{ W m}^{-1} \text{ K}^{-1}$ ).<sup>136</sup> In this thesis, we investigated the role of polymer chain length and weight of side groups in thermal transport by experimentally probing thermal conductivity of several electrospun polymer nanofibers. In order to further understand the enhanced thermal conductivity, Raman spectroscopy and atomic force microscope were employed to characterize the degree of crystallinity and Young's moduli of obtained electrospun nanofibers, respectively. Though enhanced thermal conductivity was obtained, there is also the possibility that nanofibers consisting of several molecular chains may exhibit surprisingly high thermal conductivity. One potential approach to manufacture such samples is to stretch collected electrospun fibers in a controlled manner. Though many issues still remain, electrospun polymer nanofibers could play an important role in applications such as flexible electronics and photovoltaic cells.

## REFERENCES

1. Ladd, T. D. *et al.* Quantum computers. *Nature* **464**, 45–53 (2010).
2. Zhang, H. F., Maslov, K., Stoica, G. & Wang, L. V. Functional photoacoustic microscopy for high-resolution and noninvasive in vivo imaging. *Nat. Biotechnol.* **24**, 848–851 (2006).
3. Peer, D. *et al.* Nanocarriers as an emerging platform for cancer therapy. *Nat. Nanotechnol.* **2**, 751–760 (2007).
4. Rogers, J. a, Lagally, M. G. & Nuzzo, R. G. Synthesis, assembly and applications of semiconductor nanomembranes. *Nature* **477**, 45–53 (2011).
5. Ying, M. *et al.* Silicon nanomembranes for fingertip electronics. *Nanotechnology* **23**, (2012).
6. Choi, W. M. *et al.* Biaxially stretchable ‘wavy’ silicon nanomembranes. *Nano Lett.* **7**, 1655–1663 (2007).
7. Son, D. *et al.* Multifunctional wearable devices for diagnosis and therapy of movement disorders. *Nat. Nanotechnol.* **9**, 397–404 (2014).
8. Hochberg, L. R. *et al.* Neuronal ensemble control of prosthetic devices by a human with tetraplegia. *Nature* **442**, 164–171 (2006).
9. Jain, S., Hirst, D. G. & O’Sullivan, J. M. Gold nanoparticles as novel agents for cancer therapy. *Br. J. Radiol.* **85**, 101–113 (2012).
10. Stankovich, S. *et al.* Graphene-based composite materials. *Nature* **442**, 282–286 (2006).
11. Moaisala, A., Li, Q., Kinloch, I. A. & Windle, A. H. Thermal and electrical conductivity of single- and multi-walled carbon nanotube-epoxy composites. *Compos. Sci. Technol.* **66**, 1285–1288 (2006).
12. Hwang, S.-W. *et al.* A Physically Transient Form of Silicon Electronics. *Science (80-. ).* **337**, 1640–1644 (2012).
13. Fu, K. K., Wang, Z., Dai, J., Carter, M. & Hu, L. Transient Electronics: Materials and Devices. *Chem. Mater.* **28**, 3527–3539 (2016).
14. Acar, H. *et al.* Study of Physically Transient Insulating Materials as a Potential Platform for Transient Electronics and Bioelectronics. *Adv. Funct. Mater.* **24**, 4135–4143 (2014).
15. Huang, X. *et al.* Biodegradable Materials for Multilayer Transient Printed Circuit Boards. *Adv. Mater.* **26**, 7371–7377 (2014).
16. Park, C. W. *et al.* Thermally Triggered Degradation of Transient Electronic Devices. *Adv. Mater.* **27**, 3783–3788 (2015).
17. Lee, C. H. *et al.* Wireless Microfluidic Systems for Programmed, Functional Transformation of Transient Electronic Devices. *Adv. Funct. Mater.* **25**, 5100–5106 (2015).
18. Sun, S. & Zeng, H. Size-controlled synthesis of magnetite nanoparticles. *J. Am. Chem. Soc.* **124**, 8204–8205 (2002).
19. Sun, Y. *et al.* Shape-controlled synthesis of gold and silver nanoparticles. *Science* **298**, 2176–9 (2002).
20. Molenkamp, W. C., Watanabe, M., Miyata, H. & Tolbert, S. H. Highly polarized luminescence from optical quality films of a semiconducting polymer aligned within oriented mesoporous silica. *J. Am. Chem. Soc.* **126**, 4476–4477 (2004).
21. Sundrani, D., Darling, S. B. & Sibener, S. J. Hierarchical assembly and compliance of aligned nanoscale polymer cylinders in confinement. *Langmuir* **20**, 5091–5099 (2004).
22. Lu, X., Wang, C. & Wei, Y. One-dimensional composite nanomaterials: Synthesis by electrospinning and their applications. *Small* **5**, 2349–2370 (2009).
23. Wu, H. *et al.* A transparent electrode based on a metal nanotrough network. *Nat. Nanotechnol.* **8**, 421–425 (2013).

24. Wang, X. *et al.* Electrospun Nanofibrous Membranes for Highly Sensitive Optical Sensors. *Nano Lett.* **2**, 1273–1275 (2002).
25. Sawicka, K., Gouma, P. & Simon, S. Electrospun biocomposite nanofibers for urea biosensing. *Sensors Actuators, B Chem.* **108**, 585–588 (2005).
26. Patel, A. C., Li, S., Yuan, J. M. & Wei, Y. In situ encapsulation of horseradish peroxidase in electrospun porous silica fibers for potential biosensor applications. *Nano Lett.* **6**, 1042–1046 (2006).
27. Elvira, K. S., i Solvas, X. C., Wootton, R. C. R. & DeMello, A. J. The past, present and potential for microfluidic reactor technology in chemical synthesis. *Nat. Chem.* **5**, 905–915 (2013).
28. Xu, S. *et al.* Generation of Monodisperse Particles by Using Microfluidics: Control over Size, Shape, and Composition. *Angew. Chemie* **117**, 734–738 (2005).
29. Whitesides, G. M. The origins and the future of microfluidics. *Nature* **442**, 368–373 (2006).
30. Lee, C.-C. Multistep Synthesis of a Radiolabeled Imaging Probe Using Integrated Microfluidics. *Science (80-. )*. **310**, 1793–1796 (2005).
31. Dagdeviren, C. *et al.* Transient, biocompatible electronics and energy harvesters based on ZnO. *Small* **9**, 3398–3404 (2013).
32. Berggren, M. & Richter-Dahlfors, A. Organic bioelectronics. *Adv. Mater.* **19**, 3201–3213 (2007).
33. Kim, Y. J., Wu, W., Chun, S., Whitacre, J. F. & Bettinger, C. J. Biologically derived melanin electrodes in aqueous sodium-ion energy storage devices. *Proc. Natl. Acad. Sci. U. S. A.* **110**, 20912–7 (2013).
34. Yin, L. *et al.* Dissolvable metals for transient electronics. *Adv. Funct. Mater.* **24**, 645–658 (2014).
35. Yin, L. *et al.* Mechanisms for Hydrolysis of Silicon Nanomembranes as Used in Bioresorbable Electronics. *Adv. Mater.* **27**, 1857–1864 (2015).
36. Hwang, S. W. *et al.* Dissolution chemistry and biocompatibility of single-crystalline silicon nanomembranes and associated materials for transient electronics. *ACS Nano* **8**, 5843–5851 (2014).
37. Kang, S. K. *et al.* Dissolution chemistry and biocompatibility of silicon- and germanium-based semiconductors for transient electronics. *ACS Appl. Mater. Interfaces* **7**, 9297–9305 (2015).
38. Lei, T. *et al.* Biocompatible and totally disintegrable semiconducting polymer for ultrathin and ultralightweight transient electronics. *Proc. Natl. Acad. Sci.* **114**, 201701478 (2017).
39. Jin, S. H. *et al.* Solution-processed single-walled carbon nanotube field effect transistors and bootstrapped inverters for disintegratable, transient electronics. *Appl. Phys. Lett.* **105**, 2012–2016 (2014).
40. Kang, S. *et al.* Bioresorbable silicon electronic sensors for the brain. *Nature* **530**, 71–76 (2016).
41. Fu, K. *et al.* Transient Rechargeable Batteries Triggered by Cascade Reactions. *Nano Lett.* **15**, 4664–4671 (2015).
42. Lopez Hernandez, H. *et al.* Triggered transience of metastable poly(phthalaldehyde) for transient electronics. *Adv. Mater.* **26**, 7637–7642 (2014).
43. Ametamey, S. M., Honer, M. & Schubiger, P. A. Molecular imaging with PET. *Chem. Rev.* **108**, 1501–16 (2008).
44. Audrain, H. Positron Emission Tomography (PET) and Microfluidic Devices: A Breakthrough on the Microscale? *Angew. Chemie Int. Ed.* **46**, 1772–1775 (2007).
45. Elizarov, A. M. Microreactors for radiopharmaceutical synthesis. *Lab Chip* **9**, 1326–1333 (2009).
46. Zacheo, A. *et al.* Radioactivity resistance evaluation of polymeric materials for application in radiopharmaceutical production at microscale. *Microfluid. Nanofluidics* **11**, 35–44 (2011).
47. Gillies, J. M. *et al.* Microfluidic reactor for the radiosynthesis of PET radiotracers. *Appl. Radiat. Isot.* **64**, 325–32 (2006).
48. Gillies, J. M. *et al.* Microfluidic technology for PET radiochemistry. *Appl. Radiat. Isot.* **64**, 333–336 (2006).
49. Elizarov, A. M. Microreactors for radiopharmaceutical synthesis. *Lab Chip* **9**, 1326 (2009).
50. Javed, M. R. *et al.* High yield and high specific activity synthesis of [<sup>18</sup>F]fallypride in a batch



- microfluidic reactor for micro-PET imaging. *Chem. Commun.* **50**, 1192–1194 (2014).
51. Chen, S. *et al.* Radiolabelling diverse positron emission tomography (PET) tracers using a single digital microfluidic reactor chip. *Lab Chip* **14**, 902–910 (2014).
  52. Ding, H. *et al.* Accurate dispensing of volatile reagents on demand for chemical reactions in EWOD chips. *Lab Chip* **12**, 3331 (2012).
  53. Keng, P. Y. *et al.* Micro-chemical synthesis of molecular probes on an electronic microfluidic device. *Proc. Natl. Acad. Sci.* **109**, 690–695 (2012).
  54. Bejot, R. *et al.* Batch-mode microfluidic radiosynthesis of N-succinimidyl-4-[<sup>18</sup>F]fluorobenzoate for protein labelling. *J. Label. Compd. Radiopharm.* **54**, 117–122 (2011).
  55. Steel, C. J., O'Brien, A. T., Luthra, S. K. & Brady, F. Automated PET radiosyntheses using microfluidic devices. *J. Label. Compd. Radiopharm.* **50**, 308–311 (2007).
  56. Lebedev, A. *et al.* Batch-reactor microfluidic device: First human use of a microfluidically produced PET radiotracer. *Lab Chip* 136–145 (2012). doi:10.1039/c2lc40853h
  57. Arima, V. *et al.* Radiochemistry on chip: towards dose-on-demand synthesis of PET radiopharmaceuticals. *Lab Chip* **13**, 2328–36 (2013).
  58. Son, D. *et al.* Bioresorbable Electronic Stent Integrated with Therapeutic Nanoparticles for Endovascular Diseases. *ACS Nano* **9**, 5937–5946 (2015).
  59. Tao, H. *et al.* Silk-based resorbable electronic devices for remotely controlled therapy and in vivo infection abatement. *Proc. Natl. Acad. Sci.* **111**, 17385–17389 (2014).
  60. Douglas, A., Muralidharan, N., Carter, R., Share, K. & Pint, C. L. Ultrafast triggered transient energy storage by atomic layer deposition into porous silicon for integrated transient electronics. *Nanoscale* **8**, 7384–7390 (2016).
  61. Chen, Z. *et al.* Fast and reversible thermoresponsive polymer switching materials for safer batteries. *Nat. Energy* **1**, 15009 (2016).
  62. Yin, L., Bozler, C., Harburg, D. V., Omenetto, F. & Rogers, J. A. Materials and fabrication sequences for water soluble silicon integrated circuits at the 90 nm node. *Appl. Phys. Lett.* **106**, 14105 (2015).
  63. Xia, Y., Sun, K. & Ouyang, J. Solution-processed metallic conducting polymer films as transparent electrode of optoelectronic devices. *Adv. Mater.* **24**, 2436–2440 (2012).
  64. Wu, H. *et al.* Electrospun metal nanofiber webs as high-performance transparent electrode. *Nano Lett.* **10**, 4242–4248 (2010).
  65. Jiang, H., Moon, K. S., Li, Y. & Wong, C. P. Surface functionalized silver nanoparticles for ultrahigh conductive polymer composites. *Chem. Mater.* **18**, 2969–2973 (2006).
  66. Merilampi, S., Laine-Ma, T. & Ruuskanen, P. The characterization of electrically conductive silver ink patterns on flexible substrates. *Microelectron. Reliab.* **49**, 782–790 (2009).
  67. Yin, L. *et al.* Materials, designs, and operational characteristics for fully biodegradable primary batteries. *Adv. Mater.* **26**, 3879–3884 (2014).
  68. Hwang, S. W. *et al.* High-performance biodegradable/transient electronics on biodegradable polymers. *Adv. Mater.* **26**, 3905–3911 (2014).
  69. Hwang, S. W. *et al.* Materials and fabrication processes for transient and bioresorbable high-performance electronics. *Adv. Funct. Mater.* **23**, 4087–4093 (2013).
  70. Hwang, S. W. *et al.* 25th anniversary article: Materials for high-performance biodegradable semiconductor devices. *Adv. Mater.* **26**, 1992–2000 (2014).
  71. Kang, S. K. *et al.* Dissolution behaviors and applications of silicon oxides and nitrides in transient electronics. *Adv. Funct. Mater.* **24**, 4427–4434 (2014).
  72. Jamshidi, R., Çinar, S., Chen, Y., Hashemi, N. & Montazami, R. Transient bioelectronics: Electronic properties of silver microparticle-based circuits on polymeric substrates subjected to mechanical load. *J. Polym. Sci. Part B Polym. Phys.* **53**, 1603–1610 (2015).
  73. Li, L. *et al.* Gel network structure of methylcellulose in water. *Langmuir* **17**, 8062–8068 (2001).
  74. Liu, W. *et al.* A rapid temperature-responsive sol-gel reversible poly(N-isopropylacrylamide)-g-methylcellulose copolymer hydrogel. *Biomaterials* **25**, 3005–3012 (2004).

75. Xu, F. & Zhu, Y. Highly conductive and stretchable silver nanowire conductors. *Adv. Mater.* **24**, 5117–5122 (2012).
76. Liu, C.-H. & Yu, X. Silver nanowire-based transparent, flexible, and conductive thin film. *Nanoscale Res. Lett.* **6**, 75 (2011).
77. White, S. I. *et al.* Electrical Percolation Behavior in Silver Nanowire-Polystyrene Composites: Simulation and Experiment. *Adv. Funct. Mater.* **20**, 2709–2716 (2010).
78. Shibuya, M., Yamamura, S., Matsue, T. & Uchida, I. In Situ Conductivity Measurements during Lithium Intercalation/Deintercalation on V2O5 Thin Film by Using Interdigitated Microarray Electrodes. *Chem. Lett.* **143**, 749–750 (1995).
79. Olthuis, W., Streekstra, W. & Bergveld, P. Theoretical and experimental determination of cell constants of planar-interdigitated electrolyte conductivity sensors. *Sensors Actuators, B Chem.* **24**, 252–256 (1995).
80. Kang, S. K. *et al.* Biodegradable thin metal foils and spin-on glass materials for transient electronics. *Adv. Funct. Mater.* **25**, 1789–1797 (2015).
81. Tibbitt, M. W., Dahlman, J. E. & Langer, R. Emerging Frontiers in Drug Delivery. *J. Am. Chem. Soc.* **138**, 704–717 (2016).
82. Lee, J. B. *et al.* Development of 3D Microvascular Networks Within Gelatin Hydrogels Using Thermoresponsive Sacrificial Microfibers. *Adv. Healthc. Mater.* **5**, 781–785 (2016).
83. Jain, S., Sandhu, P. S., Malvi, R. & Gupta, B. Cellulose derivatives as thermoresponsive polymer: An overview. *J. Appl. Pharm. Sci.* **3**, 139–144 (2013).
84. Wang, Q. & Li, L. Effects of molecular weight on thermoreversible gelation and gel elasticity of methylcellulose in aqueous solution. *Carbohydr. Polym.* **62**, 232–238 (2005).
85. Sarkar, N. Kinetics of thermal gelation of methylcellulose and hydroxypropylmethylcellulose in aqueous solutions. *Carbohydr. Polym.* **26**, 195–203 (1995).
86. Rogers, J. A., Someya, T. & Huang, Y. Materials and Mechanics for Stretchable Electronics. *Science (80-. )*. **327**, 1603–1607 (2010).
87. Lee, J. *et al.* Very long Ag nanowire synthesis and its application in a highly transparent, conductive and flexible metal electrode touch panel. *Nanoscale* **4**, 6408 (2012).
88. Bauer, S. *et al.* 25th Anniversary Article: A Soft Future: From Robots and Sensor Skin to Energy Harvesters. *Adv. Mater.* **26**, 149–162 (2014).
89. 8331 - Silver Conductive Epoxy, High Conductivity - 10 Minute Working Time - Electrically Conductive Adhesives | MG Chemicals. at <<http://www.mgchemicals.com/products/adhesives/electrically-conductive-adhesives/silver-conductive-epoxy-8331>>
90. Hu, L., Kim, H. S., Lee, J., Peumans, P. & Cui, Y. Scalable Coating and Properties of Transparent, Flexible, Silver Nanowire Electrodes. *ACS Nano* **4**, 2955–2963 (2010).
91. Wuelfing, W. P. & Murray, R. W. Electron hopping through films of arenethiolate monolayer-protected gold clusters. *J. Phys. Chem. B* **106**, 3139–3145 (2002).
92. Balberg, I. & Binenbaum, N. Invariant properties of the percolation thresholds in the soft-core hard-core transition. *Phys. Rev. A* **35**, 5174–5177 (1987).
93. Li, J. & Östling, M. Percolation thresholds of two-dimensional continuum systems of rectangles. *Phys. Rev. E* **88**, 1–8 (2013).
94. Zeng, X. Y., Zhang, Q. K., Yu, R. M. & Lu, C. Z. A new transparent conductor: Silver nanowire film buried at the surface of a transparent polymer. *Adv. Mater.* **22**, 4484–4488 (2010).
95. Lee, P. *et al.* Highly stretchable and highly conductive metal electrode by very long metal nanowire percolation network. *Adv. Mater.* **24**, 3326–3332 (2012).
96. Abd El-Kader, M. F. H. & Ragab, H. S. DC conductivity and dielectric properties of maize starch/methylcellulose blend films. *Ionics (Kiel)*. **19**, 361–369 (2013).
97. Chang, J.-K. *et al.* Biodegradable Electronic Systems in 3D, Heterogeneously Integrated Formats. *Adv. Mater.* **30**, 1704955 (2018).
98. Feig, V. R., Tran, H. & Bao, Z. Biodegradable Polymeric Materials in Degradable Electronic

- Devices. *ACS Cent. Sci.* **4**, 337–348 (2018).
99. Chen, X. *et al.* CVD-grown monolayer MoS<sub>2</sub> in bioabsorbable electronics and biosensors. *Nat. Commun.* **9**, 1–12 (2018).
  100. Kim, Y. J., Chun, S. E., Whitacre, J. & Bettinger, C. J. Self-deployable current sources fabricated from edible materials. *J. Mater. Chem. B* **1**, 3781–3788 (2013).
  101. Koo, J. *et al.* Wireless bioresorbable electronic system enables sustained nonpharmacological neuroregenerative therapy. *Nat. Med.* (2018). doi:10.1038/s41591-018-0196-2
  102. Yu, K. J. *et al.* Bioresorbable silicon electronics for transient spatiotemporal mapping of electrical activity from the cerebral cortex. *Nat. Mater.* **15**, 782–791 (2016).
  103. Kang, S. K. *et al.* Bioresorbable silicon electronic sensors for the brain. *Nature* **530**, 71–76 (2016).
  104. Pandey, S. S., Banerjee, N., Xie, Y. & Mastrangelo, C. H. Self-Destructing Secured Microchips by On-Chip Triggered Energetic and Corrosive Attacks for Transient Electronics. *Adv. Mater. Technol.* **3**, 1–14 (2018).
  105. Vivekananthan, V. *et al.* Biocompatible Collagen Nanofibrils: An Approach for Sustainable Energy Harvesting and Battery-Free Humidity Sensor Applications. *ACS Appl. Mater. Interfaces* **10**, 18650–18656 (2018).
  106. Pal, R. K., Kundu, S. C. & Yadavalli, V. K. Fabrication of Flexible, Fully Organic, Degradable Energy Storage Devices Using Silk Proteins. *ACS Appl. Mater. Interfaces* **10**, 9620–9628 (2018).
  107. Kang, S. K., Koo, J., Lee, Y. K. & Rogers, J. A. Advanced Materials and Devices for Bioresorbable Electronics. *Acc. Chem. Res.* **51**, 988–998 (2018).
  108. Yu, X., Shou, W., Mahajan, B. K., Huang, X. & Pan, H. Materials, Processes, and Facile Manufacturing for Bioresorbable Electronics: A Review. *Adv. Mater.* **30**, 1–27 (2018).
  109. Gao, Y. *et al.* Moisture-triggered physically transient electronics. *Sci. Adv.* **3**, 1–9 (2017).
  110. Zhang, X. & Bellan, L. M. Composites Formed from Thermoresponsive Polymers and Conductive Nanowires for Transient Electronic Systems. *ACS Appl. Mater. Interfaces* **9**, 21991–21997 (2017).
  111. Yoon, J. *et al.* Three-Dimensional Printed Poly(vinyl alcohol) Substrate with Controlled On-Demand Degradation for Transient Electronics. *ACS Nano* **12**, 6006–6012 (2018).
  112. Jeong, B., Kim, S. W. & Bae, Y. H. Thermosensitive sol-gel reversible hydrogels. *Adv. Drug Deliv. Rev.* **64**, 154–162 (2012).
  113. Selvarasah, S. *et al.* A reusable high aspect ratio parylene-C shadow mask technology for diverse micropatterning applications. *Sensors Actuators A Phys.* **145–146**, 306–315 (2008).
  114. Won, S. M. *et al.* Natural Wax for Transient Electronics. *Adv. Funct. Mater.* **1801819**, 1801819 (2018).
  115. Rodger, D. C. *et al.* Flexible parylene-based microelectrode technology for intraocular retinal prostheses. *Proc. 1st IEEE Int. Conf. Nano Micro Eng. Mol. Syst. 1st IEEE-NEMS* 743–746 (2006). doi:10.1109/NEMS.2006.334886
  116. Carlson, A., Bowen, A. M., Huang, Y., Nuzzo, R. G. & Rogers, J. A. Transfer Printing Techniques for Materials Assembly and Micro/Nanodevice Fabrication. *Adv. Mater.* **24**, 5284–5318 (2012).
  117. Xue, Y. *et al.* A wireless closed-loop system for optogenetic peripheral neuromodulation. *Nature* **565**, 361–365 (2018).
  118. Gómez-Carracedo, A., Alvarez-Lorenzo, C., Gómez-Amoza, J. L. & Concheiro, A. Chemical structure and glass transition temperature of non-ionic cellulose ethers DSC, TMDSC®: Oscillatory rheometry study. *J. Therm. Anal. Calorim.* **73**, 587–596 (2003).
  119. Tan, C. P., Cipriany, B. R., Lin, D. M. & Craighead, H. G. Nanoscale resolution, multicomponent biomolecular arrays generated by aligned printing with parylene peel-off. *Nano Lett.* **10**, 719–725 (2010).
  120. Ilic, B. & Craighead, H. G. Topographical Patterning of Chemically Sensitive Biological Materials Using a Polymer-Based Dry Lift Off. *Biomed. Microdevices* **2**, 317–322 (2000).
  121. Xylouri, E. M., Patrikakis, C. Z., Voulodimos, A. S., Sideridis, A. B. & Ntakis, V. A. A complete farm management system based on animal identification using RFID technology. *Comput. Electron. Agric.* **70**, 380–388 (2009).

122. Preradovic, S., Balbin, I., Karmakar, N. C. & Swiegers, G. F. Multiresonator-Based Chipless RFID System for Low-Cost Item Tracking. *IEEE Trans. Microw. Theory Tech.* **57**, 1411–1419 (2009).
123. Lodato, R., Marrocco, G., Amendola, S., Manzari, S. & Occhiuzzi, C. RFID Technology for IoT-Based Personal Healthcare in Smart Spaces. *IEEE Internet Things J.* **1**, 144–152 (2014).
124. Lee, Y. K. *et al.* Room Temperature Electrochemical Sintering of Zn Microparticles and Its Use in Printable Conducting Inks for Bioresorbable Electronics. *Adv. Mater.* **29**, 1–8 (2017).
125. Brenckle, M. A. *et al.* Methods and Applications of Multilayer Silk Fibroin Laminates Based on Spatially Controlled Welding in Protein Films. *Adv. Funct. Mater.* **26**, 44–50 (2016).
126. Mohan, S. S., Hershenson, M. D. M., Boyd, S. P. & Lee, T. H. Simple accurate expressions for planar spiral inductances. *IEEE J. Solid-State Circuits* **34**, 1419–1420 (1999).
127. Rao, K. V. S., Member, S., Nikitin, P. V & Lam, S. F. Antenna Design for UHF RFID Tags : A Review and a Practical Application. **53**, 3870–3876 (2005).
128. Komoda, N. *et al.* Printed silver nanowire antennas with low signal loss at high-frequency radio. *Nanoscale* **4**, 3148 (2012).
129. Burroughes, J. H. *et al.* Light-emitting diodes based on conjugated polymers. *Nature* **347**, 539–541 (1990).
130. Gustafsson, G. *et al.* Flexible light-emitting diodes made from soluble conducting polymers. *Nature* **357**, 477–479 (1992).
131. Granström, M. *et al.* Laminated fabrication of polymeric photovoltaic diodes. *Nature* **395**, 257–260 (1998).
132. He, Z. *et al.* Single-junction polymer solar cells with high efficiency and photovoltage. *Nat. Photonics* **9**, 174–179 (2015).
133. Forrest, S. R. The path to ubiquitous and low-cost organic electronic appliances on plastic. *Nature* **428**, 911–918 (2004).
134. Klauk, H. Organic thin-film transistors. *Chem. Soc. Rev.* **39**, 2643–2666 (2010).
135. Henry, A. & Chen, G. High thermal conductivity of single polyethylene chains using molecular dynamics simulations. *Phys. Rev. Lett.* **101**, 1–4 (2008).
136. Shen, S., Henry, A., Tong, J., Zheng, R. & Chen, G. Polyethylene nanofibres with very high thermal conductivities. *Nat. Nanotechnol.* **5**, 251–255 (2010).
137. Singh, V. *et al.* High thermal conductivity of chain-oriented amorphous polythiophene. *Nat. Nanotechnol.* **9**, 384–390 (2014).
138. Kim, G.-H. *et al.* High thermal conductivity in amorphous polymer blends by engineered interchain interactions. *Nat. Mater.* **14**, 295–300 (2014).
139. Wang, C. *et al.* Superior thermal conductivity in suspended bilayer hexagonal boron nitride. *Sci. Rep.* **6**, 25334 (2016).
140. Ma, J. *et al.* Thermal conductivity of electrospun polyethylene nanofibers. *Nanoscale* **7**, 16899–16908 (2015).
141. Liao, Q., Zeng, L., Liu, Z. & Liu, W. Tailoring thermal conductivity of single-stranded carbon-chain polymers through atomic mass modification. *Sci. Rep.* **6**, 34999 (2016).
142. Zhong, Z. *et al.* Structure-induced enhancement of thermal conductivities in electrospun polymer nanofibers. *Nanoscale* **6**, 8283–8291 (2014).
143. Shrestha, R. *et al.* Crystalline polymer nanofibers with ultra-high strength and thermal conductivity. *Nat. Commun.* **9**, 1664 (2018).
144. Canetta, C., Guo, S. & Narayanaswamy, A. Measuring thermal conductivity of polystyrene nanowires using the dual-cantilever technique. *Rev. Sci. Instrum.* **85**, 104901 (2014).
145. Ma, H. & Tian, Z. Effects of polymer topology and morphology on thermal transport: A molecular dynamics study of bottlebrush polymers. *Appl. Phys. Lett.* **110**, 91903 (2017).
146. Ma, H., O'Donnell, E. & Tian, Z. Tunable thermal conductivity of  $\pi$ -conjugated two-dimensional polymers. *Nanoscale* **10**, 13924–13929 (2018).
147. Li, D. *et al.* Thermal conductivity of individual silicon nanowires. *Appl. Phys. Lett.* **83**, 2934–2936

- (2003).
148. Wingert, M. C., Chen, Z. C. Y., Kwon, S., Xiang, J. & Chen, R. Ultra-sensitive thermal conductance measurement of one-dimensional nanostructures enhanced by differential bridge. *Rev. Sci. Instrum.* **83**, 24901 (2012).
  149. Moore, A. L. & Shi, L. On errors in thermal conductivity measurements of suspended and supported nanowires using micro-thermometer devices from low to high temperatures. *Meas. Sci. Technol.* **22**, 15103 (2010).
  150. Zhang, Q. *et al.* Defect facilitated phonon transport through kinks in boron carbide nanowires. *Nano Lett.* **17**, 3550–3555 (2017).
  151. Yang, L. *et al.* Ballistic Phonon Penetration Depth in Amorphous Silicon Dioxide. *Nano Lett.* **17**, 7218–7225 (2017).
  152. Mark, J. E. *Physical Properties of Polymers Handbook*. (Springer New York, 2007).
  153. Xie, X. *et al.* Thermal Conductivity, Heat Capacity, and Elastic Constants of Water-Soluble Polymers and Polymer Blends. *Macromolecules* **49**, 972–978 (2016).
  154. Ibeh, C. C. *Thermoplastic materials : properties, manufacturing methods, and applications*. (CRC Press, 2011).
  155. Asahina, M. & Enomoto, S. Elastic moduli of oriented polymers. II.(- A1- A2-) n-type polymers. *J. Polym. Sci.* **59**, 101–111 (1962).
  156. Tashiro, K. Molecular theory of mechanical properties of crystalline polymers. *Prog. Polym. Sci.* **18**, 377–435 (1993).
  157. Li, P., Hu, L., McGaughey, A. J. H. & Shen, S. Crystalline polyethylene nanofibers with the theoretical limit of Young's modulus. *Adv. Mater.* **26**, 1065–1070 (2014).
  158. Sterzyński, T., Tomaszewska, J., Piszczek, K. & Skórczewska, K. The influence of carbon nanotubes on the PVC glass transition temperature. *Compos. Sci. Technol.* **70**, 966–969 (2010).
  159. Yu, L. & Cebe, P. Crystal polymorphism in electrospun composite nanofibers of poly(vinylidene fluoride) with nanoclay. *Polymer (Guildf)*. **50**, 2133–2141 (2009).
  160. Cowie, J. M. G. & McEwen, I. J. Molecular Relaxations in Partially Hydrogenated cis-1,4-Polybutadienes. A Guide to the Glass Transition Temperature of Amorphous Polyethylene. *Macromolecules* **10**, 1124–1128 (1977).
  161. Ho, D. H. and C. C. Thermal conductivity of High Polymers. *J. Polym. Sci.* **3**, 659–670 (1965).
  162. Hansen, D. & Washo, B. D. Thermal Conductivity of High Polymers - The Influence of Molecular Weight. *Polym. Eng. Sci.* **6**, 260–262 (1966).
  163. Tung, L. J. & Buckser, S. The Effects of Molecular Weight on the Crystallinity of Polyethylene. *J. Phys. Chem.* **62**, 1530–1534 (1958).
  164. Ergoz, E., Fatou, J. & Mandelkern, L. Molecular weight dependence of the crystallization kinetics of linear polyethylene. I. Experimental results. *Macromolecules* **5**, 147–157 (1972).
  165. Perkins, W. G., Capiati, N. J. & Porter, R. S. The effect of molecular weight on the physical and mechanical properties of ultra-drawn high density polyethylene. *Polym. Eng. Sci.* **16**, 200–203 (1976).
  166. Maxfield, J. & Mandelkern, L. Crystallinity, Supermolecular Structure, and Thermodynamic Properties of Linear Polyethylene Fractions. *Macromolecules* **10**, 1141–1153 (1977).
  167. Strobl, G. R. & Hagedorn, W. Raman spectroscopic method for determining the crystallinity of polyethylene. *J. Polym. Sci. Polym. Phys. Ed.* **16**, 1181–1193 (1978).
  168. Enikolopian, N. S., Akopian, E. L., Styrikovitch, N. M., Ketchekian, A. S. & Nikolskii, V. C. Effect of molecular weight distribution and structure of LDPE on its deformation behavior in a high-temperature region. *J. Polym. Sci. Part B Polym. Phys.* **25**, 1203–1217 (1987).
  169. Samuel, A. Z. *et al.* Estimating Percent Crystallinity of Polyethylene as a Function of Temperature by Raman Spectroscopy Multivariate Curve Resolution by Alternating Least Squares. *Anal. Chem.* **89**, 3043–3050 (2017).
  170. Naylor, C. C. *et al.* Raman Spectroscopy Employed for the Determination of the Intermediate Phase in Polyethylene. *Macromolecules* **28**, 2969–2978 (1995).

171. Lagaron, J. ., Dixon, N. ., Reed, W., Pastor, J. . & Kip, B. . Morphological characterisation of the crystalline structure of cold-drawn HDPE used as a model material for the environmental stress cracking (ESC) phenomenon. *Polymer (Guildf)*. **40**, 2569–2586 (1999).
172. Zhang, T., Wu, X. & Luo, T. Polymer nanofibers with outstanding thermal conductivity and thermal stability: Fundamental linkage between molecular characteristics and macroscopic thermal properties. *J. Phys. Chem. C* **118**, 21148–21159 (2014).
173. Ma, Z. *et al.* Flexible and transparent optically anisotropic films based on oriented assembly of nanofibers. *J. Mater. Chem. C* **4**, 1029–1038 (2016).
174. Liu, J. & Yang, R. Length-dependent thermal conductivity of single extended polymer chains. *Phys. Rev. B - Condens. Matter Mater. Phys.* **86**, 104307 (2012).
175. Slack, G. A. The Thermal Conductivity of Nonmetallic Crystals. *Solid State Phys. - Adv. Res. Appl.* **34**, 1–71 (1979).
176. Lee, S. *et al.* Resonant bonding leads to low lattice thermal conductivity. *Nat. Commun.* **5**, 1–8 (2014).
177. Ong, W.-L. *et al.* Orientational order controls crystalline and amorphous thermal transport in superatomic crystals. *Nat. Mater.* **16**, 83–88 (2016).
178. Mattsson, B., Ericson, H., Torell, L. M. & Sundholm, F. Micro-Raman investigations of PVDF-based proton-conducting membranes. *J. Polym. Sci. Part A Polym. Chem.* **37**, 3317–3327 (1999).
179. Bellan, L. M., Kameoka, J. & Craighead, H. G. Measurement of the Young's moduli of individual polyethylene oxide and glass nanofibres. *Nanotechnology* **16**, 1095–1099 (2005).
180. Arinstein, A., Burman, M., Gendelman, O. & Zussman, E. Effect of supramolecular structure on polymer nanofibre elasticity. *Nat. Nanotechnol.* **2**, 59–62 (2007).
181. Ico, G. *et al.* Size-dependent piezoelectric and mechanical properties of electrospun P(VDF-TrFE) nanofibers for enhanced energy harvesting. *J. Mater. Chem. A* **4**, 2293–2304 (2016).
182. Cuenot, S., Demoustier-Champagne, S. & Nysten, B. *Elastic Modulus of Polypyrrole Nanotubes*. (2000).
183. Wingert, M. C., Jiang, Z., Chen, R. & Cai, S. Strong size-dependent stress relaxation in electrospun polymer nanofibers. *Cit. J. Appl. Phys.* **121**, 15103 (2017).
184. Mahieux, C. A. & Reifsnider, K. L. Property modeling across transition temperatures in polymers: A robust stiffness - Temperature model. *Polymer (Guildf)*. **42**, 3281–3291 (2001).
185. Czernin, J. & Phelps, M. E. Positron Emission Tomography Scanning: Current and Future Applications. *Annu. Rev. Med.* **53**, 89–112 (2002).
186. Rensch, C. *et al.* Microfluidics: A Groundbreaking Technology for PET Tracer Production? *Molecules* **18**, 7930–7956 (2013).
187. Wang, M. W., Lin, W. Y., Liu, K., Masterman-Smith, M. & Shen, C. K. F. Microfluidics for positron emission tomography probe development. *Mol. Imaging* **9**, 175–191 (2010).
188. Kimura, H. *et al.* Continuous-Flow Synthesis of N-Succinimidyl 4-[<sup>18</sup>F]fluorobenzoate Using a Single Microfluidic Chip. *PLoS One* **11**, e0159303 (2016).
189. Ismail, R. *et al.* Cationic imidazolium polymer monoliths for efficient solvent exchange, activation and fluorination on a continuous flow system. *RSC Adv.* **4**, 25348 (2014).
190. Salvador, B. *et al.* Disposable PDMS Chip With Integrated [<sup>18</sup>F]Fluoride Pre-Concentration Cartridge for Radiopharmaceuticals. *J. Microelectromechanical Syst.* **26**, 1442–1448 (2017).
191. Elizarov, A. M. *et al.* Design and optimization of coin-shaped microreactor chips for PET radiopharmaceutical synthesis. *J. Nucl. Med.* **51**, 282–7 (2010).
192. Pascali, G., Mazzone, G., Saccomanni, G., Manera, C. & Salvadori, P. A. Microfluidic approach for fast labeling optimization and dose-on-demand implementation. *Nucl. Med. Biol.* **37**, 547–555 (2010).
193. Elizarov, A. M. *et al.* Design and optimization of coin-shaped microreactor chips for PET radiopharmaceutical synthesis. *J. Nucl. Med.* **51**, 282–7 (2010).
194. Miller, P. W. Radiolabelling with short-lived PET (positron emission tomography) isotopes using microfluidic reactors. *J. Chem. Technol. Biotechnol.* **84**, 309–315 (2009).

195. Lu, S., Giamis, A. M. & Pike, V. W. Synthesis of [<sup>18</sup>F]fallypride in a micro-reactor: rapid optimization and multiple-production in small doses for micro-PET studies. *Curr. Radiopharm.* **2**, 81093 (2009).
196. Seok Moon, B. *et al.* Highly efficient production of [<sup>18</sup>F]fallypride using small amounts of base concentration. *Appl. Radiat. Isot.* **68**, 2279–2284 (2010).
197. Sasaki, H., Onoe, H., Osaki, T., Kawano, R. & Takeuchi, S. Parylene-coating in PDMS microfluidic channels prevents the absorption of fluorescent dyes. *Sensors Actuators, B Chem.* **150**, 478–482 (2010).
198. Abdelgawad, M., Watson, M. W. L. & Wheeler, A. R. Hybrid microfluidics: A digital-to-channel interface for in-line sample processing and chemical separations. *Lab Chip* **9**, 1046 (2009).
199. Rensch, C. *et al.* A solvent resistant lab-on-chip platform for radiochemistry applications. *Lab Chip* **14**, 2556–64 (2014).
200. Tantawy, M. N. *et al.* [<sup>18</sup>F]Fallypride dopamine D2 receptor studies using delayed microPET scans and a modified Logan plot. *Nucl. Med. Biol.* **36**, 931–940 (2009).
201. Fortt, R. & Gee, A. Microfluidics: a golden opportunity for positron emission tomography? *Future Med. Chem.* **5**, 241–244 (2013).
202. Philippe, C., Pichler, V., Hacker, M., Mitterhauser, M. & Wadsak, W. study. 5997–6004 (2018). doi:10.1039/c8dt00158h
203. Chen, S. *et al.* Radiolabelling diverse positron emission tomography (PET) tracers using a single digital microfluidic reactor chip. *Lab Chip* **14**, 902–910 (2014).
204. Arima, V. *et al.* Radiochemistry on chip: towards dose-on-demand synthesis of PET radiopharmaceuticals. *Lab Chip* **13**, 2328 (2013).
205. Pascali, G., Nannavecchia, G., Pitzianti, S. & Salvadori, P. A. Dose-on-demand of diverse 18 F-fluorocholine derivatives through a two-step microfluidic approach. *Nucl. Med. Biol.* **38**, 637–644 (2011).
206. Zeng, D. *et al.* Microfluidic radiolabeling of biomolecules with PET radiometals. *Nucl. Med. Biol.* **40**, 42–51 (2013).
207. von Eyben, F. E., Baumann, G. S. & Baum, R. P. PSMA diagnostics and treatments of prostate cancer become mature. *Clin. Transl. Imaging* **6**, 145–148 (2018).
208. Afshar-Oromieh, A. *et al.* Comparison of PET imaging with a<sup>68</sup>Ga-labelled PSMA ligand and<sup>18</sup>F-choline-based PET/CT for the diagnosis of recurrent prostate cancer. *Eur. J. Nucl. Med. Mol. Imaging* **41**, 11–20 (2014).
209. Afshar-Oromieh, A., Haberkorn, U., Eder, M., Eisenhut, M. & Zechmann, C. M. [<sup>68</sup>Ga]Gallium-labelled PSMA ligand as superior PET tracer for the diagnosis of prostate cancer: Comparison with<sup>18</sup>F-FECH. *Eur. J. Nucl. Med. Mol. Imaging* **39**, 1085–1086 (2012).
210. Ahmadzadehfar, H. *et al.* Therapeutic response and side effects of repeated radioligand therapy with <sup>177</sup>Lu-PSMA-DKFZ-617 of castrate-resistant metastatic prostate cancer. *Oncotarget* **7**, 12477–12488 (2016).
211. Zhang, X. *et al.* A simple microfluidic platform for rapid and efficient production of the radiotracer [<sup>18</sup>F]fallypride. *Lab Chip* **18**, 1369–1377 (2018).
212. Mueller, D. *et al.* Radiolabeling of DOTA-like conjugated peptides with generator-produced <sup>68</sup>Ga and using NaCl-based cationic elution method. *Nat. Protoc.* **11**, 1057–1066 (2016).
213. Mueller, D. *et al.* Simplified NaCl Based <sup>68</sup>Ga Concentration and Labeling Procedure for Rapid Synthesis of <sup>68</sup>Ga Radiopharmaceuticals in High Radiochemical Purity. (2012). doi:10.1021/bc300103t
214. Mueller, D. *et al.* Simplified NaCl based<sup>68</sup>Ga concentration and labeling procedure for rapid synthesis of<sup>68</sup>Ga radiopharmaceuticals in high radiochemical purity. *Bioconjug. Chem.* **23**, 1712–1717 (2012).